

AD-A170 673

DYNAMIC AND THERMODYNAMIC CHARACTERISTICS OF A  
MICROBURST-PRODUCING STORM. (U) AIR FORCE INST OF TECH  
WRIGHT-PATTERSON AFB OH R G HUGHES 1986

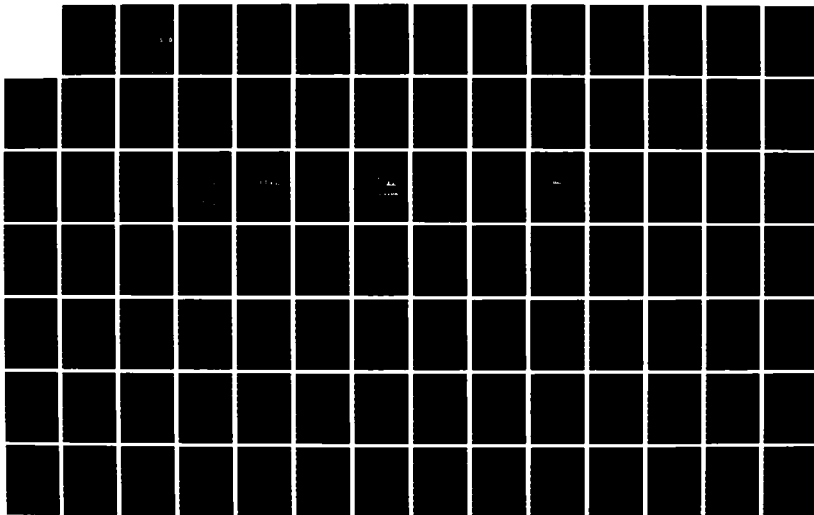
1/3

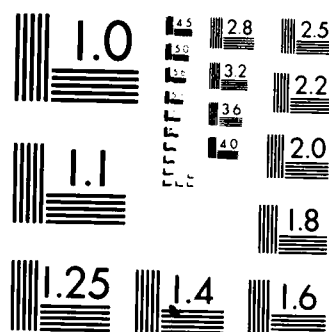
UNCLASSIFIED

AFIT/CI/NR-86-690

F/G 17/9

NL





MICROCOPY RESOLUTION TEST CHART  
NATIONAL BUREAU OF STANDARDS-1963-A

AD-A170 673

SECURITY CLASSIFICATION OF THIS PAGE (When Data Entered)

REPORT DOCUMENTATION PAGE		READ INSTRUCTIONS BEFORE COMPLETING FORM
1. REPORT NUMBER AFIT/CI/NR 86-69D	2. GOVT ACCESSION NO.	3. RECIPIENT'S CATALOG NUMBER
4. TITLE (and Subtitle) Dynamic and Thermodynamic Characteristics Of A Microburst-Producing Storm In Colorado Determined From Jaws Dual-Doppler Data		5. TYPE OF REPORT & PERIOD COVERED THESIS/DISSERTATION
		6. PERFORMING ORG. REPORT NUMBER
7. AUTHOR(s) Robert G. Hughes		8. CONTRACT OR GRANT NUMBER(s)
9. PERFORMING ORGANIZATION NAME AND ADDRESS AFIT STUDENT AT: Saint Louis University		10. PROGRAM ELEMENT, PROJECT, TASK AREA & WORK UNIT NUMBERS
11. CONTROLLING OFFICE NAME AND ADDRESS AFIT/NR WPAFB OH 45433-6583		12. REPORT DATE 1986
		13. NUMBER OF PAGES 214
14. MONITORING AGENCY NAME & ADDRESS (if different from Controlling Office)		15. SECURITY CLASS. (of this report) UNCLAS
		15a. DECLASSIFICATION/DOWNGRADING SCHEDULE
16. DISTRIBUTION STATEMENT (of this Report) APPROVED FOR PUBLIC RELEASE; DISTRIBUTION UNLIMITED		
17. DISTRIBUTION STATEMENT (of the abstract entered in Block 20, if different from Report)		
18. SUPPLEMENTARY NOTES APPROVED FOR PUBLIC RELEASE: IAW AFR 190-1		DTIC ELECTE AUG 12 1986 S D L. E. WOLAVER LYNN E. WOLAVER Dean for Research and Professional Development AFIT/NR
19. KEY WORDS (Continue on reverse side if necessary and identify by block number)		
20. ABSTRACT (Continue on reverse side if necessary and identify by block number)  ATTACHED.		

86

6

11

00

2

DD FORM 1 JAN 73 1473

EDITION OF 1 NOV 65 IS OBSOLETE

SECURITY CLASSIFICATION OF THIS PAGE (When Data Entered)

DTIC FILE COPY

## Digest

Some dynamic and thermodynamic structures of a microburst-producing storm which occurred on 14 July 1982 in Colorado were studied in detail. Dual-Doppler radar data collected during the Joint Airport Weather Studies (JAWS) project at Denver's Stapleton International Airport, were objectively analyzed to produce a 3D wind field. The analyzed domain had dimensions of 10 km by 10 km by 8.5 km centered on the microburst. Vertical velocities were computed by integrating the anelastic continuity equation downward from the storm's top. A variational approach was then employed to adjust the derived three-dimensional wind components. Subsequently, fields of deviation perturbation pressure, density and virtual temperature were recovered from a detailed wind field using the three momentum equations. These retrieved fields were subjected to internal consistency checks to determine the level of confidence before interpretation. ✕

Our study demonstrates that thermodynamic retrieval is feasible even when the storm intensity is non-severe. Variational adjustment substantially reduces errors in vertical velocity fields. Results show that the microburst being investigated occurs during the decaying stage of a storm. It is embedded

within the high reflectivity region with heavy precipitation. A strong downdraft impinges upon the surface producing a stagnation mesohigh inside the microburst. This high is accompanied by low pressure in the strongest outflow regions forming a pronounced horizontal perturbation pressure gradient outward from the center. Such pressure patterns are in good agreement with the surface observations in similar cases. The outflow region extends from the surface to approximately 1 km height AGL with maximum divergence in excess of  $10^{-2} \text{ s}^{-1}$ . In the middle troposphere, high pressure forms in the upshear side of the main updraft with low pressure on the downshear side due to dynamic interactions between the updraft and the sheared environmental wind. Favorable perturbation pressure gradients, evaporation and precipitation loading are responsible for initiating and sustaining a downdraft which produced the microburst at low levels.



Accession For	
NTIS CRA&I	<input checked="" type="checkbox"/>
DTIC TAB	<input type="checkbox"/>
Unannounced	<input type="checkbox"/>
Justification	
By	
Distribution /	
Availability Codes	
Dist	Avail and/or Special
A-1	

DYNAMIC AND THERMODYNAMIC  
CHARACTERISTICS OF A  
MICROBURST-PRODUCING STORM IN COLORADO  
DETERMINED FROM JAWS DUAL-DOPPLER DATA

Robert G. Hughes, B.A., M.S.

A Digest Presented to the Faculty of the Graduate  
School of Saint Louis University in Partial  
Fulfillment of the Requirements for the  
Degree of Doctor of Philosophy

1986

DYNAMIC AND THERMODYNAMIC  
CHARACTERISTICS OF A  
MICROBURST-PRODUCING STORM IN COLORADO  
DETERMINED FROM JAWS DUAL-DOPPLER DATA

Robert G. Hughes, B.A., M.S.

A Dissertation Presented to the Faculty of the Graduate  
School of Saint Louis University in Partial  
Fulfillment of the Requirements for the  
Degree of Doctor of Philosophy

1986

COMMITTEE IN CHARGE OF CANDIDACY:

Professor Yeong-jer Lin,  
Chairperson and Advisor

Professor Gandakota V. Rao

Associate Professor James T. Moore



#### DEDICATION

This endeavor is dedicated to my father,  
who was with me at the beginning and could  
not be with me at the end. I miss him.

## ACKNOWLEDGEMENTS

The author would like to thank Dr. Yeong-ger Lin for his guidance, assistance and patience throughout this endeavor. I would also like to extend my thanks to Drs. Gandakota V. Rao and James T. Moore for their comments, direction, and helpful criticisms. A very special thank you goes to Dr. Robert W. Pasken and Captain Frederick Wirsing who acted as patient sounding boards throughout.

Without a doubt, my deepest appreciation goes to Susan, my wife. In the final hours she gave up everything to aid in the completion of this work.

The authors work at St. Louis University is sponsored and supported by the United States Air Force Institute of Technology and the National Science Foundation under grant ATM 8312172, 8312172-01.

I also extend my appreciation to the personnel at the National Center for Atmospheric Research (NCAR) and the Joint Airport Weather Studies (JAWS) who made the data used in this study available.

## TABLE OF CONTENTS

Title	page
Dedication.....	iii
Acknowledgements.....	iv
List of Tables.....	vi
List of Figures.....	ix
1. Introduction.....	1
2. Statement of the Problem.....	22
3. Data Analysis and Reduction.....	25
4. Error Analysis.....	74
5. Sensitivity Tests of Thermodynamic Retrieval.	88
6. Discussion of Results.....	121
7. Summary and conclusions.....	159
Appendix A Objective Analysis Schemes.....	163
Appendix B Correction of the 3-D wind field.....	194
Appendix C Computation of Weighting Function....	203
Bibliography.....	206
Biography of the Author.....	213

## List of Tables

	Page
Table 3.1 Radar locations in latitude, longitude and CP-2 relative coordinates.	32
Table 3.2 NCAR Doppler radar characteristics for JAWS.	33
Table 3.3 Radar system parameters for data acquisition during JAWS.	34
Table 3.4 Terminal velocity in m s versus reflectivity in dBz	56
Table 3.5 Comparison of density computation methods.	59
Table 5.1 Description of the experiments conducted in the present study.	90
Table 5.2 Momentum Check values for each case at 1647 MDT. Cases considered include unsmoothed no friction (VUN), unsmoothed with Klemp and Wilhelmson friction parameterization (VUKW), unsmoothed with Austausch friction parameterization (VUA) with $K_m = 100 \text{ m s}^{-1}$ , smoothed no friction (VSN), smoothed with Klemp and Wilhelmson friction parameterization (VSKW), and smoothed with Austausch friction parameterization (VSA) with $K_m = 100 \text{ m s}^{-1}$ . The domain being considered is 10 km by 10 km centered on the microburst and containing the entire storm. Unsmoothed data were computed with a scan radius of 1.25 km, while smoothed data were computed with a scan radius of 1.75 km. VSKWE1 and VSKWE2 cases include 10 and 20% random errors, respectively, in the measured radial wind fields.	94

# List of Tables (continued)

	Page
Table 5.3a Values of the standard deviation (SD) for the two retrieved thermodynamic variables at a given level for 1647 MDT. Cases considered include unsmoothed no friction (VUN), Klemp and Wilhelmson frictional parameterization (VUKW), and Austausch frictional $\alpha$ parameterization (VUA) with $K_m = 100 \text{ m s}^{-1}$ . The domain being considered is 10 km by 10 km centered on the microburst and containing the entire storm. Units are in Pascals (Pa) and $^{\circ}\text{C}$ for pressure and temperature, respectively.	97
Table 5.3b As in Table 5.3a except for smoothed case.	98
Table 5.4a Values of the mean and standard deviation (SD) for horizontal Reynolds stresses; $\tau_{xx}$ , $\tau_{xy}$ and $\tau_{yy}$ and vertical Reynolds stresses; $\tau_{xz}$ , $\tau_{yz}$ , and $\tau_{zz}$ , computed from case VSKW with the Klemp and Wilhelmson frictional formulation at a given level for 1647 MDT.	99
Table 5.4b As in Table 5.4a but for case VSA with constant eddy viscosity coefficient ( $K_m = 100 \text{ m}^2 \text{ s}^{-1}$ ).	101
Table 5.5 Values of the mean and standard deviation (SD) for the three velocity components at a given level for 1647 MDT. Cases considered include VUN (variational-unsmoothed without friction) and VSN (variational-smoothed with friction). Scan radii employed are 1.25 and 1.75 km for unsmoothed and smoothed cases, respectively. The domain is 10 km by 10 km centered on the microburst.	111
Table 5.6 Values of root mean square error (RMSE) between basic case, VSKW, and various sensitivity test cases, VSKWE1, VSKWE2 and VSKWEL.	116

# List of Tables (continued)

	Page
Table A1. Relationship between $D_0$ and $D'$ for various values of $\Upsilon$ and $\lambda$ (km).	174
Table A2. The amplitude gain function $G$ , based on the theoretical formulas derived by Testud and Chong (1983). $G_1$ is the amplitude gain for $n = 1$ (first order) and $G_2$ is for $n = 2$ (second order). The cut-off wavelength (where $G = 0.5$ ), $\lambda$ , is 4.0 km.	189
Table A3. Computed values for $G_1$ and $G_2$ from the theoretical formulas derived by Testud and Chong (1983). Values of $\mu_1$ and $\mu_2$ are 0.1584 km and 0.0251 km, respectively. For comparison, values of $D'$ obtained from the Barnes (1973) scheme with $\Upsilon = 0.3$ and $R = 2.5$ are also listed.	192

## List of Figures

	Page
Fig. 1.1 Schematic illustration of an aircraft penetration of a microburst (not to scale), indicating first a rapidly increasing headwind (performance increasing), then the remnants of the downdraft (performance decreasing), followed by a strong tailwind (seriously decreasing performance). After McCarthy <u>et al.</u> (1983).	7
Fig. 1.2 Transient features of a descending microburst. Hatched areas represent pockets of high winds. Some midair microbursts descend to the surface becoming surface microbursts while others remain aloft. Midair microbursts cannot be detected by ground-based anemometers until they reach the surface (after Fujita, 1983).	9
Fig. 1.3 Daily count of NIMROD microbursts as determined by computer analysis. Then number of wet and dry microbursts is shown on the figure (after Fujita, 1983).	12
Fig. 1.4 As in Fig. 1.3 except for JAWS.	13
Fig. 1.5 Diurnal variation of surface microbursts. Top: 186 microbursts depicted during 86 days of JAWS operation. Bottom: 50 Microbursts during 43 days of NIMROD operation (after Fujita, 1983).	15
Fig. 1.6 Correlogram of maximum radar reflectivity at 500 m AGL versus maximum velocity differential (after McCarthy <u>et al.</u> , 1983).	16
Fig. 1.7 Scatter diagram of the relationship between rainfall rate and the maximum wind speed of 186 microbursts during JAWS (after Fujita, 1983).	17
Fig. 1.8 Frequency of surface microbursts presented as a function of the front-side to back-side wind shear (after Fujita, 1983).	18

# List of Figures (continued)

	Page
Fig. 1.9 Three stages of a descending microburst (after Fujita, 1985).	20
Fig. 1.10 Schematic views of wet and dry microbursts. Wet microbursts are expected to occur in the wet regions of the world, while dry microbursts are commonly seen in the dry regions with high bases of convective clouds.	21
Fig. 3.1 Relationship between detected wind speed and radar-storm-radar angle: (a) for $90^\circ$ and (b) for $40^\circ$ .	27
Fig. 3.2 Synoptic scale map for 14 July 1982, 0600 MDT.	29
Fig. 3.3 0000Z sounding for Denver, CO, 15 July 1982.	30
Fig. 3.4 Map illustrating JAWS Project facilities situated in the vicinity of Denver's Stapleton International Airport (after McCarthy <u>et al.</u> , 1983).	35
Fig. 3.5 As in Fig. 3.4 but including analysis grid. Grid is 20 km by 20 km.	40
Fig. 3.6 Final response curve from Barnes' gridding scheme for $R = 1.25$ km and $1.75$ km. $\Gamma = 0.3$ . Ordinate represents the wavelength and abscissa is the percentage of original amplitude retained after the gridding process.	48
Fig. 3.7 Plan and side view illustrating banding of the data which results from horizontal slicing of conical data.	49
Fig. 4.1 Error analysis for horizontal fields for two radars. Axes are in kilometers. Areas inside heavy line is within 120 km of at least two radars (after Ray <u>et al.</u> , 1978).	76



# List of Figures (continued)

	Page
Fig. 4.2 Graph of terminal velocity for both the FULL (...) and the ABBREVIATED (____) Foote and du Toit correction formula. Reflectivity is 60 dBz, density is from adiabatic-hydrostatic formulation. Terminal velocity formula is from Martner (1976). Difference at 200 mb is 1.08 m s.	83
Fig. 5.1 Horizontal Reynolds stresses $\tau_{xx}$ , $\tau_{xy}$ and $\tau_{yy}$ for case VSKW. Units are Newtons per square meter ( $N/m^2$ ).	104
Fig. 5.2 As in Fig. 5.1 except for case VSA.	105
Fig. 5.3 Range of $\tau_{xx}$ for given U-component differences for Klemp and Wilhelmson frictional parameterization and Austausch frictional parameterization.	106
Fig. 5.4 Vertical eddy viscosity coefficients computed from basic case (VSKW) horizontal winds using formula of Smagorinsky (1963). Units are $m^2s^{-1}$ .	108
Fig. 5.5 As in Fig. 5.4 except for horizontal eddy viscosity coefficients.	109
Fig. 5.6 Distribution of deviation perturbation pressure ( $P_d'$ ) at 0.25 km computed using winds with a randomly introduced 10% error in magnitude.	114
Fig. 5.7 As in Fig. 5.6 except for deviation perturbation virtual temperature ( $T_{vd}'$ ).	115
Fig. 5.8 Distribution of difference at 0.50 km between temperature computed with base case (VSKW) winds and temperature computed using winds with 10% induced error (VSKWE1).	119
Fig. 6.1 Distribution of U-component of wind superimposed on storm-relative horizontal winds at 0.25 km. Line AB signifies the line of vertical cross sections presented elsewhere. Isotachs are at intervals of $2 m s^{-1}$ .	122

# List of Figures (continued)

	Page
Fig. 6.2 As in Fig. 6.1 except for V-component. Dashed line denotes 0 isotachs for U-component of wind. M denotes the center of the microburst.	123
Fig. 6.3 As in Fig. 6.1 except for 1.0 km.	125
Fig. 6.4 As in Fig. 6.1 except for Reflectivity. Isopleths are at intervals of 10 dBz.	127
Fig. 6.5 As in Fig. 6.4 except for 4.0 km.	128
Fig. 6.6 Distribution of vertical velocity (w) superimposed on storm-relative horizontal winds at 0.50 km. Isotachs are at intervals of 4 m s <sup>-1</sup> .	130
Fig. 6.7 As in Fig. 6.6 except for 1.0 km.	132
Fig. 6.8 As in Fig. 6.6 except for 4.0 km.	133
Fig. 6.9 As in Fig. 6.6 except for 6.0 km.	135
Fig. 6.10 Vertical cross section along line AB showing vertical velocity superimposed on 3-dimensional wind field. Horizontal wind is the in-plane wind constructed from u and v components. Isotachs are at intervals of 4 m s <sup>-1</sup> .	137
Fig. 6.11 As in Fig. 6.10 except for reflectivity. Isopleths are at intervals of 10 dBz. (A) and dashed line denote microburst surface outflow boundary, (M) marks the center of the microburst and (B) is the reflectivity maximum along line AB.	139
Fig. 6.12 As in Fig. 6.1 except for Divergence with units of 10 <sup>-3</sup> s <sup>-1</sup> . Isopleths are at intervals of 4 * 10 <sup>-3</sup> s <sup>-1</sup> .	142
Fig. 6.13 As in Fig. 6.10 except for divergence in units of 10 <sup>-3</sup> s <sup>-1</sup> .	143

# List of Figures (continued)

	Page
Fig. 6.14 As in Fig. 6.1 except for deviation perturbation pressure. Isobars are at intervals of 5 Pascals (Pa).	145
Fig. 6.15 As in Fig. 6.14 except for 0.75 km.	147
Fig. 6.16 As in Fig. 6.14 except for 4.00 km. Isobars are at intervals of 10 Pascals (Pa).	148
Fig. 6.17 As in Fig. 6.10 except for deviation perturbation pressure. Isobars are at intervals of 10 Pascals (Pa). Dashed line denotes microburst outflow boundary.	151
Fig. 6.18 The distribution at 0.25 km of (a) deviation perturbation pressure in Pascals, (b) vertical velocity ( $w$ ) in $\text{m s}^{-1}$ , (c) divergence in $10^{-3} \text{s}^{-1}$ , (d) deviation perturbation temperature in $^{\circ}\text{C}$ and (e) in-plane horizontal velocity in $\text{m s}^{-1}$ along line AB.	152
Fig. 6.19 As in Fig. 6.1 except for deviation perturbation virtual temperature. Iso-pleths are at intervals of $1^{\circ}\text{C}$ .	156
Fig. 6.20 As in Fig. 6.10 except for deviation perturbation virtual temperature.	157
Fig. A1 Relationship between the data point and the grid points for Barnes scheme.	165
Fig. A2 Relationship of response function to wavelength for various choices of parameter $K$ (after Barnes, 1973).	167
Fig. A3 Cressman weighting function (solid line) compared to first pass of Barnes weighting function (dashed line). For Cressman, $R = 1.7$ , for Barnes $R = 2.3$ . Crossover point is $r=1.15$ with weight $w = \exp(-1) = 0.368$ .	168

# List of Figures (continued)

	Page
Fig. A4 Response curve for Barnes scheme (Eq. A5) for various values of $R$ . Ordinate represents the percentage of original amplitude returned after gridding procedure.	170
Fig. A5 Response $D'$ after one correction pass as a function of initial response $D_0$ and arbitrary parameter $r$ . After Barnes, 1973.	173
Fig. A6 Response functions $D_0$ and $D'$ versus the wavelength $\lambda$ in km.	182
Fig. A7 Amplitude gain $G$ of the filtering as a function of the wavelength $\lambda$ . Curve A variational analysis with functional $J$ ; curve B variational analysis with functional $J$ ; Curve C filtering using the Cressman weighting function. The response curve $D'$ obtained from Barnes (1973) scheme with $\gamma=0.3$ and $R=3.6$ km is denoted by the symbol $x$ .	187
Fig. A8 Comparison of response curves obtained from Barnes (1973) scheme ( $D'$ ) with $\gamma=0.3$ and $R=2.5$ km and theoretical formulas derived by Testud and Chong (1983) for $n=1$ ( $G_1$ ) and $n=2$ ( $G_2$ ).	190
Fig. B1 Relationship between "true" functional solution and neighboring function for method of calculus of variation.	197

## CHAPTER 1

### Introduction

In early studies of the Thunderstorm Project, Byers and Braham (1948) pointed out the co-existence of strong updrafts and downdrafts in thunderstorms during the mature stage with vertical velocities reaching 40 m s . They suggested three mechanisms important in the development, enhancement and maintenance of the strong downdraft; 1) entrainment of outside air into the rear of the storm, 2) evaporation of precipitation into this drier entrained air, and 3) aerodynamic drag effects of precipitation. For a severe thunderstorm, Newton (1963) added to these mechanisms the effect of forced lifting created by this downrush of colder air spreading out under the storm. This forced lifting provides a continuing energy source in the form of warmer moist inflow. Both Byers and Braham (1948) and Newton (1963) along with many other investigators recognized the need to understand this downdraft and its role in the thunderstorm life cycle. Byers and Braham (1948) stated in their conclusions that the distribution of temperature and hydrometeors within the thunderstorm remained to be studied. Newton (1963) in his summary stated that

the Thunderstorm Project of Byers and Braham had provided many new hypotheses which needed to be verified.

Studies of the internal structure of the thunderstorm using the radar as a remote sensing device has been in progress since the operators of the Illinois State Water Survey radar spotted the first hook echo in 1947. Browning and Ludlam (1962) documented the internal structure and kinematic features of the Wokingham supercell hail storm. However, they were unable to detail dynamic and thermodynamic information due to the restrictions of the radar. Others attempted alternative techniques to gain insight into the internal structure of storms. Atlas and Wexler (1965) suggested a modification to the beam pattern of a conventional radar which would allow horizontal wind fields to be extracted. Davis-Jones and Henderson (1973) launched in-storm rawinsondes and Sinclair (1978) attempted aircraft penetration. All these attempts proved to be too expensive, unsafe, or unreliable in the continuing investigation of the thunderstorm.

The advancement of Doppler radar techniques in deducing air motion within convection storms has added the needed tool necessary to increasing our understanding of the kinematic and dynamic structure of the storm. Multiple Doppler radars can provide three

dimensional winds inside the storm; for example, see studies by Pille', Justio and Rogers (1963) and Armijo (1969). Lhermitte (1970) was the first to use the Doppler radar to observe horizontal wind fields within a convective storm. Ray et al. (1975) were the first to study a severe storm. Their results of low level wind features essentially verified features described by Ludlam (1963) and Newton (1963). Since the pioneering work of Ray et al. (1975), many other researchers have used the multiple Doppler radar as the primary tool in the investigation of kinematic features of severe thunderstorms, e.g., Kropfli and Miller (1976), Brandes (1977a, 1977b, 1978), etc.

Dual-Doppler radar measurements cannot, however, provide a direct measure of thermodynamic and pressure information. Fluctuations in pressure and temperature (potential temperature) are important in understanding the structure and internal dynamics of a convective storm. These fluctuations are only a few degrees in temperature and a few millibars in pressure and cannot accurately be measured by conventional upper air sounding techniques. Some type of indirect measurement method is necessary to recover these thermodynamic fluctuations from measurable fields, such as a detailed wind field.

Recently Gal-Chen (1978) proposed a retrieval technique in which the momentum equations and the observed three-dimensional wind field are employed to determine the density, pressure and temperature fluctuations. This method has been employed on model generated data and observed wind fields by Gal-Chen (1978), Hane et al. (1981), Lin and Pasken (1982a,b), Pasken and Lin (1982), Brandes (1984), Hane and Ray (1985), and Lin et al. (1985).

Since the method proposed by Gal-Chen (1978) is indirect, its effectiveness to a large extent depends on the degree of accuracy in the input data (Hane et al., 1981). Thus, verification of the recovered fields of pressure, density and temperature fluctuations is critical. While direct verification is desirable, they are difficult to obtain especially within the storm. Consequently, some indirect verification is needed in order to validate the method and the recovered fields. Gal-Chen and Hane (1981) suggested three indirect verification techniques: 1) numerical simulations, 2) momentum checking, and 3) time continuity. Hane et al. (1981) applied this retrieval technique to numerical simulations as a guide to verification. Momentum checking was employed in studies by Gal-Chen and Kropfli (1984), Hane and Ray (1985) and Lin et al. (1985). Time continuity



checking was reported in a study by Gal-Chen and Kropfli (1984).

The aforementioned studies showed that the retrieval method is feasible for recovering perturbation pressure, virtual temperature or, virtual potential temperature within a convective storm. The degree of accuracy of the observed winds appears to be the key factor in determining the effectiveness and validity of the method. As Gal-Chen and Hane (1981) concluded "Studies using real data are encouraging. It appears that pressure fluctuations within 30% accuracy can be retrieved. Retrieval temperature and pressure fields demonstrate the importance of non-hydrostatic pressure gradients in convective dynamics and appear to display continuity and coherence. Firm verification of these results, as well as further technique developments (particularly in retrieval of vertical velocities), should be pursued with vigor. Almost everything in this vast and difficult problem still remains to be done."

The Joint Airport Weather Studies (JAWS) project was jointly conducted by scientists from the National Center for Atmospheric Research (NCAR) and the University of Chicago in the summer of 1982 at Denver's Stapleton International Airport. Primary objectives of the project include: 1) the research on

fine-scale structure of thunderstorm dynamics and kinematics in the vicinity of the airport, 2) the effect of thunderstorm low-level wind shear on aircraft performance, and 3) the development of real-time testing of low-level wind shear interaction and warning techniques and displays, see McCarthy et al. (1982).

Fujita (1978) defined the term "microburst" as a small downburst, less than 4 km in outflow diameter, with peak winds lasting only 2 to 5 minutes. A microburst could occur in areas of precipitation or no precipitation. It induces a sudden outflow of damaging horizontal winds near the ground. Fujita and Wakimoto (1983) further noted that this outburst may be sensed at the surface within a few minutes or may dissipate aloft without being sensed at the surface. Either of the types can produce dangerous tailwind and downflow wind shear which can reduce aircraft performance below critical operating levels, especially during takeoff and landing (see Fig. 1.1). The low-level wind shear associated with microburst has been cited as a main cause of many aircraft accidents in the U.S.; for example, see studies by Fujita and Byers (1977), Fujita and Caracena (1977), NTBS (1983), and more recently Fujita (1985).

The above definition of microbursts was somewhat

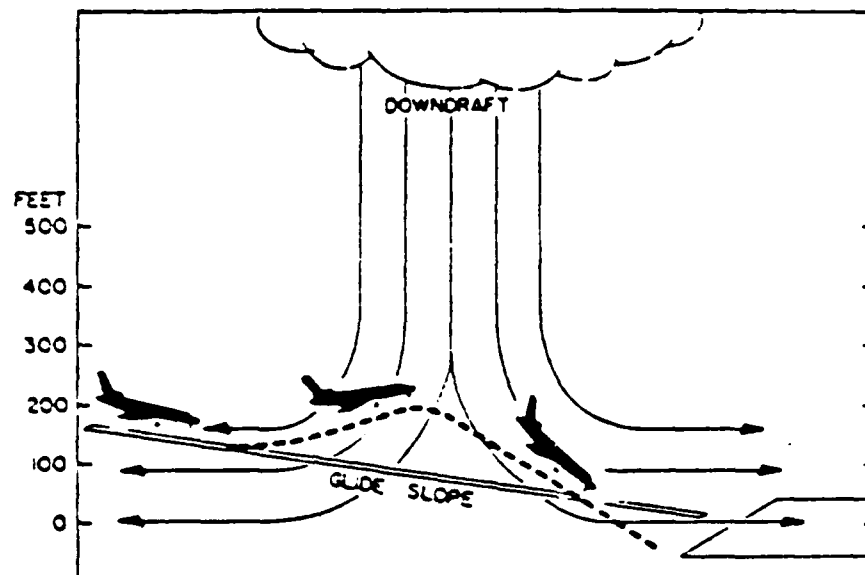


Figure 1.1 . Schematic illustration of an aircraft penetration of a microburst (not to scale), indicating first a rapidly increasing headwind (performance increasing), then the remnants of the downdraft (performance decreasing), followed by a strong tailwind (seriously performance decreasing), (AFTER MCCARTHY, ET AL., 1983.)

restricted in the JAWS study to be more aligned with the aviation involvement (McCarthy et al., 1983). They defined a microburst as a downdraft-induced, damaging horizontal flow near the surface, whose horizontal dimension is  $< 4$  km, and whose differential velocity is  $> 10 \text{ m s}^{-1}$ . If the initial horizontal dimension is  $> 4$  km, the feature is referred to as a macroburst (Fujita and Wakimoto, 1983).

In an effort to distinguish microburst types, two subcategories were created. According to Fujita and Wakimoto (1983), a "wet" microburst is a microburst event also accompanied by at least 0.01" of precipitation reaching the surface between the onset and end of the high winds, including any calm periods, while a "dry" microburst is an event with less than 0.01" of precipitation. They further defined the term "surface microburst" as a microburst with its outburst winds detectable by a network of ground-based anemometers (Fig. 1.2).

Mueller and Hildebrand (1983) detailed the structure of a microburst and compared the vertical velocities deduced from dual-Doppler radar data with airborne Doppler radar data scanning in the vertical. They found that a good agreement between the location of updraft and downdraft features and the vertical velocities were within a few  $\text{m s}^{-1}$ . Kessinger et al.

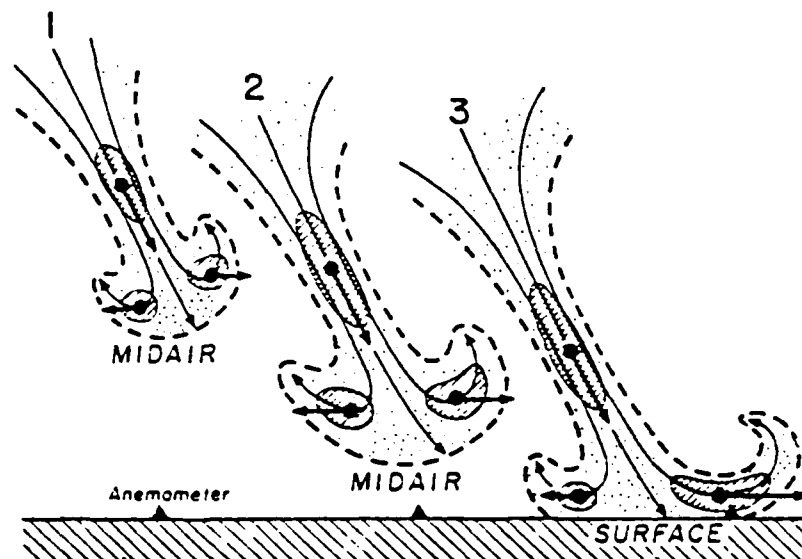


Fig. 1.2 Transient features of a descending microburst. Hatched areas represent pockets of high winds. Some midair microbursts descend to the surface becoming surface microbursts while others remain aloft. Midair microbursts cannot be detected by ground-based anemometers until they reach the surface. (AFTER FUJITA, 1982.)

(1983) compared the low-level horizontal flow computed from dual-Doppler radar data and Portable Automated Mesonet (PAM) surface data. Results indicated that the derived horizontal velocities were faster than those observed within the PAM network. They attributed this result to the presence of frictional forces in the surface boundary-layer which were at the level of the PAM sensors but below the lowest level the radars were able to detect. Wilson et al. (1984) identified 70 microbursts using Doppler radar results during the 86 day observation period. Using PAM data, Fujita and Wakimoto (1983) identified up to 186 microbursts during the same period. At this point it is constructive to consider what is known, in general, about microbursts, realizing that the observed samples from which this climatology is drawn is not only limited in size but in geographical extent as well.

### 1.1 Microburst Climatology

During the last decade, two extensive field studies have been conducted observing and studying microbursts. The Northern Illinois Meteorological Research On Downbursts (NIMROD) was conducted in the Chicago area from 19 May through 1 July 1978, lasting 43 days. The Joint Airport Weather Studies Project (JAWS) was conducted in the Denver area from 15 May through 9 August 1982, totaling 86 days. It is impor-

tant to remember when comparing results of these studies that they occurred in areas with different environmental conditions. The NIMROD study included the effects of a much smoother terrain and the effects of a large lake (Lake Michigan) to the east, while the JAWS environment was more that of the High Plains with little locally available moisture and a large mountain range immediately to the west.

Figures 1.3 and 1.4 show the number of microbursts in chronological fashion that Fujita and Wakimoto (1983) found looking at the PAM data from both studies. Notice that they are somewhat dissimilar. The NIMROD data appear to contain many more wet occurrences (32/50) than dry ones (18/50). On the other hand, the JAWS data reveal the opposite. Among the 186 microbursts identified by PAM data, 155 were dry and only 31 were wet. Moisture availability and the higher cloud bases generally noted in the High Plains thunderstorm allowing precipitation to evaporate prior to reaching the surface could account for this difference. Also note the apparent cyclic occurrence in the NIMROD data. Fujita and Wakimoto (1983) suggested that this may be due to synoptic scale forcing mechanisms in the case of NIMROD and more local effect mechanisms, such as orographic lifting and solar heating, in the case of JAWS.

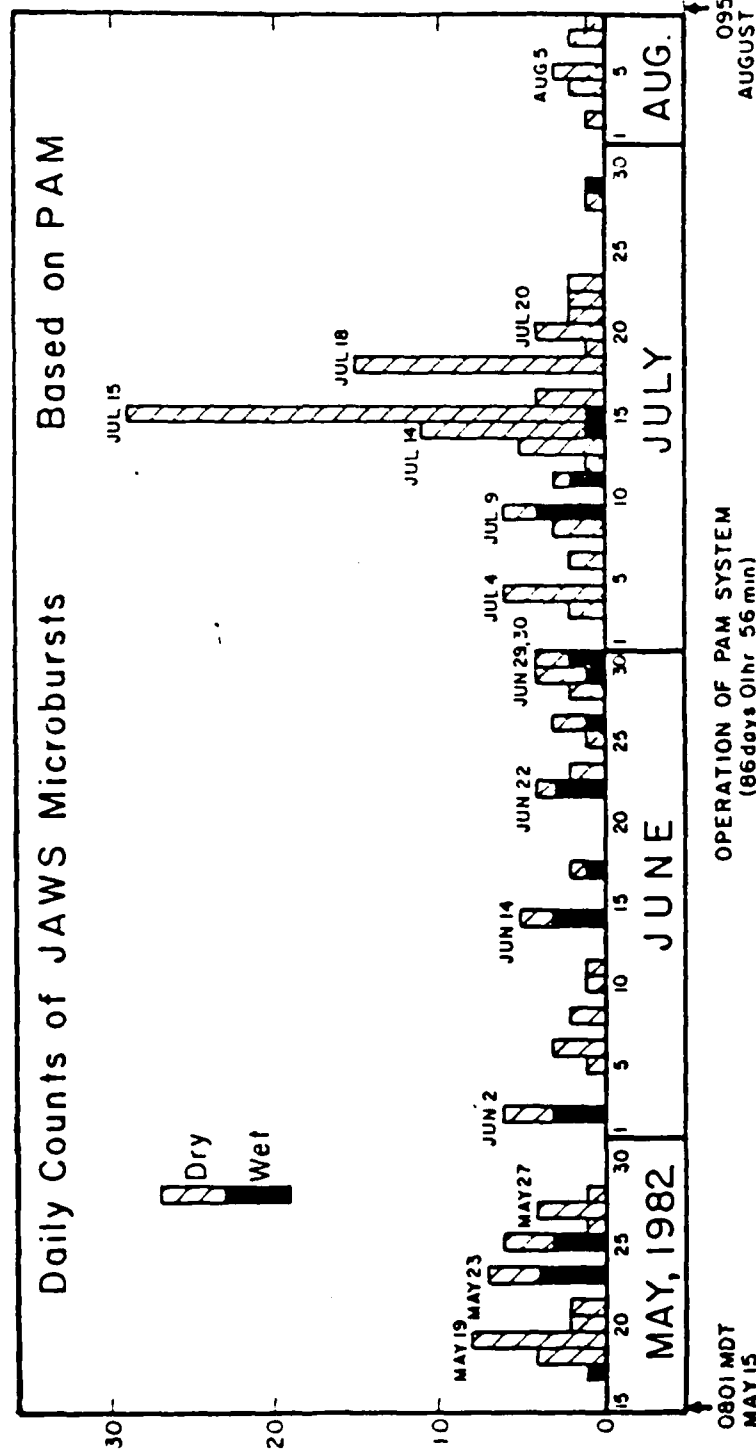


Fig. 1.3 Daily count of JAWS microbursts as determined by computer analysis. The number of wet and dry microbursts is shown on the figure. (AFTER FU-CA 1983.)



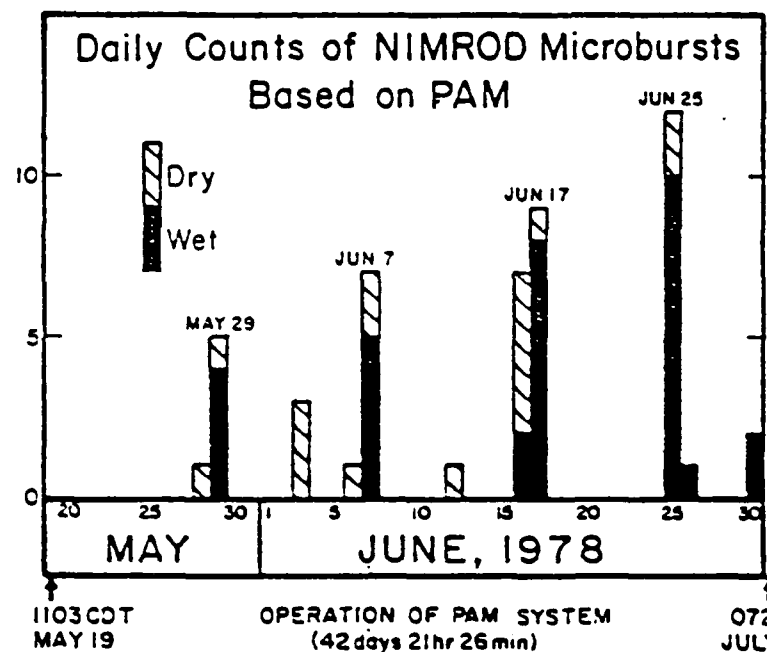


Fig. 1.4 Daily count of NIMROD microbursts as determined by computer analysis. The number of wet and dry microbursts is shown on the figure. (AFTER FUJITA 1983.)

Figure 1.5 shows the occurrence of microbursts by hour for the two studies. The diurnal signal seems to be present in the JAWS data but not the NIMROD data. Also, note that the diurnal signal in the JAWS data is present in both the wet and dry cases. The larger number of microbursts which occurred after daylight in the Midwest can be attributed to the larger number of nocturnal thunderstorms. Perhaps the most revealing results are shown in Figs. 1.6 and 1.7. Figure 1.6 depicts the relationship between maximum reflectivity in the parent storm at 500 m AGL and the maximum differential horizontal wind speed across the microburst. The fact that the correlation is almost nonexistent suggests to a forecaster that perhaps he should look elsewhere for a telltale signal of an impending microburst, especially when making a wind shear intensity forecast or "nowcast". The relationship between the rainfall rate and the maximum wind speed is shown in Fig. 1.7. Again the correlation is very small suggesting little or no relationship between the horizontal wind speed and the amount of rainfall reaching the ground. Figure 1.8 depicts front-rear windshear for the 186 microbursts identified by Fujita and Wakimoto (1983). While one may be tempted to suggest that the presence of precipitation enhances the horizontal wind shear, the reader is

## DIURNAL VARIATION OF MICROBURSTS

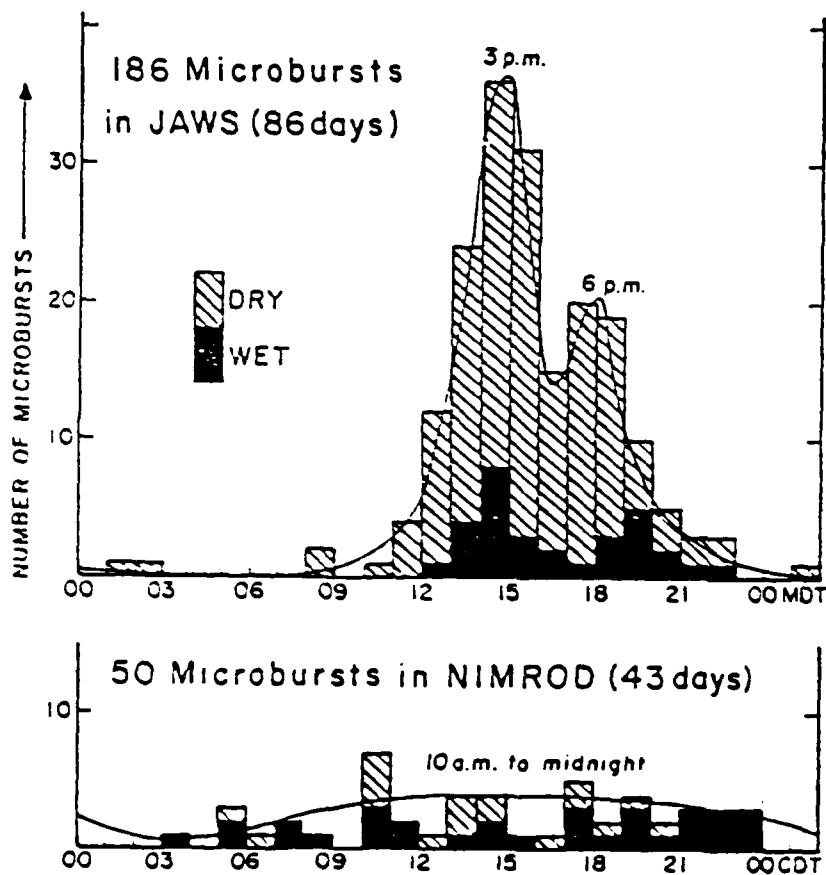


Fig. 1.5 Diurnal variation of surface microbursts. Top: 186 microbursts depicted during 86 days of JAWS operation. Two peak activity periods are 1500 and 1800 MDT. Bottom: 50 microbursts during 43 days of NIMROD operation. Rather uniform activity is seen from 1000 MDT to midnight. (AFTER FUJITA, 1963.)

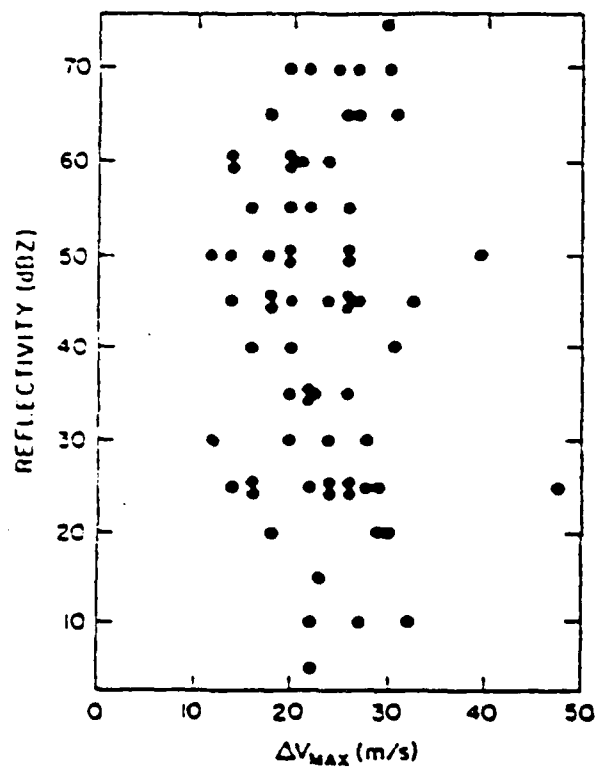


Fig. 1.6 Correlogram of maximum radar reflectivity at 500 m AGL versus maximum velocity differential (after McCarthy et al., 1983).

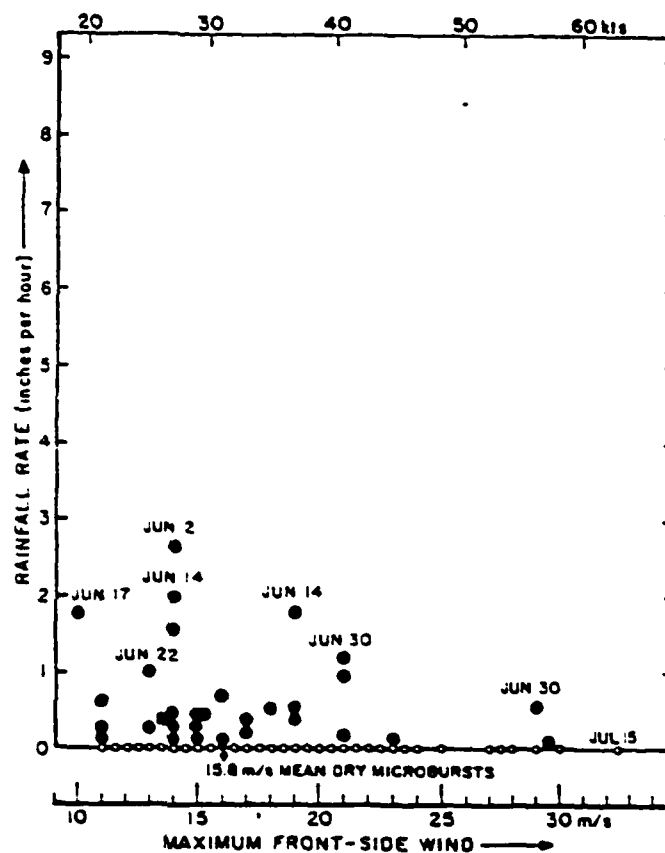


Fig. 1.7 Scatter diagram of the relationship between rainfall rate and the maximum wind speed of 186 microbursts during JAWS (AFTER FURITA 1983.)

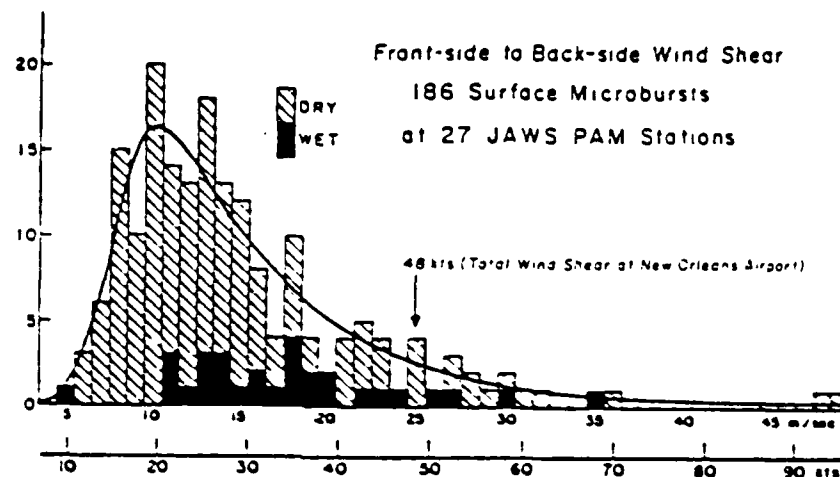


Fig. 1.8 Frequency of surface microbursts presented as a function of the front-side to back-side wind shear. An aircraft penetrating through a microburst from the front or the backside would experience this magnitude of wind shear. (After RITA, 1981)

reminded of the small size and local nature of this sample.

Figure 1.9 shows expected changes one is likely to encounter when looking at macrobursts and microbursts. For a microbursts the downflow may extend very close to the ground prior to spreading out. In cases where the precipitation shaft does not reach the surface, the downward moving air is heated dry-adiabatically unless evaporative cooling can occur (Fig. 1.10). When precipitation is occurring from the cloud base to the surface, cooling is less likely since the air is already highly saturated. Srivastava (1985) notes that the downward moving air is heated nearly dry adiabatically. This suggests that while the air is descending through the relatively saturated area within the precipitation shaft below the cloud base, it does not evaporate enough of the rain to either cool the air or cause it to heat up at the moist adiabatic rate. possible to obtain a temperature deviation which is warmer than normal (Fujita, 1985).

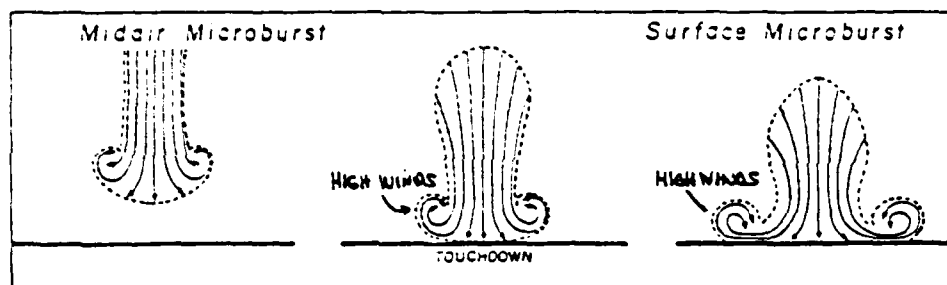


Fig. 1.9 Three stages of a descending microburst. A mid-air microburst may or may not descend to the surface. If it does, the outburst winds develop immediately after its touchdown. (AFTER FUJITA, 1985)



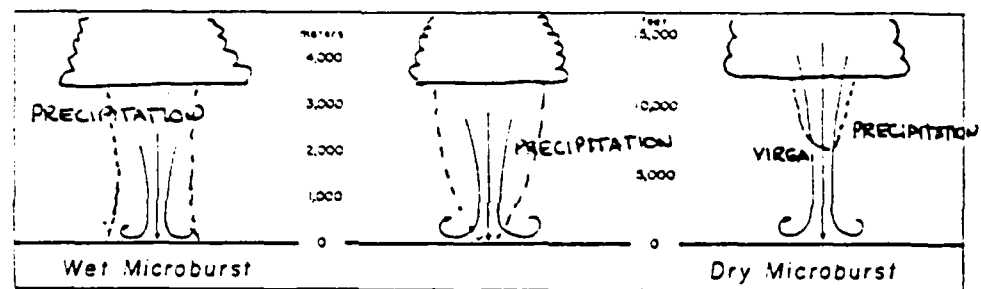


Fig. 1.10 Schematic views of wet and dry microbursts. Wet microbursts are expected to occur in the wet regions of the world, while dry microbursts are commonly seen in the dry regions with high bases of convective clouds. (AFTER FUJITA, 1985)

## CHAPTER 2

### Statement of the Problem

The main objective of this dissertation research is to study the kinematic, dynamic and thermodynamic (via retrieval techniques) structures of a microburst-producing thunderstorm. The storm which produced this microburst was of "average" strength. One of the primary reasons a storm of this strength was chosen was to test the subtleness of the techniques in recovering the derived fields. Data used in the research are dual-Doppler radar measurements taken during the JAWS project. The specific storm being investigated occurred on 14 July 1982 with the microburst beginning near 1641 MDT and continuing through 1651 MDT. During this period, a peak velocity difference across the microburst of  $21 \text{ m s}^{-1}$  was observed, see McCarthy et al. (1983). The data being considered in this study are for a full volume scan beginning at 1646 MDT and ending at 1648 MDT.

The analysis and reduction of the data are similar to those developed by Lin and Pasken (1982) and Wirsing (1985). Data retrieved will include horizontal

wind fields as suggested by Armijo (1969) and vertical wind fields using the anelastic continuity equation with the lower boundary condition applied similar to Rodi et al. (1983). Perturbation pressure and temperature deviations, from their horizontal averages, will be retrieved using the method outlined by Gal-Chen (1973). These data will be judiciously processed and carefully checked using the objective analysis schemes developed at NCAR and here at St. Louis University. Once the thermodynamic fields are retrieved, momentum and time continuity checks proposed by Gal-Chen and Hane (1981) will be employed to determine the "goodness" of the derived fields.

Once this has been accomplished, the data will be used to test the hypothesis that a downdraft which produced the microburst at low levels was triggered and to some extent maintained by a favorable perturbation pressure gradient force (PPGF) together with the combined effects of evaporative cooling and precipitation loading in the middle troposphere. For a wet microburst, precipitation loading is more important than evaporative cooling. As a downdraft approaches the lower troposphere, a strong downflow with speeds reaching  $-10 \text{ m s}^{-1}$  impinges upon the surface forming a "stagnation mesohigh". This high is surrounded by low pressure in the regions with the strongest outflow

resulting in a pronounced horizontal PPGF outward from the high pressure center. This PPGF is primarily responsible for driving intense diverging outflow in the lower layers, extending from the surface to approximately 1 km height.

In order to determine the role played by friction in thermodynamic retrieval, a frictional parameterization scheme similar to that of Klemp and Wilhelmson (1978) will be employed. The variability of eddy viscosity coefficients and Reynolds stresses (eddy transfer of momentum) in the subcloud layer of a storm will be studied in detail. Such a study will reveal the effect of low-level transfer of momentum by eddies on the structure and internal dynamics of a nonsevere thunderstorm which produced a microburst in Colorado.

## CHAPTER 3

### Data Analysis and Reduction

The success of thermodynamic retrieval, to a considerable extent, depends on the degree of accuracy of the detailed wind field (Hane et al., 1981; Lin and Pasken, 1982). The data set used in this study was obtained from the JAWS project. It represents an individual deep volume scan of a storm by two separate radars beginning at 1646 MDT. The storm was producing a microburst at that time which actually lasted from 1643 to 1651 MDT.

The parent storm which produced the microburst is closer to an "average" strength storm. A storm of this strength is more likely to be encountered than storms which also produce severe weather. One of the primary reasons this storm was chosen for study was to test the subtleness of the techniques in recovering the derived fields from a less intense storm. In addition, a deep volume scan is available for this storm from the surface to approximately 8 km AGL. Hence the entire storm structure can be investigated using a variational approach with downward integration.

While no dynamic studies of this specific storm

have been performed, Wilson et al. (1984) studied the kinematic aspects of this particular microburst at the 50 m level from 1641 to 1650 MDT. In addition, Mueller and Hildebrand (1983) analyzed a microburst case from the JAWS data for 29 June 1982. Results from these studies will be compared with the results from the present study in Chapter 6.

The data from NCAR's CP2 and CP4 Doppler radar were chosen for use in this study. There are two reasons for choosing these radars. First, the cross-beam angle formed by the two radars is larger ( $78^{\circ}$ ) for CP2 and CP4 than either CP2 and CP3 ( $43^{\circ}$ ) or CP3 and CP4 ( $35^{\circ}$ ). Second, the storm and the radars nearly form an isosceles triangle with the storm at the vertex of the sides of equal length. These tend to minimize the effect of errors and variance of the measured wind field on the derived wind field (Fig. 3.1).

Studies which focus on the kinematic aspects of storms generally require only first derivatives of derived velocity. This study utilizes the complete momentum equations and their differential form and, therefore, requires higher order derivatives. Thus, the criteria used in the processing of the measured data must be more stringent than those employed in a kinematic study.

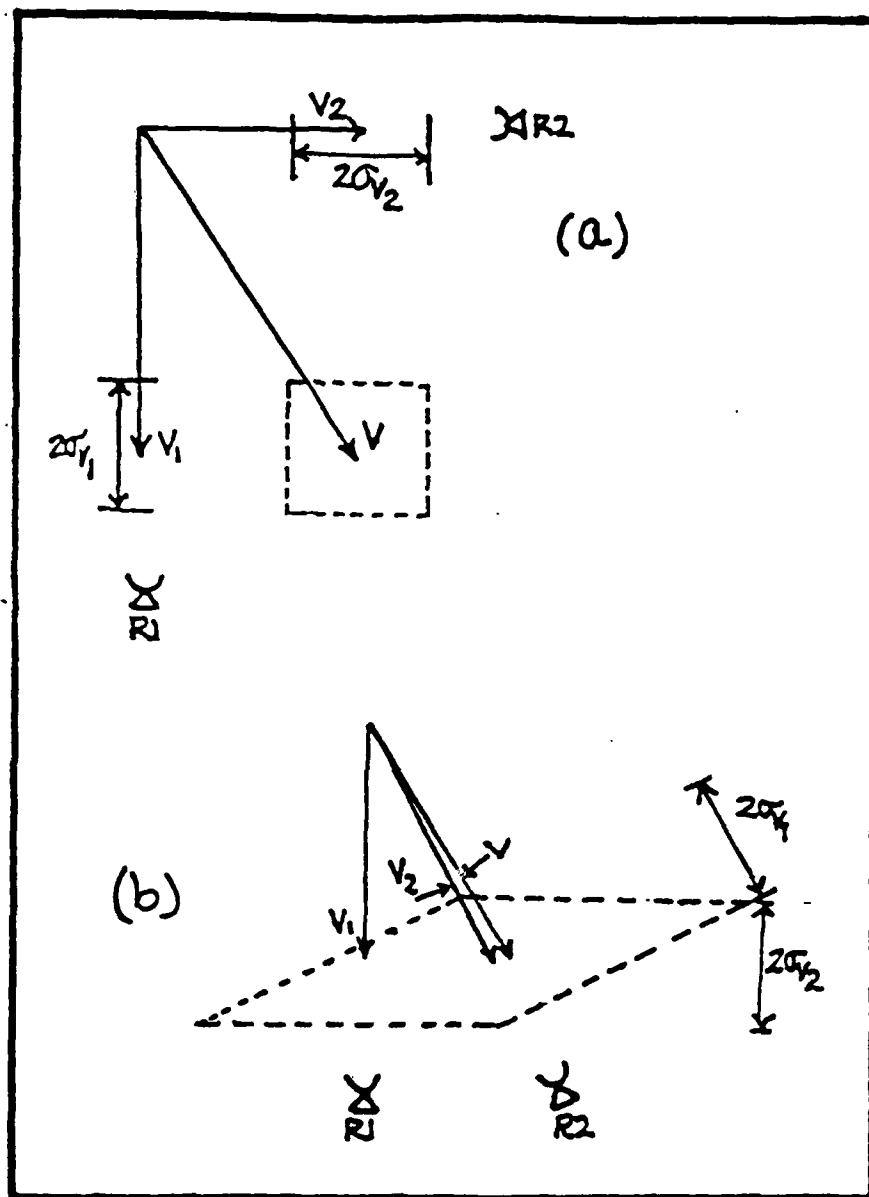


Fig. 3.1 Relationship between detected wind speed and radar-storm-radar angle: (a) for  $90^\circ$  and (b) for  $40^\circ$ .

Section 3.1 describes the general synoptic situation. In Section 3.2, the characteristics of the radars and specific information on the data set are detailed. Section 3.3 discusses the data reduction techniques in detail. Each critical choice is reviewed and reasons for specific choices offered. The computational procedure to synthesize a 3-D wind field from radial velocities and radar reflectivities are presented in Section 3.4. Section 3.5 discusses the variational adjustment of the 3-D wind field to conform to the lower kinematic boundary condition at the surface. Finally, Section 3.6 discusses the recovery of thermodynamic variables, e.g., perturbation pressure deviation, perturbation density deviation and perturbation virtual temperature deviation, in detail.

### 3.1 Synoptic Situation

The synoptic situation at 0600 MDT on 14 July 1982 is shown in Fig. 3.2. It revealed a high pressure center in northwestern Colorado with a cold front farther west. This cold front passed through the Denver area after the 1800 MDT 14 July time.

The sounding for Denver released at 0000 GMT on 15 July (equivalent to 1800 MDT 14 July) is presented in Fig. 3.3. It shows a dry layer from the surface to the reported cloud base at 3.5 km AGL (Rodi et al.,



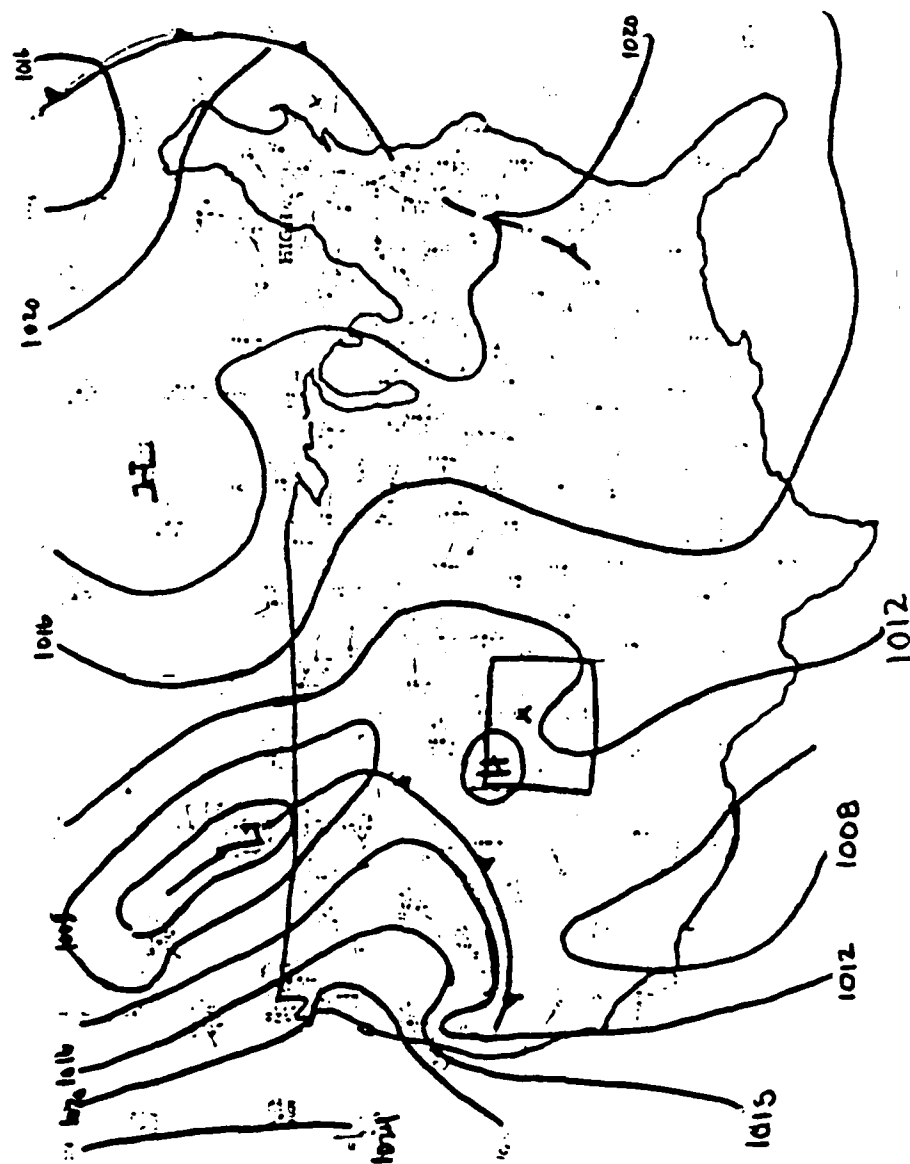


Fig. 3.2 Synoptic scale map for 14 July 1982, 0600 HDT.

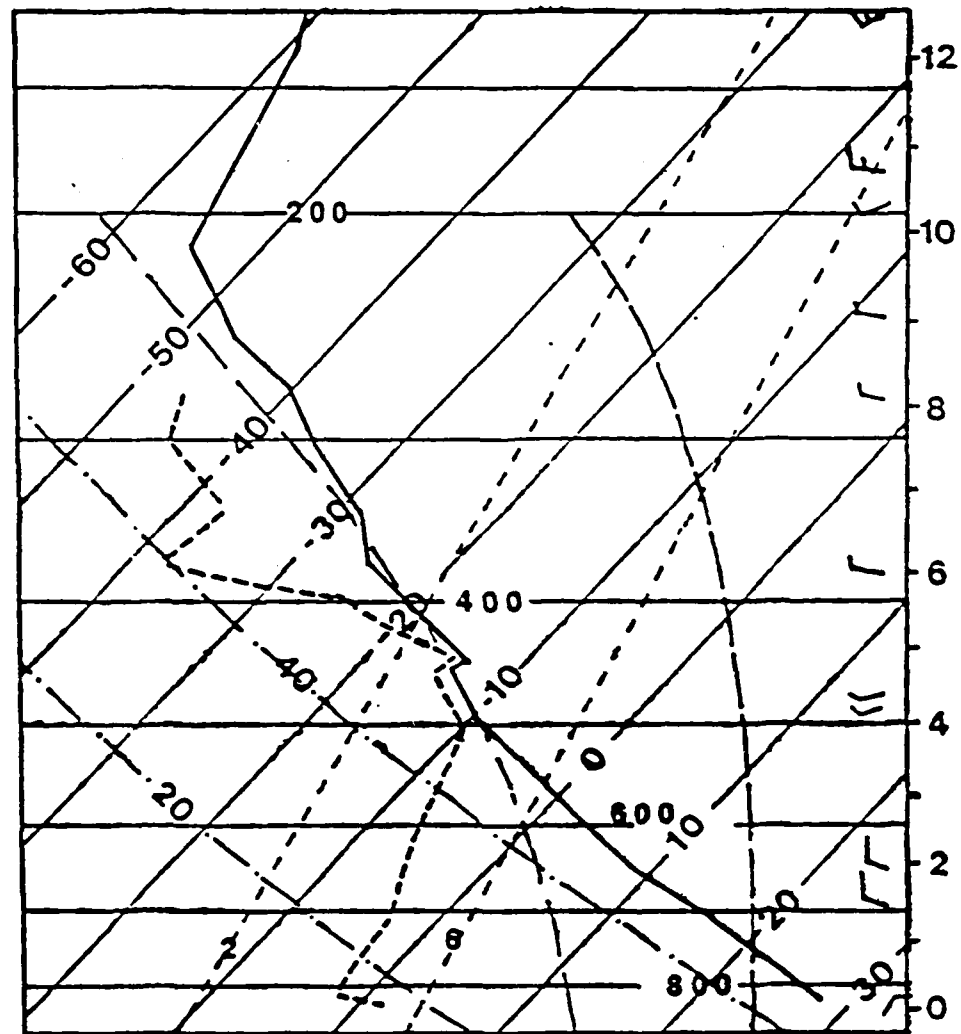


Fig. 3.3 0000Z sounding for Denver, CO, 15 July 1982.

are shown in Tables 3.1, 3.2, and 3.3. Different scanning strategies were employed due to joint use of CP2. This radar was required to make a 360 degree sweep at low elevation angles every 5 minutes. This took approximately 1 minute to complete and utilized the capability of the radar to change pulse repetition frequency (PRF). In addition, when not needed by the JAWS personnel, this radar made a complete 360 degree volume scan every 15 minutes. The other two radars, CP3 and CP4, were used for JAWS objectives.

To reduce temporal and spatial problems within the data set, an effort was made to scan the same volume at the same time with more than one radar. The scanning sequence, including the elevation angles selections for each radar, was coordinated between radars. This resulted in a data set which has a higher degree of temporal coincidence than has been previously produced.

Theoretically and ideally, the volume scanned by the two radars should be the same. To achieve this with two Doppler radars can be somewhat of a problem. It involves a particular geometric interrelationship between the two radars and the storm. The storm should be located so as to form an isosceles triangle with the storm at the vertex of the equal legs. Figure 3.4 shows the relationship between the radars

Table 3.1

Radar locations in latitude, longitude and CP-2 relative coordinates

Radar	Latitude (deg min sec)	Longitude (deg min sec)	Elev (m)	CP-2 Coordinates	
				X (km)	Y
CP-2	39 59 37	104 59 39	1602*	0	0
CP-3	39 53 34	104 49 41	1570*	14.15	-11.19
CP-4	39 45 53	104 52 19	1619*	10.43	-25.45

\*Height to center of beam.

Table 3.2  
NCAR Doppler radar characteristics for JAWS

Parameter	CP-2	CP-3	CP-4
Wavelength (cm)	10.67	5.45	5.49
Pulse duration ( s)	0.4 to 1.5	1.0	1.0
Avg. power* (dBm)	59	55	55
Pulse repetition frequency (Hz)	960 & 480	1666 & 1250	1666 & 1250
Antenna diameter (m)	8.534	3.658	3.658
System gain (dB)	43.9	43.0**	41.0***
Beamwidth (deg)	0.97	1.17	1.09
Minimum detectable signal at 10 km (dBz)*	-25	-10	-24
velocity	-25	-23	-24

\*Representative values

\*\*Radar dome off

\*\*\*Radar dome on

Table 3.3  
Radar system parameters for data acquisition during JAWS

Parameter	CP-2	CP-3	CP-4
No. of samples in estimate	32,64,....,2048	32,64,....,2048	32,64,....,2048
No. range gates	256,512,768,1024	512	512
Azimuth scan rate (deg/sec)	0-15	0-35	0-35
Min. elev. angle increment (deg)	0.1	0.1	0.2
Range gate spacing (m)	90-600	150-240	150-240
Max. unambiguous range (km)	150 & 300	90 & 120	90 & 120
Max. unambiguous velocity (m/s)	+25.7 & +12.8	+22.6 & +17.0	+22.8 & +17.2

# JAWS NETWORK 1982

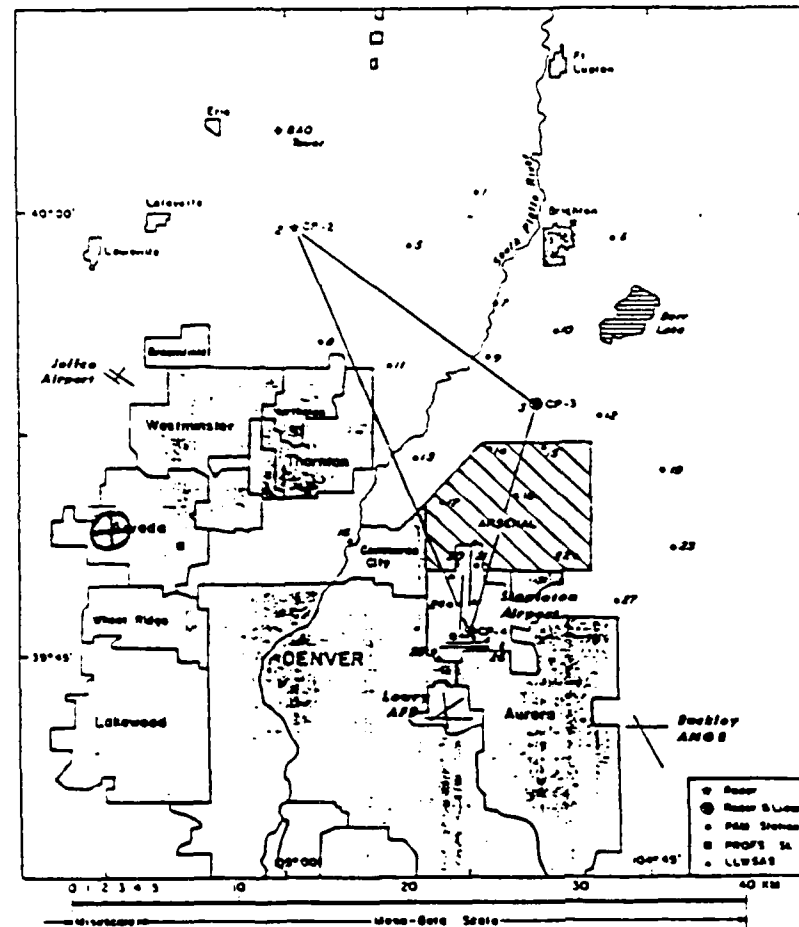


Fig. 3.4 Map illustrating JAWS Project facilities situated in the vicinity of Denver's Stapleton International Airport (after McCarthy et al., 1983).

1983). This coincides with the decrease in temperature-dewpoint spread at 500 mb. From 500 mb the sounding is almost moist adiabatic to 450 mb where a small inversion exists. A parcel lifted moist adiabatically from 530 mb would wipe out this inversion to 280 mb. Thus with very little forced lifting, a parcel could easily rise from the surface to 270 mb (8.4 km AGL). Surface temperature was 30 C and the lapse rate was nearly dry adiabatic from the surface to 600 mb. This sounding is similar to the composite microburst sounding presented by Brown et al. (1982).

The Program for Regional Observing and Forecasting Service (PROFS) noted early in the day the potential for the production of dry-type microbursts. This proved to be the case with 7 microbursts identified during that day. The dry mid-level and low-level conditions were conducive to the enhancement of downward moving air when evaporative cooling in the sub-cloud region increased negative buoyancy (Srivastava, 1985).

### 3.2 Doppler Measurements

The data used in this study were obtained from two Doppler radars used in the JAWS project. These radars, designated CP2 and CP4, were located in the area of Stapleton International Airport in Denver, CO. (Fig. 3.4). The technical parameters of these radars



and the microburst of this study. CP2 and CP4 nearly form the ideal configuration to take advantage of this situation. The more orthogonal the radar-storm-radar angle the less the effect of variance of the sensed radial wind on the possible range of the true wind. Figure 3.1 shows that a wider range of true winds is possible when the angle between the storm and the radars is decreased.

In both cases ( Fig. 3.1) the two radars sense the same vector wind plus or minus the same variance. Any vector wind originating at point P and terminating within the outlined area will produce the correct sensed radial wind plus or minus the variance. It is evident from the size and shape of the areas that when the angle between the radars and the storm is 90 degrees the size of the area is minimal.

### 3.3 Data Analysis Procedures

The Doppler data were brought back from NCAR having been edited as described in the previous section. They consisted of radial velocity, standard deviations of radial velocity (referred to as spectral width hereafter), and reflectivities. The spectral widths were of no immediate use due to the random errors introduced during the collection procedure (Elmore, 1984; private communication).

Lin and Pasken (1982) discussed six stages in analysis of the Doppler data. They are:

- 1) Desired data are collected and ordered according to time and altitude.

- 2) Errors are deleted and aliased velocities, or "folded velocities", are corrected.

- 3) Data are then interpolated on to the three-dimensional grid array.

- 4) The three-dimensional wind field is computed from dual-Doppler radar data; u, v, and w components are then calculated from gridded fields of reflectivity and radial velocity.

- 5) Kinematic variables are derived, and

- 6) These data are displayed.

The specific detail of each of these steps will be covered with the rationale for the choices of technique used in this study.

### 3.3.1 Extraction of desired parameters

The data brought back to St. Louis University consisted of a single magnetic tape for each radar. The first step was to reduce this vast quantity of data into a more compact and usable form for the PDP 11/70 computer. The data were first scanned and any data falling outside our predefined area of interest were eliminated. Next the data were converted from

spherical coordinates centered on each radar to an orthogonal coordinate system centered on radar CP2. During this step the location of the data was translated using storm motion and actual observation time of the individual ray scans. Finally, the data were "cut" horizontally in relationship to the desired analysis levels. A slab, 0.5 km thick, centered on each of the analysis levels was defined and all observations within that slab were consolidated into a single file. The choice of .5 km was dictated by need to have enough data points to satisfy the Barnes criteria for minimum number of observations (Barnes, 1973). This file was further reduced by limiting the actual areal coverage of the observations (Fig. 3.5).

### 3.3.2 Quality control of extracted parameters

It is important that the data be rendered consistent with the known features of the storm. The quality control checks used to insure this consistency were as follows:

- 1) All reflectivities were checked for values greater than 20 dBz. This value corresponds well to the cloud boundary. In cases where the reflectivity was less, the observation was flagged as suspect, but not eliminated from the data base.

- 2) All velocities were again checked for folding. This involved objectively computing radial and cross-

# JAWS NETWORK 1982

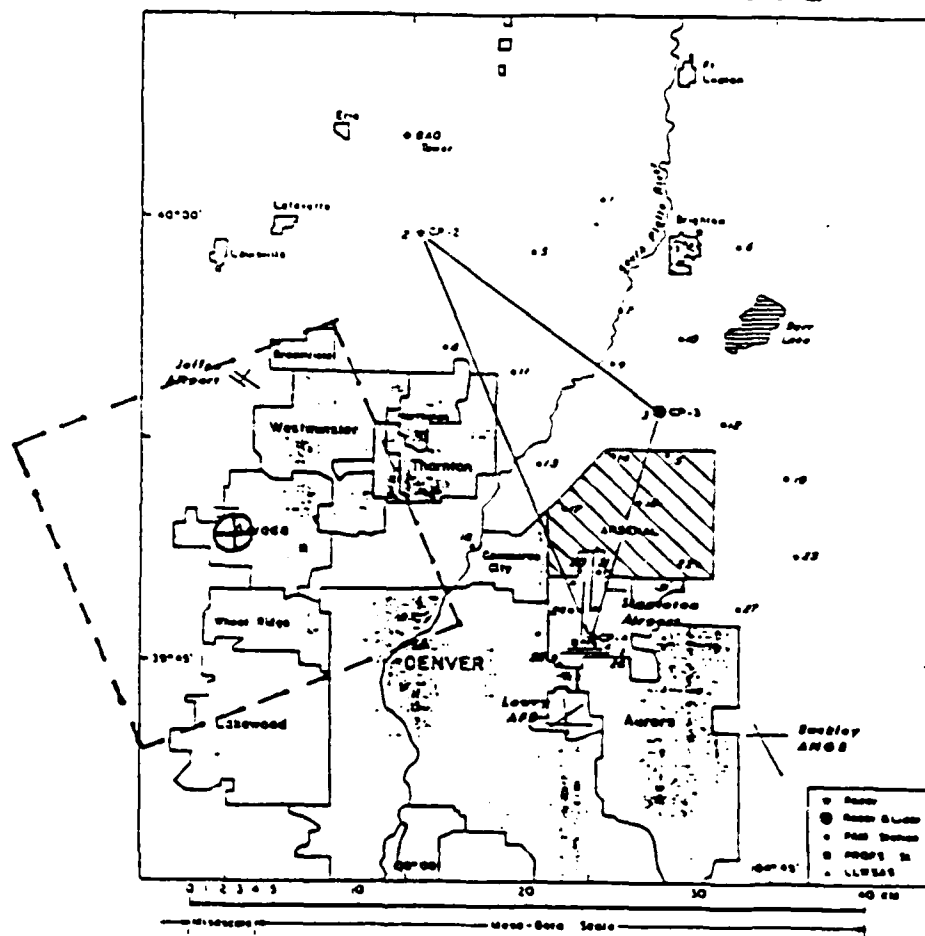


Fig. 3.5 As in Fig. 3.4 but including analysis grid. Grid is 20 km by 20 km.

beam shear and comparing these to maximum allowable values. In cases where the shear was excessive, the suspect data were unfolded. Finally the unfolded velocities were subjectively checked in areas which appeared suspicious.

3) At this point no quality control checks were considered for the spectral widths.

4) Finally, the velocities were checked in conjunction with reflectivities and the apriori knowledge of storms of this type and the environmental conditions to insure against gross errors which might be caused by non-hydrometer targets within the radar scan, such as birds, insects, planes, etc.

### 3.3.3 Interpolation of the extracted parameters to grid

The actual steps required to analyze the data will be presented here. In order to obtain as consistent a set of data as possible, at each step the data were subjected to both objective error analysis and scrutiny.

#### 3.3.3.1 Collection and ordering of desired data

This procedure was basically completed with the cutting of the data in the horizontal. However, a correction was applied to account for the time difference between the different sweeps which made up the

horizontal slab of observations. The entire volume scan for both radars began at 16:46:15 MDT and ended at 16:48:15 MDT.

Wilson (1983) suggested a temporal correction scheme which also accounted for the fact that the radial velocity is a vector quantity and not a scalar. As such, any correction in space would also require a realignment of the vector to maintain its length and sense. In situations where the elevation angles of the radar are high, this can result in an error in the corrected velocities. However, in this study, the maximum horizontal wind error would be less than  $1.0 \text{ m s}^{-1}$ .

Parsons et al. (1983) employed an advection correction scheme suggested by Gal-Chen (1982) to account for the temporal differences in scanning the storm volume. Vertical velocity errors were reduced by an order of magnitude. They noted that the error on computed vertical velocities was a function of three parameters; namely, the scanning time, the advection velocity, and the correction velocity. Increased scanning time increased the errors in vertical velocity both in the corrected and uncorrected cases. It also threatens the assumption of steady state used in studies involving only one time scan. Similar results also held for the advection velocity.

The errors in vertical velocity seemed to be negatively correlated with corrected speed, i.e., higher vertical velocities produced more negative errors. However, errors were still much smaller for corrected cases when compared to uncorrected cases. They concluded that "... considerable improvement can be obtained in the derived wind fields even when the advection velocity is not exactly known."

The advection scheme was employed to correct the data location. The difference between the "storm observation time" and the actual data observation was multiplied by the mean storm motion to produce a horizontal offset. This was then added to the horizontal coordinate to produce a new location for the data point, so that

$$x_{\eta} = x_0 - (t - t_0) cx \quad (3.3.1)$$

$$y_{\eta} = y_0 - (t - t_0) cy \quad (3.3.2)$$

where

$(x_0, y_0)$  = uncorrected datum coordinates,

$(x_{\eta}, y_{\eta})$  = corrected datum coordinates,

$(cx, cy)$  = mean storm velocity in x and y direction,

$t_0$  = mean storm observation time (averaged over the starting and ending times), and

$t$  = actual radar time for datum point.

### 3.3.3.2 Interpolation scheme

There are a number of techniques available for transferring the data to a grid. Lhermitte (1970) utilized a COPLAN technique in a cylindrical coordinate system. The advantage of this system was that Cartesian wind components could be synthesized directly from cylindrical components. By contrast, many of the studies involving JAWS data use the Cartesian grid, e.g., Mueller and Hildebrand (1983), Kessinger et al. (1983), Rodi et al. (1983), etc. In keeping with this precedent, the Cartesian grid system is utilized in this study. There are a number of drawbacks to this choice. The first involves the necessity to convert radial velocities from two radars to horizontal velocities. This involves the solution of a hyperbolic partial differential equation to derive the vertical wind (Armijo, 1969). The second and perhaps more bothersome problem involves transferring winds collected on a conical surface to a horizontal plane.

When the data are cut into slabs the location of data points within that slab is not random. As a result, the technique for evaluating the variable at grid points must be carefully considered. There are many techniques for evaluating non-gridded data at grid points. Only those which involve some averaging process of the points "close" to the grid point will



be considered.

The simplest of these involves a direct unweighted average of all points within a specified radius. This technique is inappropriate since it smooths the data far too much, removing many of the mesoscale features of interest. Cressman (1959) suggested a scheme which weighted the influence of the data in relation to the distance from the grid point:

$$\eta = \frac{R^2 - r^2}{R^2 + r^2} \quad (3.3.3)$$

where  $R$  is the maximum radius of influence and  $r$  is the actual distance from the grid point to the datum point. This scheme has been used by Mueller and Hildebrand (1983), Kessinger et al. (1983) and Wilson et al. (1984). The primary criticism of this technique is the large amount of influence this technique exerts on a grid point at great distances and the requirement from multiple passes at different radii of influence to reintroduce the effects of smaller scale features. Perhaps even a more pointed criticism is the inability to produce a "response curve" similar to that found with the Barnes technique. By choosing differing radii, the actual amplitude recovered from a specific wave number is not readily apparent. Thus, the investigator must be careful when discussing features which may be below the range of discernible wave

numbers.

Barnes (1964) developed a weighted influence function which partially negated the problems of the Cressman scheme. The result was an exponential weighting function which could be reapplied successively to obtain a gridded set of data. It still, however, required the use of multiple passes, i.e.,

$$\eta = \exp\left(\frac{-Er^2}{R^2}\right) \quad (3.3.4)$$

where

$R$  is the radius of influence,

$r$  is the distance between the datum point and the grid point, and

$E$  is the amount of influence of the weighted data we wish to represent.

When  $E = 4.0$ , it implies that we have represented 98 percent of the influence of any datum within a circular region whose radius is  $R$ . This scheme was improved by Barnes (1973) reducing the number of passes to 2, namely,

$$\eta = \exp\left(\frac{-Er^2}{R^2\gamma}\right) \quad (3.3.5)$$

where  $R$ ,  $r$ , and  $E$  are as above and  $\gamma$  is a parameter between 0 and 1 which represents confidence in the data (Koch et al., 1984).

As stated above, one of the advantages of the Barnes scheme is the ability to compute the scheme's response to various wave number inclusions in the

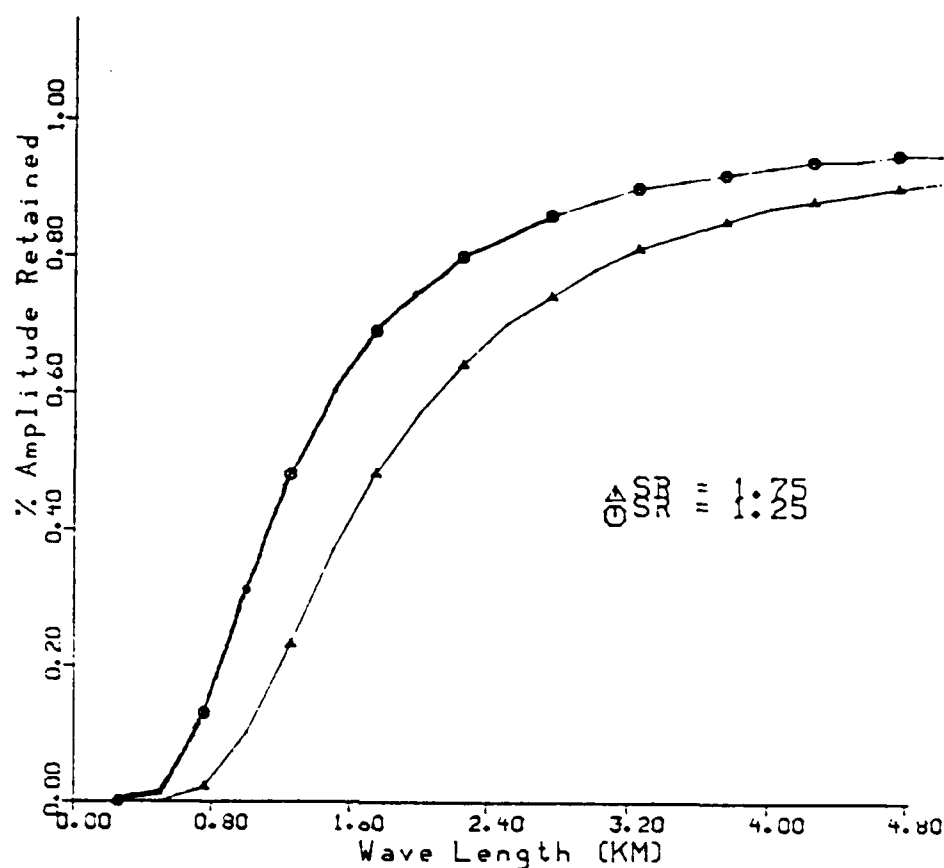
final gridded data set. Equation (3.3.6)

$$D' = D_o (1 + D_o^{Y-1} - D_o^Y) \quad (3.3.6)$$

shows the computational form of the response curve and Fig. 3.6 shows the final response curve for the two scan radii,  $R = 1.25$  km and  $R = 1.75$  km, used in this study.

In most of the studies in the literature, the Barnes scheme has been applied primarily to the horizontal plane with either the  $p$  or  $z$  coordinate held constant, e.g., Lin and Pasken (1982), Wirsing (1985), and Lin et al. (1985). An in-depth discussion of the Barnes' gridding technique as it was used in this study can be found in Appendix A.

Employment of the horizontal gridding scheme requires that all data points within the slab be projected directly to the level of interest. Since the data are not randomly located within the slab but rather in intersection bands, the resultant wind field contains features which appear as wave patterns. These patterns are fictitious and are the result of speed and directional wind shear in the vertical. Figure 3.7 shows this phenomenon. Point one obtains all its influence from the points to the right which in actuality lie above the plane, while the point on the left obtains all its influence from the points to



#### RESPONSE CURVE FOR BARNES SCHEME

Fig. 3.6 Final response curve from Barnes' gridding scheme for  $R = 1.25$  km and  $1.75$  km.  $\Gamma = 0.3$ . Ordinate represents the wavelength and abscissa is the percentage of original amplitude retained after the gridding process.

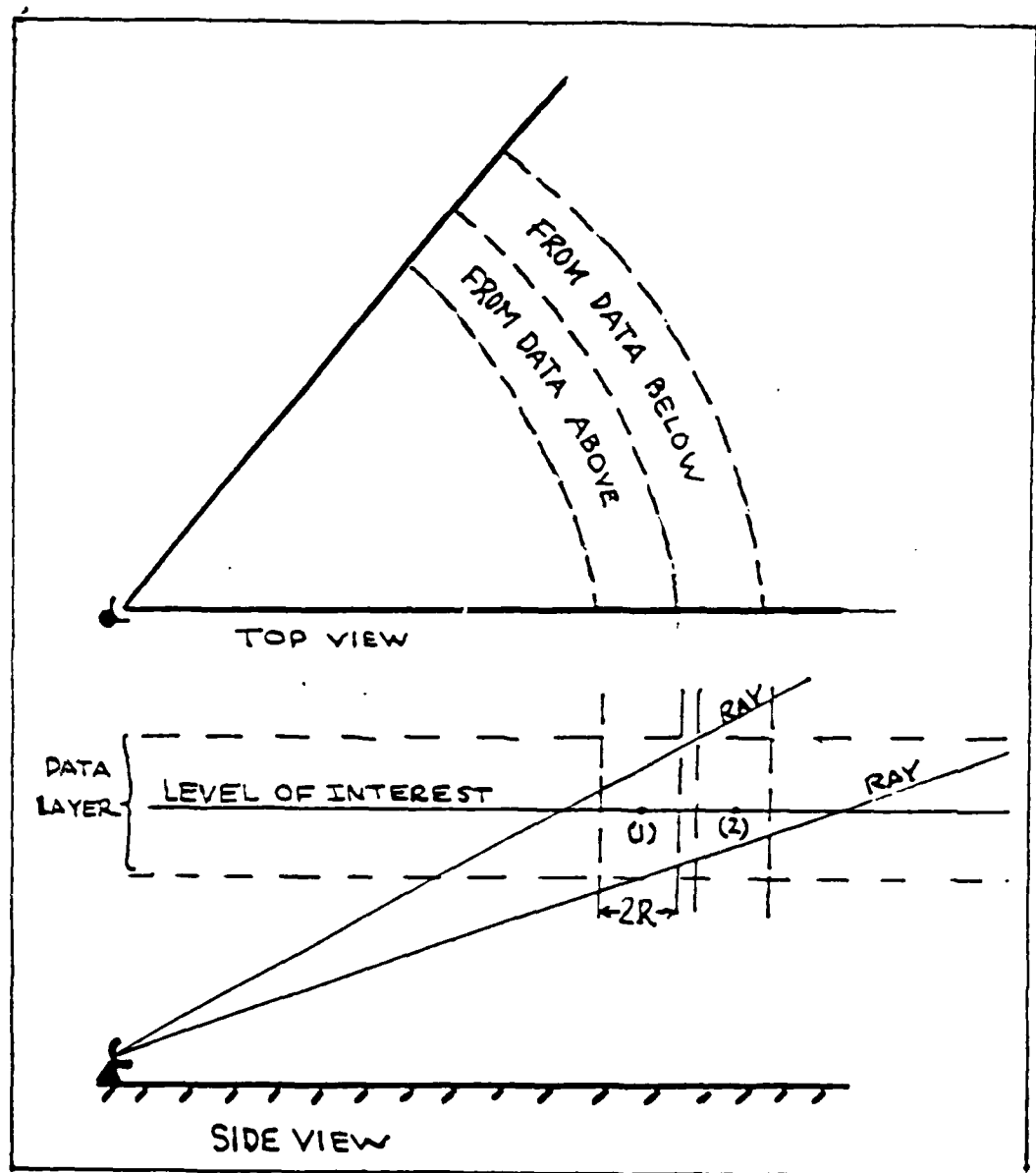


Fig. 3.7 Plan and side view illustrating banding of the data which results from horizontal slicing of conical data

the left which lie below the plane. The result is that the vertical directional and speed shear is transferred to the horizontal plane.

Extension of the Barnes scheme to three dimensions has not appeared extensively in the literature and where it has there is considerable variation in the method for handling the vertical coordinate. Regan (1984; personal communication) utilized a weighting function which employs a spherical volume of influence. Wang (1984; personal communication) utilized an elliptical volume in which the vertical axis is smaller than the horizontal axis and the horizontal axes are equal. Barber (1983) suggests a weighting function of the form

$$\eta = \frac{1}{4\pi k D} \exp\left(-\frac{d_h^2}{4K} - \frac{z_v^2}{4D}\right) \quad (3.3.7)$$

where

$k$  and  $D$  are weight parameters controlling horizontal and vertical smoothness, respectively, and

$d_h$  and  $z_v$  are horizontal and vertical distances, respectively, between observation and a given gridpoint.

This essentially results in an elliptical weighted volume, with  $K$  and  $D$  defining the major (horizontal)

and minor (vertical) axis, respectively. On the other hand, Wirsing (1985) attempted to solve the problem in a completely different manner. Along with gridding the data in a manner similar to the two-dimensional scheme, he also gridded the heights of the actual data points. The gridded values were then assigned to the gridded height and the values at the level of interest were interpolated in the vertical from the gridded profiles. This technique eliminates the requirement to determine whether a datum point is within an elliptical volume and adds only one additional run through the gridding routine and one additional storage array. This technique was employed in the present study. A number of different fitting polynomials were studied and the linear fit seems to be the most sensible. We feel that the order of the polynomial used should be inversely proportional to the standard deviation of the interval of adjacent data points for the independent variable. Since the intervals are of non-uniform size, the simplest polynomial provides the most reliable approximation.

#### 3.4 Synthesis of three-dimensional wind field

The method of processing Doppler data to obtain three-dimensional wind fields and thermodynamic information are separate procedures in this study, but the re-

covery procedures for the thermodynamic variables depend on the procedures used to derive the wind field. Lhermitte (1968) and Armijo (1960) first suggested methods of recovering the 3-dimensional wind field patterns from multiple Doppler radar data. Lhermitte (1968) developed a technique referred to as the COPLAN scheme. This scheme utilizes cylindrical coordinates and processes the wind field on tilted planes. The principle drawback of the COPLAN scheme seems to be the requirement that the volume be scanned in unison by two radars. Zrnic and Doviak (1984) provided a condensed discussion of this technique. They noted that it is easier to compute the vertical velocity using the COPLAN technique than any other principle method available, e.g., Armijo (1969).

The Armijo (1969) technique for 2 Doppler radars involves direct synthesis of the 3-dimensional wind field in Cartesian coordinates. The principle drawback is the need to solve an inhomogeneous hyperbolic partial differential equation to obtain vertical wind. However, it does not have the strict synchronous scan requirement, rather relying on a temporal adjustment scheme to adjust for nonsynchronous scanning. Since most of the analysis presented in this study employed the interpolation scheme in a Cartesian coordinate system, the Armijo (1969) method of producing the 3-



dimensional wind field is used.

Considering the geometry of two radars looking at the same storm, Armijo (1969) expressed the radial velocities as sensed by the radars as a function of the three-dimensional wind field by

$$V_{R_1} = \frac{u(x-x_1) + v(y-y_1) + (w+V_t)(z-z_1)}{R_1} \quad (3.4.1a)$$

$$V_{R_2} = \frac{u(x-x_2) + v(y-y_2) + (w+V_t)(z-z_2)}{R_2} \quad (3.4.1b)$$

where

$R_1$  is radial distance from radar 1 to target,

$R_2$  is radial distance from radar 2 to target,

$V_{R_1}$  is radial velocity measured by radar 1,

$V_{R_2}$  is radial velocity measured by radar 2,

$(u,v,w)$  are components of true wind in  $x,y,z$  directions, respectively,

$(x,y,z)$  is actual location of the target w.r.t. origin,

$(x_1,y_1,z_1)$  is location of radar 1 w.r.t. origin,

$(x_2,y_2,z_2)$  is location of radar 2 w.r.t. origin,

and

$V_t$  is mean terminal velocity of hydrometeors within the target volume.

With the location of the radars and the measured radial velocities known, (3.4.1) results in 2

equations in 4 unknowns, namely,  $u$ ,  $v$ ,  $w$ , and  $V_t$ . In order to solve for  $u$ ,  $v$ , and  $w$ , it is necessary to formulate two additional equations. Using the reflectivity, a terminal velocity-reflectivity equation can be formulated relating the terminal velocity of the target,  $V_t$ , to reflectivity,  $Z_e$ . A number of investigators have developed such empirical formulae including Rogers (1964), Sekhon and Srivastava (1971), Atlas et al. (1973), Battan (1973), and Martner (1975). Foote and du Toit (1969) proposed a density height correction to account for differences in terminal fall speed of specific sized particles due to differences in air density through which the particles are falling. The Martner formula which was derived for High Plains thunderstorms along the Foote and du Toit correction are employed in this study, i.e.,

$$V_t = -5.70 Z_e^{0.04} \left( \frac{\bar{p}_0}{\bar{p}} \right)^{0.4} \quad (3.4.2)$$

where

$V_t$  is raindrop terminal velocity,

$Z_e$  is equivalent radar reflectivity factor,

$\bar{p}_0$  is standard surface density, and

$\bar{p}$  is actual environmental density.

This formula has appeal beyond the fact that it was developed for High Plains thunderstorms. In studies where the reflectivity is small or may be

questionable, a form of this equation which is relatively insensitive to errors in  $Ze$  is desirable. Formulas which utilize small exponents tend to be less sensitive than those which utilize large exponents. Table 3.4 compares the values for a number of equations and a variety of reflectivities. The percentage change from 10-60 dBz reveals that while the values are absolutely larger, the percentage change is smaller. Thus the Martner's formula is chosen for this study.

The final equation is the anelastic continuity equation:

$$\frac{\partial(\bar{\rho}_a(z)w)}{\partial z} = -\nabla_H \cdot (\bar{\rho}_a(z)\vec{V}_H) \quad (3.4.3)$$

where

$\bar{\rho}_a(z)$  is adiabatic-hydrostatic density, a function of height only, and

$\vec{V}_H$  is horizontal velocity vector.

Equations (3.4.1), (3.4.2), and (3.4.3) form a complete set of equations with four unknowns,  $u$ ,  $v$ ,  $w$  and  $V_t$ . The solution can be obtained from a standard iteration procedure from one level to another. The vertical wind,  $w$ , is consistent with the horizontal winds through the use of the anelastic continuity equation. In practice, these equations are modified and solved for  $u$ ,  $v$ , and  $w$ . Section 3.4.1 outlines this procedure in detail.

Table 3.4

Terminal velocity in m s versus reflectivity in dBz

Reflectivity (dBz)	Rogers (1964)	Atlas (1965)	Sekhon (1971)	Martner (1975)
10	-4.5	-3.4	-4.9	-6.3
20	-4.8	-3.7	-5.1	-6.4
30	-4.9	-3.9	-5.2	-6.5
40	-5.0	-4.0	-5.2	-6.6
50	-5.1	-4.1	-5.3	-6.7
60	-5.1	-4.2	-5.3	-6.7
% Change	.13	.24	.08	.06

(Rogers -3.84Z<sup>0.07</sup>), (Atlas -2.65Z<sup>.114</sup>),  
 (Sekhon -4.32Z<sup>.052</sup>) and (Martner -5.72<sup>0.04</sup>)

The anelastic continuity equation, Eq. (3.4.3), requires the adiabatic density  $\bar{\rho}_a$ . Beginning with the first law of thermodynamics

$$dQ = c_p d\bar{T} - \bar{\alpha} d\bar{P} \quad (3.4.4)$$

where

$\bar{\alpha}$  is specific volume,

$c_p$  is specific heat at constant pressure,

$d\bar{T}$  is change in temperature,

$d\bar{P}$  is change in pressure,

$dQ$  is amount of internal heat added to or lost from the system, and the overbar indicates environmental (basic) state.

From the adiabatic assumption  $dQ = 0$ , one has

$$0 = c_p d\bar{T} - \bar{\alpha} d\bar{P} \quad (3.4.5)$$

The hydrostatic equation gives

$$\frac{d\bar{P}}{dz} = -\bar{\rho} g \quad (3.4.6)$$

Substituting Eq. (3.4.6) into Eq. (3.4.5) yields

$$\frac{d\bar{T}}{dz} = -\frac{g}{c_p} \quad (3.4.7)$$

Replacing temperature using the equation of state

$$\frac{1}{\bar{\rho} R_d} \frac{d\bar{P}}{dz} = \frac{\bar{T}}{\bar{P}} \frac{d\bar{P}}{dz} - \frac{g}{c_p} \quad (3.4.8)$$

Rearranging Eq. (3.4.8) yields

$$\frac{d \ln \bar{P}}{dz} = -\frac{g c_p}{\bar{T} c_p R_d} \quad (3.4.9)$$

Integrating this equation from  $Z_i$  to  $Z_{i+1}$  and noting the value of  $g = 9.8 \text{ m/s}^2$ , we arrive at

$$\bar{\rho}_{i+1} = \bar{\rho}_i \exp\left(\frac{-24.3207}{T_{i,i+1}}\right) \quad (3.4.10)$$

where  $T_{i,i+1}$  is the mean environmental virtual temperature between layers  $i$  and  $i+1$ . To solve for  $\bar{\rho}_i$ , we first compute the value of  $\bar{\rho}_0$  from the surface observation taken at 1800 MDT, 14 July 1982 in Denver, CO.

To determine the validity of this technique for computing density with the assumptions made, values of density were computed using Eq. (3.4.10) and the equation of state. Table 3.5 shows these computations as well as the correction factor of Foote and du Toit using the different density values.

### 3.4.1 Synthesis of wind components

To solve for the wind components we begin with Eq. (3.4.1). Multiplying (3.4.1a) by  $(x-x_2)$  and (3.4.1b) by  $(x-x_1)$  and rearranging, we have

$$V = \frac{\Delta x_1 R_2 V_{R2} - \Delta x_2 R_1 V_{R1} + (w + V_t)(\Delta x_2 \Delta z_1 - \Delta x_1 \Delta z_2)}{\Delta x_1 \Delta y_2 - \Delta x_2 \Delta y_1} \quad (3.4.11a)$$

Similarly multiplying (3.4.1a) by  $(y-y_2)$  and (3.4.1b) by  $(y-y_1)$ , we can obtain

$$U = \frac{\Delta y_1 R_2 V_{R2} - \Delta y_2 R_1 V_{R1} + (w + V_t)(\Delta y_2 \Delta z_1 - \Delta y_1 \Delta z_2)}{\Delta y_1 \Delta x_2 - \Delta x_1 \Delta y_2} \quad (3.4.11b)$$

Table 3.5  
Comparison of Density Computation Methods

Pres mb	kg/m <sup>3</sup>	F & D	kg/m <sup>3</sup>	F & D
835	0.954	1.096	1.013	1.067
700	0.843	1.151	0.936	1.104
500	0.658	1.271	0.853	1.145
400	0.553	1.363	0.775	1.191
300	0.440	1.493	0.699	1.240
250	0.384	1.576	0.628	1.295
200	0.320	1.695	0.562	1.354

where

$$\Delta x_i = x - x'_i,$$

$$\Delta y_i = y - y'_i,$$

$$\Delta z_i = z - z'_i,$$

and  $i = 1$  or  $2$ .

Equations (3.4.11a) and (3.4.11b) replace those of (3.4.1) and along with (3.4.3) and (3.4.4) form a complete set of equations.

To obtain the vertical velocity by downward integration, the kinematic boundary condition requires that  $w = 0$  at the top boundary. This height was chosen by assuming that the storm top could be defined by the 20 dBZ envelope. At the level actually chosen as the storm top,  $Z_t = 8.5$  km, the maximum reflectivity was less than 20 dBZ. To avoid the concern that perhaps the vertical velocity at the storm top was not in fact zero, a cap was constructed at 0.5 km above the highest point in the storm. It was assumed that  $w$  was actually zero at this height, 9.0 km. Next the divergence for the storm top level is computed from (3.4.11a) and (3.4.11b) assuming that  $w=0$  for this level. A solution for vertical velocity is obtained for the second level below the storm top, at 8.0 km. Using these values of vertical velocity and the fact that the vertical velocity is actually zero at 9.0 km, the "second guess" of the vertical velocity is made



for the storm top level by averaging the vertical velocities from 9.0 and 8.0 km. This is then compared to the "first guess" of the velocities at 8.5 km. This iterative process is continued until the "nth guess" - "n-1th guess" is within a specified tolerance level for all grid points. Rodi et al. (1983) used this scheme with upward integration technique iterating until the variation in divergence is below a threshold value. However, they continue to utilize this procedure throughout the volume. Lin and Pasken (1982a,b), and Wirsing (1985) applied a similar technique except they began at the top of the storm and integrated downward. The above technique was only used to obtain the vertical velocity at the topmost level. From that point, standard downward integration procedures were used.

At this point it is germane to address the use of upward integration. Many investigators, e.g., Lin and Pasken (1982a,b), Ray et al. (1980), Nelson (1980) and Brown and Nelson (1982), suggested that downward integration from the top of a storm volume will produce errors of less magnitude than upward integration from the bottom of the storm volume.

By integrating the anelastic continuity equation to obtain the vertical velocity at the next level, one can see that errors computed early in the downward

integration process are initially multiplied by smaller density terms. While integrating upward, these errors would be influenced by the larger density terms near the surface, i.e.,

$$w_1 = \frac{\bar{\rho}_{a2}(z)}{\bar{\rho}_{a1}(z)} w_2 + \frac{\bar{\rho}_{a12}(z)}{\bar{\rho}_{a1}(z)} (\nabla_2 \cdot \vec{V}_H) \Delta z \quad (3.4.12)$$

where

$w_2$  is vertical velocity at upper level,

$w_1$  is vertical velocity at lower level,

$\nabla_2 \cdot \vec{V}_H$  is horizontal divergence averaged vertically through the layer of interest,

$\bar{\rho}_{a1}(z)$  is basic density at lower level,

$\bar{\rho}_{a2}(z)$  is basic density at upper level,

$\bar{\rho}_{a12}(z)$  is mean density averaged vertically between two levels.

In this study, data were available through the entire volume of the storm and downward integration was used.

### 3.5 Correction of Wind Components using Variational Analysis

As indicated previously, computation of vertical velocity was accomplished using downward integration of the anelastic continuity equation. This technique minimizes errors due to various computational considerations such as derivative formulation and

boundary considerations, and errors in data. Errors in the derived vertical velocity are generally greatest near the surface since they tend to be cumulative. Techniques which correct these errors are generally based on a linear distribution of the surface error. The method suggested by O'Brien (1970) is one such technique available in which the error variance is assumed to be a linear function of height (or pressure). Another scheme suggested by Sasaki (1970) involves the use of the calculus of variation.

Ziegler et al. (1983) employed this technique in a study using two and multiple radars. A more complete discussion of this technique and the formulation of the Euler-Lagrange equations is given in Appendix B. A similar correction technique was applied to this data set. The functional to be minimized is

$$J = \int_{z_t}^0 \int_{y_x} \int \left\{ \alpha^2 (u - \hat{u})^2 + \beta^2 (v - \hat{v})^2 + \lambda \nabla_3 \rho_0 \vec{W} \right\} dx dy dz \quad (3.5.1)$$

where

$\lambda$  is Lagrange multiplier,

$\hat{u}$  denotes observed data, and

$\alpha, \beta$  are two weighting factors.

The choice of weighting factors varies. Ray et al. (1980) and Lin et al. (1985) used the uncertainties in the u and v components to determine the

weighting factors in the following manner:

$$\sigma_u^2 = (2\alpha^2)^{-1} ; \quad \sigma_v^2 = (2\beta^2)^{-1} \quad (3.5.2)$$

The actual computation of  $\sigma_u^2$  and  $\sigma_v^2$  were similar to computation of the horizontal wind component equations of Armijo (1969) with  $\sigma_w^2$  set to zero. Wilson et al. (1984) suggested another method which seems to completely remove any dependence on the sensed data and is related only to the relative location of the radar and an initializing assumption about the values of  $\sigma_{R_1}^2$  and  $\sigma_{R_2}^2$ . This technique is employed in this study and is further discussed in Appendix C.

The equations used in the adjustment scheme were

$$u = \hat{u} + \bar{f} \sigma_u^2 \frac{\partial \lambda}{\partial x} \quad (3.5.3)$$

$$v = \hat{v} + \bar{f} \sigma_v^2 \frac{\partial \lambda}{\partial y} \quad (3.5.4)$$

$$(\nabla_3 \cdot (\bar{\rho} \vec{V}_3)) = 0 \quad (3.5.5)$$

Equations (3.5.3) and (3.5.4) form the Euler-Lagrange equations used in the variational correction technique. Equation (3.5.5) is the anelastic continuity equation which acts to constrain the solution. Using equations (3.5.3) and (3.5.4), we arrive at the integral elliptical equation

$$\int_{z_t}^0 \left( \frac{\partial (\bar{f} \sigma_u^2 \frac{\partial \lambda}{\partial x})}{\partial x} + \frac{\partial (\bar{f} \sigma_v^2 \frac{\partial \lambda}{\partial y})}{\partial y} \right) dz = \int_{z_t}^0 \bar{f} (D - \hat{D}) dz \quad (3.5.6)$$

where  $D$  is the "true" horizontal divergence  
 $\hat{D}$  is the computed horizontal  
 divergence  
 and  $D - \hat{D}$  is the horizontal divergence error

Equation (3.5.6) represents a Poisson type partial differential equation which can be solved via successive overrelaxation (SOR) if the right hand side of the equation is known. For this study the simultaneous relaxation method with overrelaxation coefficient equal to 1.0 was used. While the sequential overrelaxation technique may converge quicker, there is a limit to the overrelaxation value which can be used to maintain computational stability. In both techniques, if the tolerance for convergence is set to low, the number of iterations becomes large and computational instability becomes of concern. In this study tests were done to determine where computational instability became a problem. It was discovered that after about 100 iterations utilizing the simultaneous scheme results began to degrade due to computational problems. Tolerance levels were adjusted accordingly to insure that "acceptable convergence" was reached prior to 100 iterations. The convergence criteria used in this study were found to be lower than those of other studies using similar techniques, e.g.

Wirsing (1985), Lin et al. (1985).

Unfortunately, in the right hand side term only  $D$  is known. To solve (3.5.5), the anelastic continuity equation is applied to the vertically integrated horizontal mass divergence so that

$$\int_{z_t}^0 \bar{\rho} (D - \hat{D}) dz = (\bar{\rho} w_{SFC} - \bar{\rho} \hat{w}_{SFC}) - (\bar{\rho} w_{z_t} - \bar{\rho} \hat{w}_{z_t}) \quad (3.5.7)$$

Note that the three other terms on the right hand side of (3.5.7),  $\bar{\rho} w_{SFC}$ ,  $\bar{\rho} w_{z_t}$ ,  $\bar{\rho} \hat{w}_{SFC}$  are all zero by constraint and assumption. The distribution of the divergence error was assumed to be independent of height. With the aid of (3.5.6) and (3.5.7), the field of Lagrange multiplier,  $\lambda$ , could be determined assuming the natural boundary condition (Sasaki, 1970). Then horizontal components of the "true" wind were computed from (3.5.3) and (3.5.4). Finally, the vertical velocity at any height,  $z_l$ , is determined from the formula

$$w_l = \hat{w}_l - \frac{\bar{\rho}_0}{\bar{\rho}_l} \frac{\int_{z_t}^{z_l} \bar{\rho}(z) dz}{\int_{z_t}^0 \bar{\rho}(z) dz} \quad (3.5.8)$$

The derived wind field not only satisfies the kinematic boundary conditions but also satisfies the anelastic continuity equation. This internally consistent wind field is then used to recover the thermodynamic variables.

### 3.6 Computation of Thermodynamic Variables

Chong et al. (1980), Hane et al. (1981), and Gal-Chen (1982) showed that when computing perturbation quantities such as perturbation pressure, density and virtual temperature, it is absolutely necessary to use a storm-relative coordinate system. When dealing with one time period, this essentially becomes a correction for storm motion and scan time differences. However, when dealing with more than one time period, salient features such as downdraft and updraft cores, and reflectivity patterns can be used to orient the grid.

In mesoscale meteorology, it is important to retain the internal gravity waves propagating through the system, while at the same time filtering out the acoustic or sound waves. The use of the anelastic approximation of Ogura and Phillips (1962) in preference to Reynolds form of the momentum equations achieves this result and at the same time simplifies the computations. The anelastic approximation requires the hydrostatic-adiabatic assumption with density varying only in the vertical.

#### 3.6.1 Computation of perturbation pressure

The momentum equations in a moving coordinate system, see Gal-Chen (1978), can be written as

$$\frac{\partial P'}{\partial x} = F \quad (3.6.1)$$

$$\frac{\partial P'}{\partial y} = G \quad (3.6.2)$$

$$\frac{\partial P'}{\partial z} = -H - \rho'g \quad (3.6.3)$$

where

$$F = -\bar{\rho}_a \vec{\nabla} \cdot \nabla u + \left( \frac{\partial \tilde{\tau}_{1i}}{\partial x_i} \right)_{i=1,2,3} + \bar{\rho}_a 2\Omega (V \sin \phi - w \cos \phi) \quad (3.6.4)$$

$$G = -\bar{\rho}_a \vec{\nabla} \cdot \nabla v + \left( \frac{\partial \tilde{\tau}_{2i}}{\partial x_i} \right)_{i=1,2,3} - \bar{\rho}_a 2\Omega u \sin \phi \quad (3.6.5)$$

$$H = \bar{\rho}_a \vec{\nabla} \cdot \nabla w - \left( \frac{\partial \tilde{\tau}_{3i}}{\partial x_i} \right)_{i=1,2,3} - \bar{\rho}_a 2\Omega u \cos \phi + \bar{\rho}_a g \quad (3.6.6)$$

(u,v,w) are velocity components in the x, y, and z direction, respectively,

$\bar{\rho}_a$  is the basic density in the hydrostatic-adiabatic atmosphere which is approximately equal to the environmental density (Brandes, 1984; Lin et al., 1985),

$\rho'$  is perturbation density,

$P'$  is perturbation pressure,

$\tilde{\tau}_{1i}$ ,  $\tilde{\tau}_{2i}$ , and  $\tilde{\tau}_{3i}$  are turbulent momentum fluxes, and other symbols have their usual meanings.



The turbulent momentum flux terms,  $\tau_{ij}$ , are computed using the formulae by Klemp and Wilhelmson (1978):

$$\tau_{ij} = -(\overline{u'_i u'_j}) \quad (3.6.7)$$

$$-(\overline{u'_i u'_j}) = K_m \left( \frac{\partial u_i}{\partial x_j} + \frac{\partial u_j}{\partial x_i} \right) - \frac{2}{3} \delta_{ij} E \quad (3.6.8)$$

and 
$$E = K_m^2 / c_m^2 l^2 \quad (3.6.9)$$

from Smagorinsky (1963), the eddy viscosity coefficient is

$$K_m = \frac{c^2 l^2}{\sqrt{2}} \left| \frac{\partial u_i}{\partial x_j} + \frac{\partial u_j}{\partial x_i} \right| \quad (3.6.10)$$

Next we parameterize the precipitation drag term,  $q_d$ , in (3.6.6) using the formulation proposed by Douglas (1964) which relates the liquid water content to the reflectivity in  $\text{mm}^6/\text{m}^3$ .

$$q_d = \left( \frac{Z}{b} \right)^{1/a} \quad (3.6.11)$$

where  $a=1.82$  and  $b=2.4 \times 10^4$ . Substituting (3.6.7) - (3.6.10) into (3.6.4) - (3.6.6) we finally arrive at

$$\begin{aligned} \frac{\partial P_d'}{\partial x} = & -\bar{\rho}_a \nabla \cdot \nabla u + \frac{\partial \left( \frac{\bar{\rho}_a c^2 l^2}{\sqrt{2}} \left( \frac{\partial u_i}{\partial x_j} + \frac{\partial u_j}{\partial x_i} \right) \left| \frac{\partial u_i}{\partial x_j} + \frac{\partial u_j}{\partial x_i} \right| \right)}{\partial x_j} \\ & - \delta_{ij} \frac{1}{3} \frac{c^4 l^2}{c_m^2} \left| \frac{\partial u_i}{\partial x_j} + \frac{\partial u_j}{\partial x_i} \right| + f_i \end{aligned} \quad (3.6.12)$$

$$\frac{\partial P'_d}{\partial y} = -\bar{\rho}_a \mathbf{v} \cdot \nabla \mathbf{v} + \frac{\partial \left( \bar{\rho}_a \frac{c^2 \ell^2}{\sqrt{2}} \left( \frac{\partial u_2}{\partial x_j} + \frac{\partial u_j}{\partial x_2} \right) \left| \frac{\partial u_2}{\partial x_j} + \frac{\partial u_j}{\partial x_2} \right| \right)}{\partial x_j} - \frac{1}{3} \frac{c^4 \ell^2}{c_m^2} \left| \frac{\partial u_2}{\partial x_j} + \frac{\partial u_j}{\partial x_2} \right| + f_2 \quad (3.6.13)$$

$$\frac{\partial P'_d}{\partial z} = -\bar{\rho}_a \mathbf{w} \cdot \nabla \mathbf{w} + \frac{\partial \left( \bar{\rho}_a \frac{c^2 \ell^2}{\sqrt{2}} \left( \frac{\partial u_3}{\partial x_j} + \frac{\partial u_j}{\partial x_3} \right) \left| \frac{\partial u_3}{\partial x_j} + \frac{\partial u_j}{\partial x_3} \right| \right)}{\partial x_j} - \delta_{3j} \frac{1}{3} \frac{c^4 \ell^2}{c_m^2} \left| \frac{\partial u_3}{\partial x_j} + \frac{\partial u_j}{\partial x_3} \right| + f_3 - \bar{\rho}_a g \delta_{3j} \quad (3.6.14)$$

where  $\bar{\kappa}_m$  = eddy momentum mixing coefficient,  $C = 0.21$ ,  $C_m = 0.20$ , and  $\ell = (\Delta x \Delta y \Delta z)^{1/3}$  as suggested by Deardorff (1975) and  $f_1 = -\bar{\rho}_a 2\Omega(v \sin \phi - w \cos \phi)$ ,  $f_2 = -\bar{\rho}_a 2\Omega w \cos \phi$  and  $f_3 = \bar{\rho}_a 2\Omega u \cos \phi$  are the Coriolis forces.

Once the turbulent momentum fluxes have been computed, the horizontal perturbation pressure can be computed by using Eqs. (3.6.1) and (3.6.2). Differentiating (3.6.1) with respect to  $x$  and (3.6.2) with respect to  $y$  and adding yields

$$\frac{\partial^2 P'}{\partial x^2} + \frac{\partial^2 P'}{\partial y^2} = \frac{\partial F}{\partial x} + \frac{\partial G}{\partial y} \quad (3.6.15)$$

This Poisson type partial differential equation can be solved using sequential relaxation with the Neumann boundary condition. For rectangular

boundaries, we have

$$\frac{\partial P'}{\partial x} = F \quad ; \quad \text{at } x = \pm a$$

$$\frac{\partial P'}{\partial y} = G \quad ; \quad \text{at } y = \pm b$$

Gal-Chen (1978) noted that a unique solution to (3.6.15) exists only if the horizontal areal mean of  $P$ ,  $\langle P \rangle$ , is removed from  $P$  of (3.6.15). The deviation perturbation pressure ( $P'$ ) field together with the wind field are then used to retrieve deviation perturbation density and temperature fields.

### 3.6.2 Perturbation density

Once the fields of deviation perturbation pressure,  $P'_d$ , has been computed, the field of deviation perturbation density,  $\rho'_d (= \rho' - \langle \rho' \rangle)$ , can be obtained from Eq. (3.6.3) using the expression

$$(\rho' - \langle \rho' \rangle)g = -\frac{\partial P'_d}{\partial z} - (H - \langle H \rangle) \quad (3.6.16)$$

where  $\langle P' \rangle$ ,  $\langle \rho' \rangle$ , and  $\langle H \rangle$  are function of height only.

### 3.6.3 Perturbation virtual temperature

Once the fields of deviation perturbation pressure,  $P'_d$ , and deviation perturbation density,  $\rho'_d$  have been computed, the deviation perturbation virtual temperature from the horizontal mean,

$$T_{va}' (= T_v' - \langle T_v' \rangle),$$

can be computed using the perturbation equation of state

$$T_{va}' = \left( \frac{P_a'}{\bar{P}} - \frac{\dot{p}'}{\bar{P}} \right) \left( \frac{\bar{P}}{R_a \bar{\rho}} \right) \quad (3.6.17)$$

#### 3.6.4 Verification of the derived thermodynamic fields

Since the method of determining thermodynamic variables presented here is indirect, verification of the derived fields is essential. Gal-Chen and Hane (1981) suggested a verification method based on momentum checking and time continuity. The momentum checking method involves the computation of a dimensionless quantity,  $E_r$ , defined as:

$$E_r = \frac{\iint \left( \left( \frac{\partial \theta'}{\partial x} - F \right)^2 + \left( \frac{\partial p'}{\partial y} - G \right)^2 \right) dx dy}{\iint (F^2 + G^2) dx dy} \quad (3.6.18)$$

$E_r$  will be computed for each analysis level. Gal-Chen and Hane (1981) noted that while noise produces values of  $E_r > .5$ . Only values of  $E_r < .5$  can be interpreted scientifically. However, Hane and Ray (1985) pointed out that fields which produce larger values of  $E_r$ , e.g.,  $E_r \leq 1.0$ , can still contain usable information.  $E_r$  as a measure of "goodness" of fit of the derived perturbation pressure gradients and the associated wind field should be looked at in light of other

checks such as physical linkage, agreement between derived fields and vertical velocity or divergence/convergence.

The time continuity check involves inspecting the thermodynamic fields from one time period to another. If the retrieved thermodynamic fields maintain good continuity from one analysis time to the next, the field will be interpreted as reasonably accurate. Since only one time period was processed, time continuity checking was not possible in this study. Momentum checking and physical linkage were used to determine confidence in the derived fields.

## CHAPTER 4

### Error Analysis

Central to the interpretation of the results of any scientific study is an understanding of errors in those results and the mechanisms which generated them. Not only does this knowledge aid in interpreting the results more correctly but it also aids in future collection and processing of similar data.

Errors, in general, are random or non-random in nature. Those which are random are related to observational techniques, e.g., ground clutter, sidelobe contamination, sampling problems, temporal errors due to sampling differences of the radars involved, statistical probability considerations, and hardware processing errors among other things. These types of errors are very difficult to detect and almost impossible to correct. Non-random errors can be introduced from a number of sources, e.g., errors in wind field and numerical processing techniques. Numerical processing techniques include such elements as choice of boundary conditions, finite difference methods, direction of vertical integration, and errors in deduced fields due to errors in the wind field.

#### 4.1 Random Errors

Bohne and Srivastava (1976) and Ray et al. (1978a) examined random errors associated with Doppler radar wind measurements. Bohne and Srivastava (1976), using data from three Doppler radars, deduced that the theoretical accuracy of the horizontal wind was approximately  $\pm 1 \text{ m s}^{-1}$ . They noted that the accuracy of the terminal velocity,  $V_t$ , is about  $\pm 2-3 \text{ m s}^{-1}$  for rain and  $\pm 1/2 \text{ m s}^{-1}$  for snow. Ray et al. (1978a) looked at the differences in the horizontal wind fields using 2, 3, and 4 radars. Distributions of error in variances for two radars are reproduced in Fig. 4.1. Note that for the two radar case, a target located within 40 km has a standard deviation of horizontal wind uncertainty of  $< .2 \text{ m s}^{-1}$ . They note that increasing the number of radars does not appreciably reduce error. Ray et al. (1978a) deduced that errors in the horizontal wind speeds are  $< 3 \text{ m s}^{-1}$ . For a specific storm on 8 June 1974, Doviak et al. (1976) estimated errors in wind field to be 10 degrees in direction and  $1 \text{ m s}^{-1}$  in speed. Lin and Pasken (1982) utilizing a formula from Lhermitte and Miller (1970) arrived at similar values. Elmore (1982) conducted an error analysis suggested by Nelson (1980) and Nelson and Brown (1982) and obtained comparable results. A detailed error analysis was accomplished

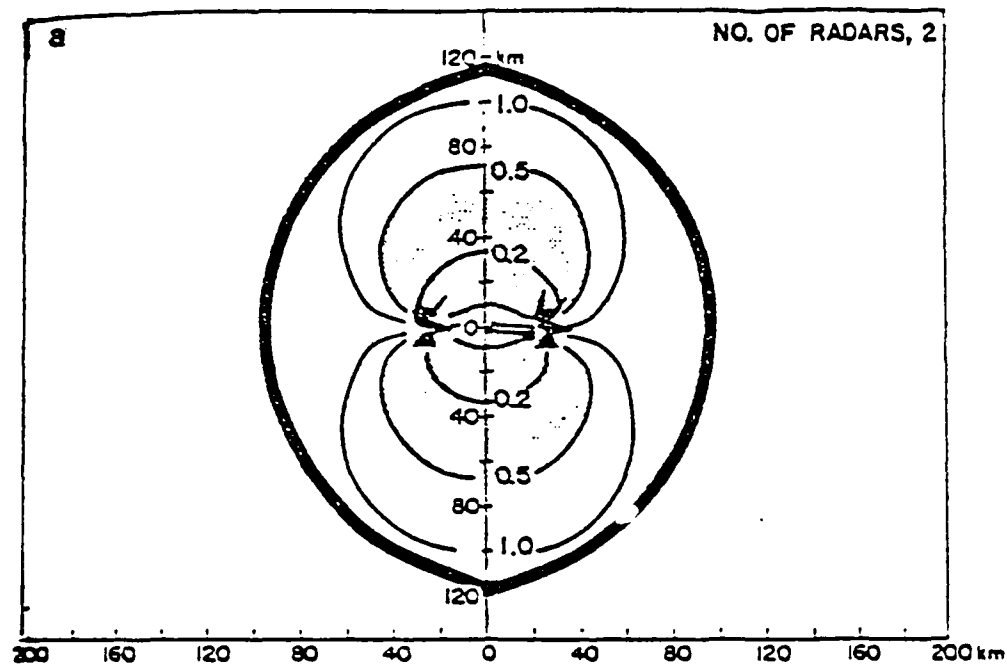


Fig. 4.1 Error analysis for horizontal fields for two radars. Axes are in kilometers. Areas inside heavy line is within 120 km of at least two radars (after Ray et al., 1978).



on results of this study and is discussed in Chapter 5.

Random errors in velocity measurements are associated with statistical probability and are difficult to discuss except theoretically. They are linked to the assumptions made about the drop size distribution within the scanned volume, the composition of the hydrometers within the scanned volume, and sampling techniques. One example involves relating the terminal fall speed of the hydrometer en masse within the scanned volume to the reflectivity. Table 3.4 shows a number of empirical  $Z - V_t$  relationships from different authors and the different values they produce for the spectrum of reflectivity values expected in this study.

Errors associated with the choice of  $Z - V_t$  function are generally more important at higher elevation angles, where the radial component of the wind reveals a larger magnitude of the vertical wind. In this study, elevation angles were small enough that this error can be neglected.

Some of the errors associated with hardware involve dropped bits, incorrect processing of the signal due to low signal to noise ratio, voltage fluctuations within the radar and problems similar to that involving the variance measurements.

#### 4.2 Non-random errors

Non-random errors can, in general, be divided into two subcategories:

- 1) Errors associated with limiting assumptions, and
- 2) Errors associated with numerical techniques.

##### 4.2.1 Errors associated with limiting assumptions

A number of limiting assumptions were made in this study. Each will be explained in the following sub-sections.

###### 4.2.1.1 Quasi-steady state storm assumption

It was assumed that both radars were scanning the same volume at the same time. Great effort was made during JAWS to coordinate the radar scanning procedures. The results were a multiple Doppler radar data set which has temporal differences between radars which were considered negligible for this study. Of importance is the problem involving reduction of the observation time needed to perform a complete volume scan. This took nearly two minutes. The solution was to correct all observations to a "storm time" by correcting the location of the observation using the time correction equations in Chapter 3. Gal-Chen (1982) suggested that this correction is necessary to reduce errors caused by storm motion. The use of (3.3.1) and (3.3.2) involve making two assumptions

AD-A170 673

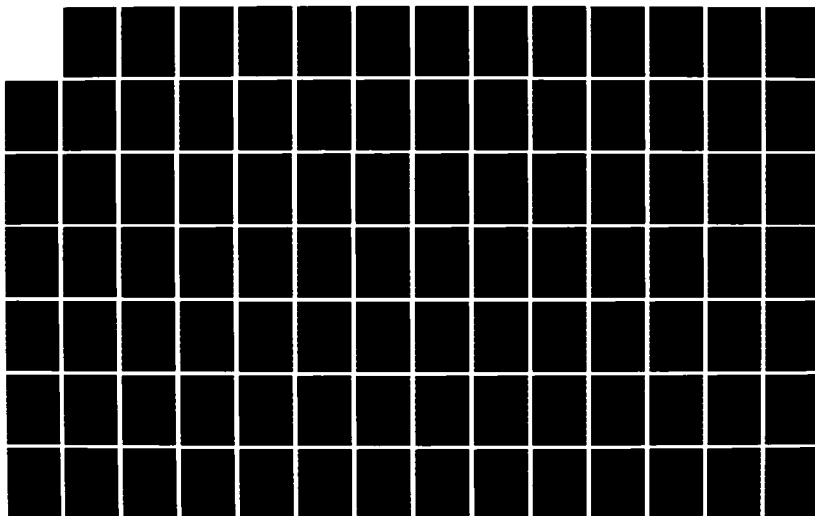
DYNAMIC AND THERMODYNAMIC CHARACTERISTICS OF A  
MICROBURST-PRODUCING STORM. (U) AIR FORCE INST OF TECH  
WRIGHT-PATTERSON AFB OH R G HUGHES 1986  
AFIT/CI/NR-86-69D

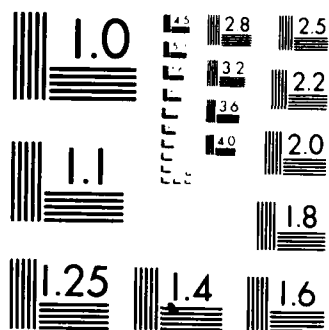
2/3

UNCLASSIFIED

F/G 17/9

NL





MICROCOPY RESOLUTION TEST CHART  
NATIONAL BUREAU OF STANDARDS-1963-A

about the state of the storm. The first assumption is that for the entire observation period the motion of the storm, as a whole, was constant. Secondly, not only was it constant, but it was moving at the same speed at all levels. Wilson et al. (1984) noted for this particular storm that the required correction was negligible for a grid size of 250 m. Inspection of the results from Wilson et al. (1984) reveals that changes in the speed of this storm near the surface were also negligible. The maximum time differences between the "storm time" and the acquisition time for any datum point is less than 80 seconds which suggests that errors in location of a datum point due to storm motion is less than one grid distance.

The quasi-steady state assumption also encompassed temporal changes in the structure of the storm. Gal-Chen (1978) suggested that when two sequential scans were available, the sensed velocity at a given point, after having been corrected spatially, could be corrected temporally. This correction, see Eq. (4.1), amounts to a linear interpolation of the change in velocity using the first and second scan times and the storm relative time

$$u(x, y, z, t) \approx \alpha u_r(x, y, z, t_k) + \beta u_r(x, y, z, t_k) \quad (4.1)$$

$$\text{where } \alpha = \frac{T - t_k}{T}; \beta = \frac{t_k}{T} \text{ for } t_k \leq T$$

The time derivative can be evaluated as

$$\left. \frac{\partial u_r}{\partial t} \right|_{t=T} = (u_r(T+t_k) - u_r(T)) / t_k \quad (4.2).$$

This procedure requires a belief that when all data points are adjusted, the result will represent the storm as it appeared at the "mean observation time". It is based on the steady state assumption for approximately 2 minutes. This technique has been employed by Lin and Pasken (1982), though in a somewhat different form, and Wirsing (1985) in a similar form.

Lin et al. (1985) examined the effect the steady state assumption had on computations of deviation perturbation pressure and deviation perturbation virtual temperature and concluded that the errors created by making the steady state assumption were of secondary importance. They also noted that the accuracy of the time tendency term depends on the "maturity" of the storm. This suggests that in order to realistically include the time tendency terms, two time periods must be analyzed, that is, parameterization of the time tendency term is questionable without knowing the "age" of the storm.

Hane et al. (1981) examined the effect of the steady state assumption on temperature retrieval using model data. Their conclusion was that while the

actual results deteriorated, the solution was judged useful if general temperature patterns were desired.

#### 4.2.1.2 Adiabatic-hydrostatic assumption on density

Table 3.5 shows the difference for densities computed from the Denver sounding, the equation of state and the first law of thermodynamics making the adiabatic and hydrostatic assumptions necessary for the use of the anelastic continuity equation. This difference has little effect on the computation of the wind field due to differences in the Foote & du Toit correction, see Section 4.2.2.2.

#### 4.2.2 Errors associated with the wind field

Some of the errors in the wind field have been discussed under the random error Section. Non-random wind errors include those associated with specific formulations of the terminal velocity equation, corrections of the terminal velocity using the Foote and du Toit correction scheme, and errors associated with subjective analysis of the horizontal wind field.

##### 4.2.2.1 Errors due to terminal velocity assumptions

In this study we have chosen to use the terminal velocity-reflectivity relationship of Martner (1976). Table 3.4 shows values for a variety of reflectivity strengths as well as a number of other possible equations. Examination of (3.11) suggests that the errors

will be at least one order of magnitude smaller than the values of  $u$ , and  $v$ . This is due to the fact that the term is multiplied by  $z - z_i^*$ , with  $i = 1$  or  $2$ , which ranges from 0-5 km, while  $x - x_i^*$  ranges from 0-30 km. This error reaches its largest magnitude for the higher elevation angles. Table 3.4 suggests that the Martner equation provides the least amount of sensitivity to errors which may be associated with  $Z$ .

#### 4.2.2.2 Errors related to Foote & du Toit correction

Foote and du Toit (1969) suggested two forms of a correction to be applied to the computed terminal velocities, namely,

$$V_d = V_{0d} 10^Y \left( 1 + 0.002 \left( 1.1 - \frac{\bar{p}}{\bar{p}_0} \right) (T - T_0) \right) \quad (4.3)$$

where

$$Y = 0.43 \log_{10} \left( \frac{\bar{p}_0}{\bar{p}} \right) - 0.4 \left( \log_{10} \left( \frac{\bar{p}_0}{\bar{p}} \right) \right)^{2.5}$$

and

$$V_d = \left( \frac{\bar{p}_0}{\bar{p}} \right)^{0.4} V_{0d} \quad (4.4)$$

where

$\bar{p}_0$  = standard surface density ( $\bar{p}_0 = 1013.25$  mb,

$T_0 = 293.16$  K), and  $\bar{p}$  = actual density.

This correction accounts for the differences in air density and the effect of this difference on aerodynamic drag of the droplets. Figure 4.2 shows the computed vertical velocities using (4.3) and (4.4), where  $V_{0d}$  is from (3.4.2), and density,  $\bar{p}$ , is



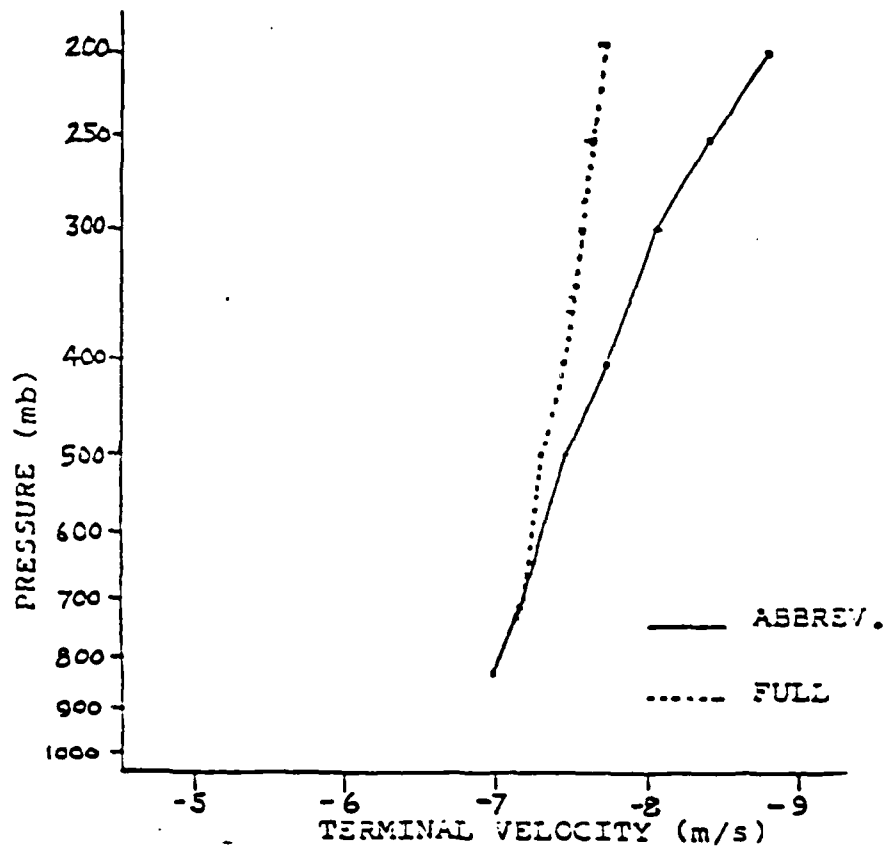


Figure 4.2 Graph of terminal velocity for both the FULL(...) and the ABBREVIATED (\_\_\_) Foote & duToit correction formula. Reflectivity is 60dBz, density is from adiabatic-hydrostatic formulation. Terminal velocity formula is from Martner(1976). Difference at 200 mb is 1.08 m/s.

from (3.4.10). While these differences are significant when related to the actual values of  $V_t$ , in light of Section 4.2.1.2, they are of little significance in the computation of the  $u$  and  $v$  components, see (3.4.11a) and (3.4.11b).

#### 4.2.2.3 Errors associated with subjective analysis

There is no exact method for measuring errors in results due to subjective editing of the data. It suffices to say that for this study wind velocities in the storm environment were modified only in cases where the data were absolutely required to perform the study.

The only data which was considered for modification were the radial winds after they had been placed on the grid and prior to deriving the three-dimensional wind fields. Among the considerations prior to modifying a given piece of data were; 1) three-dimensional continuity of the modified datum within the radial wind field, 2) effects that the modified data had on the derived wind fields, and 3) the continuity of the derived fields with and without the modifications.

#### 4.3 Errors in Derived Thermodynamic Fields

Errors in the pressure field come basically from two sources. Errors in the wind field will produce

errors in the retrieved pressure field. Pasken (1981) used model output from the Lin and Chang (1977) storm model to examine this type of error. He found that 10% error in the wind field produced approximately a 10% error in the retrieved pressure field.

The actual output from the pressure retrieval program is the perturbation pressure field. This solution is not unique. Removing the mean perturbation pressure from the solution field leaves the deviation perturbation pressure field, which is unique. If the mean perturbation pressure which is removed is in error, this will result in an error in the deviation perturbation pressure fields. Knowledge of the mean perturbation pressure is not available, however, computations of the mean and standard deviations of the resultant pressure fields were done level by level. If the area of computation of the pressure field was large enough, it was assumed that the mean of the perturbation pressure would be approximately zero (i.e.,  $\langle p' \rangle \approx 0$ , Gal-Chen, 1978). Examination of the deviation perturbation means, not shown, reveal that these values are zero. It suggests that the deviation perturbation pressure pattern is realistic and probably free of error of the second type. Lin et al. (1985) investigated the sensitivity of pressure retrieval to exclusion of the local time tendency.

They discovered that the inclusion of the local time derivative terms in the dynamic equations did not improve the accuracy of pressure recovery.

Errors in temperature retrieval depend heavily on the input wind fields as well as the retrieved pressure and density fields. The use of friction in the computations of both pressure and temperature ultimately involve the second and third derivative of the wind field. Gal-Chen and Kropfli (1984) investigated the effect of friction in the planetary boundary layer on the retrieval of pressure and potential temperature fields. They found that the inclusion of friction did not significantly reduce relative errors ( $E_r$ ) in pressure recovery and suggested that the pressure calculation seems to be relatively insensitive to which frictional parameterization scheme is used.

Using model-generated data as input, Hane et al. (1981) inserted random errors of  $\pm 0.5 \text{ m s}^{-1}$  into the wind field. Their findings indicate that retrieved perturbation virtual temperature is sensitive to errors in the wind field. They found that errors introduced in the form of "white noise", implying wavelength independence, produced an average error in the associated temperature field of about  $1.0^\circ \text{C}$ , on the average, see their Fig. 12. They further suggested that if the wavelengths at which the noise was

occurring were known, a filter could be applied to reduce noise contamination of the temperature results. After applying such a filter to the above case, they found the resultant errors in the temperature fields to be reduced to  $.5^{\circ}\text{C}$  or less, see their Fig. 13. Similar results for small wavelength noise were also obtained. Their study also investigated the effect the steady state assumption and inclusion of friction had on the resultant potential temperature fields. They found that "...when the local time derivative was eliminated altogether, the solution deteriorated considerably, but was judged to be useful if general temperature patterns are desired. Exclusion of the turbulence term resulted in significant errors, but the solution was still of value. Inability to accurately measure cloudwater mixing ratio produced errors which were less severe than those created by non-inclusion of turbulence or time derivatives."

## CHAPTER 5

### Sensitivity Tests of Thermodynamic Retrieval

A series of experiments were conducted in an effort to determine the sensitivity of the thermodynamic retrieval method. Many investigators have looked at whether the inclusion of a correction scheme which brings the continuity equation into balance after correcting the vertical velocities, aids in producing "more correct" results, e.g., Ray et al. (1980), Ziegler et al. (1983), Gal-Chen and Kropfli (1984) and Lin et al. (1985). In addition, Lin et al. (1985) and Wirsing (1985) looked at the resultant thermodynamic fields when no correction was imposed. In both these cases, downward integration was used from the storm top and the storm was considerably stronger than the storm investigated in the present study. The overwhelming conclusions from these and other investigations are that some type of correction of the 3D wind field is necessary in order to satisfy mass continuity within the domain of interest. This correction, based on the variational concept, is particularly needed if observational errors are signifi-

cant. To this end, sensitivity of the recovery technique to inclusion of a correction scheme was not tested. All results presented herein include the calculus of variation scheme (Sasaki, 1970) as the correction scheme unless otherwise noted.

In this study, we attempted to further examine the impact of random errors in the wind field on the calculation of vertical velocity, pressure and temperature fields for a non-severe convective storm. The following cases were considered:

- 1) Inclusion of two types of frictional parameterizations in the momentum equations.
- 2) Smoothing of the radial wind field by increasing the scan radius in the Barnes' objective analysis scheme.
- 3) Sensitivity of the retrieval process to randomly introduced errors in the initial wind field.
- 4) Sensitivity to changes in liquid water content.

Table 5.1 describes the identification of the cases and the elements included or excluded from each of the experiments.

Gal-Chen (1978) suggested a measure of "goodness" of the recovery technique. The momentum check mentioned in Chapter 3 provides a measure of "relative error" between the derivatives of the recovered pressure field and the momentum equations, see Eq.

Table 5.1

Description of the experiments conducted in the present study

Experiment	Case	Smoothed/ Unsmoothed	None	Friction K-W Austausch	Induced Error	Water Modified
1	VUN	Unsmoothed	Yes	No	No	No
2	VUKW	Unsmoothed	No	Yes	No	No
3	VUA	Unsmoothed	No	No	No	No
4	VSN	Smoothed	Yes	No	No	No
5	VSKW	Smoothed	No	Yes	No	No
6	VSA	Smoothed	No	No	No	No
7	VSKWE1	Smoothed	No	Yes	Yes (10%)	No
8	VSKWE2	Smoothed	No	Yes	Yes (20%)	No
9	VSKWL	Smoothed	No	Yes	No	Yes



(3.6.18). Small values of the momentum check suggest better agreement between the fields of pressure and momentum. However, this condition is only necessary but not sufficient. For this reason, it is essential to examine the physical plausibility and time continuity of the retrieved fields as well (Gal-Chen and Hane, 1981). According to Hane and Ray (1985), larger values still allow for extraction of useful information from the recovered fields. This measure was employed in this study to determine whether an included or excluded term was significant or secondary. Lin et al. (1985) used a 5% reduction of the momentum check statistic as the dividing line between significant and secondary. While this is somewhat arbitrary, their results agree well with other investigations which also tested sensitivity, e.g., Gal-Chen and Kropfli (1984) and Roux et al. (1984). The same measure is used in this study.

Two frictional parameterizations were employed along with the exclusion of friction from the computations. Results indicate that friction should be included especially when the analyzed levels extend to within 1 km of the surface. Our findings also indicate that the pressure recovery scheme is relatively insensitive to which parameterization scheme is used.

The use of a larger scan radius increases the

wavelength of a minimum resolvable wave as discussed in Appendix A. Therefore it plays a role somewhat similar to smoothing discussed in studies by Gal-Chen and Kropfli (1984), Lin et al. (1985) Wirsing (1985), etc. The studies by Wirsing (1985) and Lin et al. (1985) discovered that smoothing substantially reduced the momentum check values. Unlike an arbitrary smoothing scheme (Shuman, 1959) used in the above two studies, the scheme employed in this study allows us to explicitly know what is the minimum resolvable wavelength in the derived fields. More detailed discussions follow.

Modification of the liquid water content produced deceiving results. When viewed from the perspective of area averages, the recovery process seemed to be relatively insensitive. However, sensitivity appears to be directly related to reflectivity and can become significant where reflectivities are strong.

### 5.1 Frictional Parameterization

Two frictional parameterizations were used in this study. The first was based on the Austausch hypothesis with constant eddy viscosity coefficients, labeled A in the text. Both horizontal and vertical coefficients were set to be  $100 \text{ m}^2 \text{ s}^{-1}$ . The second approach was suggested by Klemp and Wilhelmson (1978), labeled KW in the text. The governing equa-

tions for this parameterization can be found in Section 3.6. Table 5.2 shows the momentum check ( $\epsilon_r$ ) results for the various cases. Examination of VUN versus VUKW reveals an average reduction of the momentum check values of less than 5%. However, much improvement is found when case VSN is compared to case VSKW. It appears that for unsmoothed data frictional parameterization has less effect than for smoothed data in pressure retrieval. Table 5.2 further shows that when comparing either frictional case (VSA or VSKW) with the smoothed case without friction (VSN), inclusion of friction is significant in the lower layers but not above 4.5 km. The larger momentum check value near the surface is the result of numerical problems with a one sided derivative compounded by lower boundary condition that vertical velocity vanishes at the surface. Inspection of the reflectivity pattern and the sounding reveal that the cloud base of the parent cloud was near 4.0 km AGL.

As previously stated the vertical and horizontal eddy viscosity coefficients were both set to be  $100 \text{ m}^2 \text{ s}^{-1}$ . The similarity between VSKW and VSA is evident. This would indicate that while inclusion of some friction parameterization is needed, it does not seem to matter which scheme is used. This result agrees with Hane et al. (1981). They concluded that

Table 5.2.

Momentum Check values for each case at 1647 MDT. Cases considered include unsmoothed no friction (VUN), unsmoothed with Klemp and Wilhelmson friction parameterization (VIJW), unsmoothed with Austausch friction parameterization (VUA) with  $K_m = 100 \text{ m s}$ , smoothed no friction (VSN), smoothed with Klemp and Wilhelmson friction parameterization (VSKW), and smoothed with Austausch friction parameterization (VSA) with  $K_m = 100 \text{ m s}$ . The domain being considered is 10 km by 10 km centered on the microburst and containing the entire storm. Unsmoothed data were computed with a scan radius of 1.25 km, while smoothed data were computed with a scan radius of 1.75 km. VSKWE1 and VSKWE2 cases include 10 and 20% random errors, respectively, in the measured radial wind fields.

Table 5.2

Z(km)	(VUN)	(VUKW)	(VUA)	(VSN)	(VSKW)	(VSA)	(VSKWE1)	(VSKWE2)
0.25	.284	.274	.315	.224	.202	.204	.204	.203
0.50	.230	.225	.223	.165	.152	.153	.154	.151
0.75	.264	.261	.279	.187	.176	.173	.175	.178
1.0	.360	.369	.360	.313	.300	.297	.301	.297
1.5	.501	.499	.503	.494	.472	.469	.474	.475
2.0	.531	.516	.527	.529	.492	.495	.494	.491
2.5	.492	.462	.483	.476	.404	.405	.407	.402
3.0	.557	.524	.568	.559	.505	.499	.504	.495
3.5	.540	.508	.546	.510	.494	.494	.494	.478
4.0	.529	.512	.527	.471	.439	.437	.439	.437
4.5	.552	.530	.555	.499	.448	.445	.451	.416
5.0	.603	.598	.604	.556	.527	.527	.524	.508
5.5	.633	.636	.637	.556	.554	.550	.550	.533
6.0	.645	.645	.644	.595	.593	.590	.591	.588
6.5	.720	.717	.719	.688	.679	.678	.675	.658
7.0	.762	.756	.760	.750	.739	.737	.728	.731
7.5	.710	.703	.712	.703	.690	.686	.670	.673
8.0	.646	.634	.646	.611	.584	.581	.573	.588
8.5	.620	.628	.627	.630	.609	.605	.508	.563

exclusion of the frictional parameterization would degrade results but that the solution should be of value. These results, however, do not agree with other investigations, e.g., Gal-Chen and Kropfli (1984) or Lin et al. (1985). The study by Lin et al. (1985) found that friction did not contribute significantly to thermodynamic retrievals at any level inside the severe storm embedded within a squall line system.. The lowest level analyzed in that study was 1.5 km AGL and it appeared to be above the base of the parent cloud. This would tend to suggest that frictional contributions may be most important in the area below the cloud and within first 1 or 2 km of the surface. On the other hand, Gal-Chen and Kropfli (1984) studied the dynamics of the planetary boundary layer for a clear sky. They found no significant reduction in the relative errors ( $\bar{Er}$ ) for the retrieval of pressure and temperature perturbations when the subgrid scale turbulence parameterization was included in the dynamic equations.

Unlike the above two studies, the present study is focused on the structure of a nonsevere convective storm in Colorado. This type of storm usually has a deep subcloud layer up to 4 km AGL. During the occurrence of a microburst in the lower troposphere, strong 3D wind shears develop causing severe turbulence. As

a result, a contribution due to convergence/divergence of momentum transfer by eddies to the momentum change becomes significant. This is evident in the  $Er$  values presented in Table 5.2. Note that at most levels the Austausch formulation produces slightly better results than the Klemp and Wilhelmson (1978) scheme. The standard deviations of pressure ( $SDp'$ ) are higher, especially above 2 km, when the Klemp and Wilhelmson (1978) scheme is used, while the standard deviations of temperature ( $SDT'$ ) are higher when the Austausch formulation is used, see Tables 5.3a and 5.3b. It appears that while the contributions from friction to retrieved pressure may be inversely proportional to  $\tau$ , contributions to temperature appear to be proportional to  $\tau$ .

In order to learn more about the effect of friction on the dynamics of a microburst-producing nonsevere storm, spatial variation of eddy viscosity coefficients ( $K_m$ ) and Reynolds stresses ( $\tau$ ) using the frictional parameterization of Klemp and Wilhelmson (1978) were investigated. Results are presented in Figs. 5.1 through 5.5 and Table 5.4.

Table 5.4a shows the means and standard deviations of Reynolds stresses ( $\tau$ ) created using the Klemp and Wilhelmson (1978) scheme. Table 5.4b shows similar components of Reynolds stresses ( $\tau$ ) from the

Table 5.3a

Values of the standard deviation (SD) for the two retrieved thermodynamic variables at a given level for 1647 MDT. Cases considered include unsmoothed no friction (VUN), Klemp and Wilhelmson frictional parameterization (VUKW), and Austausch frictional parameterization (VUA) with  $K_m = 100 \text{ m}^2 \text{ s}^{-1}$ . The domain being considered is 10 km by 10 km centered on the microburst and containing the entire storm. Units are in Pascals (Pa) and  $^{\circ}\text{C}$  for pressure and temperature, respectively.

Z(km)	(VUN)		(VUKW)		(VUA)	
	SDp' Pa	SDT' $^{\circ}\text{C}$	SDp' Pa	SDT' $^{\circ}\text{C}$	SDp' Pa	SDT' $^{\circ}\text{C}$
0.25	5.41	.75	6.26	.80	5.83	.71
0.50	6.64	.97	7.22	1.04	6.76	.96
0.75	8.28	.89	9.08	.94	8.60	.87
1.0	6.38	.68	7.28	.74	7.03	.62
1.5	5.77	.67	7.59	.67	6.51	.52
2.0	4.21	.68	5.06	.70	4.92	.53
2.5	4.25	.68	5.40	.70	5.97	.56
3.0	4.22	.68	5.73	.70	6.92	.63
3.5	5.43	.74	6.98	.76	9.70	.59
4.0	5.52	.86	6.57	.90	7.28	.73
4.5	5.95	1.02	7.23	1.05	7.51	.77
5.0	7.25	1.23	9.62	1.25	9.67	.89
5.5	7.18	1.37	8.67	1.39	8.45	.98
6.0	6.92	1.33	8.13	1.36	8.11	.97
6.5	5.14	1.17	6.73	1.18	6.53	.86
7.0	3.39	.92	4.36	.93	3.88	.69
7.5	3.08	.61	3.75	.63	3.28	.52
8.0	3.11	.41	3.74	.42	3.58	.34
8.5	2.23	.33	2.83	.35	1.93	.38



Table 5.3b

As in Table 5.3a except for smoothed cases.

Z(k	VSN		VSKW		VSA	
	SDp' Pa	SDT' °C	SDp' Pa	SDT' °C	SDp' Pa	SDT' °C
0.25	4.74	.65	5.79	.70	5.74	.71
0.50	5.81	.85	6.65	.94	6.78	.89
0.75	7.49	.75	8.51	.85	8.21	.86
1.0	5.61	.54	6.99	.62	6.59	.69
1.5	4.45	.51	6.44	.52	5.81	.67
2.0	3.54	.51	4.92	.53	3.99	.69
2.5	3.65	.52	6.03	.56	4.40	.69
3.0	4.31	.56	6.89	.63	3.82	.69
3.5	4.38	.54	9.53	.59	5.16	.75
4.0	5.24	.65	7.27	.72	5.54	.87
4.5	5.53	.70	7.40	.77	5.89	1.03
5.0	5.80	.85	9.73	.89	7.42	1.23
5.5	6.14	.95	8.56	.98	7.31	1.37
6.0	6.08	.93	8.16	.97	7.11	1.33
6.5	4.39	.83	6.64	.86	5.19	1.17
7.0	2.88	.66	3.93	.69	3.46	.92
7.5	2.60	.48	3.28	.52	3.07	.61
8.0	2.58	.31	3.54	.33	3.09	.40
8.5	1.44	.28	1.87	.38	2.09	.34

Table 5.4a

Values of the mean and standard deviation (SD) for horizontal Reynolds stresses;  $\tau_{xx}$ ,  $\tau_{xy}$  and  $\tau_{yy}$  and vertical Reynolds stresses;  $\tau_{xz}$ ,  $\tau_{yz}$ , and  $\tau_{zz}$ , computed from case VSKW with the Klemp and Wilhelmson frictional formulation at a given level for 1647 MDT.

Z(km)	Horizontal					
	$\tau_{xx}$		$\tau_{xy}$		$\tau_{yy}$	
	mean N/m <sup>2</sup>	SD N/m <sup>2</sup>	mean N/m <sup>2</sup>	SD N/m <sup>2</sup>	mean N/m <sup>2</sup>	SD N/m <sup>2</sup>
0.25	-.018	.106	-.001	.042	-.024	.152
0.50	-.015	.094	-.006	.041	-.017	.099
0.75	-.007	.048	-.006	.027	-.019	.070
1.0	-.007	.038	-.006	.032	-.040	.132
1.5	-.024	.078	-.004	.053	-.038	.115
2.0	-.033	.107	-.004	.059	-.029	.104
2.5	-.042	.112	-.011	.056	-.039	.139
3.0	-.054	.124	-.013	.042	-.061	.187
3.5	-.067	.139	-.010	.061	-.045	.147
4.0	-.083	.150	-.009	.054	-.040	.122
4.5	-.082	.157	-.008	.047	-.035	.135
5.0	-.056	.134	-.001	.042	-.026	.081
5.5	-.039	.124	.006	.048	-.037	.173
6.0	-.032	.118	.008	.067	-.033	.175
6.5	-.026	.094	.006	.060	-.022	.107
7.0	-.020	.099	.005	.065	-.008	.066
7.5	-.008	.077	.003	.053	-.003	.051
8.0	-.006	.071	-.002	.042	-.004	.050
8.5	-.006	.067	-.002	.029	-.010	.062

Table 5.4a  
continued

Vertical

Z(km)	$\tau_{xz}$		$\tau_{yz}$		$\tau_{zz}$	
	mean N/m <sup>2</sup>	SD N/m <sup>2</sup>	mean N/m <sup>2</sup>	SD N/m <sup>2</sup>	mean N/m <sup>2</sup>	SD N/m <sup>2</sup>
0.25	-.006	.055	-.009	.128	-.151	.477
0.50	-.000	.039	-.047	.142	-.121	.369
0.75	-.002	.068	-.096	.191	-.065	.191
1.0	-.004	.084	-.062	.116	-.034	.111
1.5	-.004	.123	-.010	.106	-.027	.125
2.0	.003	.104	.026	.110	-.013	.081
2.5	.020	.112	.023	.121	-.007	.075
3.0	.043	.135	.005	.121	-.000	.072
3.5	.037	.118	-.043	.149	.003	.068
4.0	.018	.112	-.096	.166	.014	.060
4.5	.014	.101	-.114	.190	.009	.075
5.0	.016	.105	-.084	.175	-.007	.090
5.5	.011	.112	-.035	.151	-.024	.095
6.0	.002	.104	.006	.144	-.029	.105
6.5	.003	.105	.026	.123	-.026	.069
7.0	.002	.068	.040	.098	-.039	.091
7.5	.013	.047	.039	.068	-.050	.091
8.0	-.032	.047	.022	.038	-.062	.107
8.5	-.046	.072	.025	.053	-.071	.138

Table 5.4b

As in Table 5.4a but for case VSA with constant eddy viscosity coefficient ( $K_m = 100 \text{ m}^2 \text{ s}^{-1}$ ).

Horizontal						
Z(km)	$\tau_{xx}$		$\tau_{xy}$		$\tau_{yy}$	
	mean N/m <sup>2</sup>	SD N/m <sup>2</sup>	mean N/m <sup>2</sup>	SD N/m <sup>2</sup>	mean N/m <sup>2</sup>	SD N/m <sup>2</sup>
0.25	.002	.162	-.019	.189	.026	.180
0.50	.007	.153	-.010	.148	.014	.162
0.75	.014	.105	-.011	.109	-.001	.140
1.0	.007	.079	-.028	.155	-.014	.146
1.5	-.006	.101	-.029	.119	-.020	.108
2.0	-.016	.113	-.023	.118	-.018	.095
2.5	-.021	.109	-.004	.110	-.016	.109
3.0	-.029	.110	.003	.122	-.014	.133
3.5	-.036	.116	.006	.112	-.012	.117
4.0	-.052	.109	-.010	.095	-.010	.099
4.5	-.047	.114	-.002	.091	-.004	.108
5.0	-.026	.110	.004	.090	-.002	.093
5.5	-.005	.102	-.007	.110	.003	.100
6.0	-.001	.101	-.005	.125	.008	.106
6.5	.001	.094	-.009	.111	.008	.095
7.0	.010	.092	-.004	.090	.014	.087
7.5	.020	.088	.003	.097	.019	.074
8.0	.023	.080	-.005	.074	.017	.071
8.5	.020	.074	.005	.078	.013	.075

Table 5.4b  
continued

Vertical						
Z(km)	$\tau_{xz}$		$\tau_{yz}$		$\tau_{zz}$	
	mean N/m <sup>2</sup>	SD N/m <sup>2</sup>	mean N/m <sup>2</sup>	SD N/m <sup>2</sup>	mean N/m <sup>2</sup>	SD N/m <sup>2</sup>
0.25	-.002	.210	.004	.197	-.037	.259
0.50	-.005	.150	.002	.125	-.034	.234
0.75	-.007	.115	-.010	.091	-.023	.187
1.0	-.026	.148	-.027	.133	-.003	.142
1.5	-.034	.112	-.029	.122	.011	.127
2.0	-.018	.113	-.020	.113	.022	.111
2.5	-.003	.108	.010	.111	.028	.104
3.0	.003	.123	.001	.129	.034	.110
3.5	.003	.108	-.002	.115	.044	.102
4.0	-.008	.104	-.005	.094	.052	.093
4.5	-.003	.090	-.007	.089	.047	.100
5.0	.002	.084	-.004	.081	.027	.104
5.5	-.006	.111	-.024	.111	.008	.103
6.0	-.011	.114	-.026	.112	-.004	.095
6.5	-.010	.105	-.008	.099	-.011	.080
7.0	.001	.080	.004	.088	-.024	.074
7.5	.000	.071	.004	.066	-.037	.069
8.0	-.004	.078	-.001	.068	-.041	.075
8.5	.001	.078	.002	.073	-.039	.084

Austausch scheme. Figures 5.1 and 5.2 show the mean of layer averages of horizontal Reynolds stresses for case VSKW and case VSA, respectively. A comparison of these components reveals that while they are similar in appearance, for the Austausch formulation, the means of the  $\tau$  values are more positive and tend to be slightly smaller than those generated by the Klemp and Wilhelmson (1978) formulation. Figure 5.3 depicts the reason for this phenomenon.

Figure 5.3 shows the computed  $\tau_{xx}$  for various values of  $\Delta U/\Delta X$ . The horizontal axis represents the value  $\Delta U$  and assumes  $\Delta X = 500$  m. For a span of  $\Delta U$  from -10 to +10 representing  $\Delta U/\Delta X$  of -.02 to +.02., the values produced by the Austausch formulation are seen to be smaller than those from the Klemp and Wilhelmson formulation. When the Klemp and Wilhelmson parameterization is used to compute the Reynolds stress, the values are asymmetrical about 0. That is, a negative value of  $\Delta U/\Delta X$  produces larger (in the absolute sense) values of  $\tau$  than the corresponding positive value of  $\Delta U/\Delta X$ . This accounts for the negative shift of the Reynold Stress values when the Klemp and Wilhelmson parameterization is used. Similar results, not shown, occur for the vertical Reynolds stress components. Note that the computations of the means are for the values of  $\tau$  and not for the

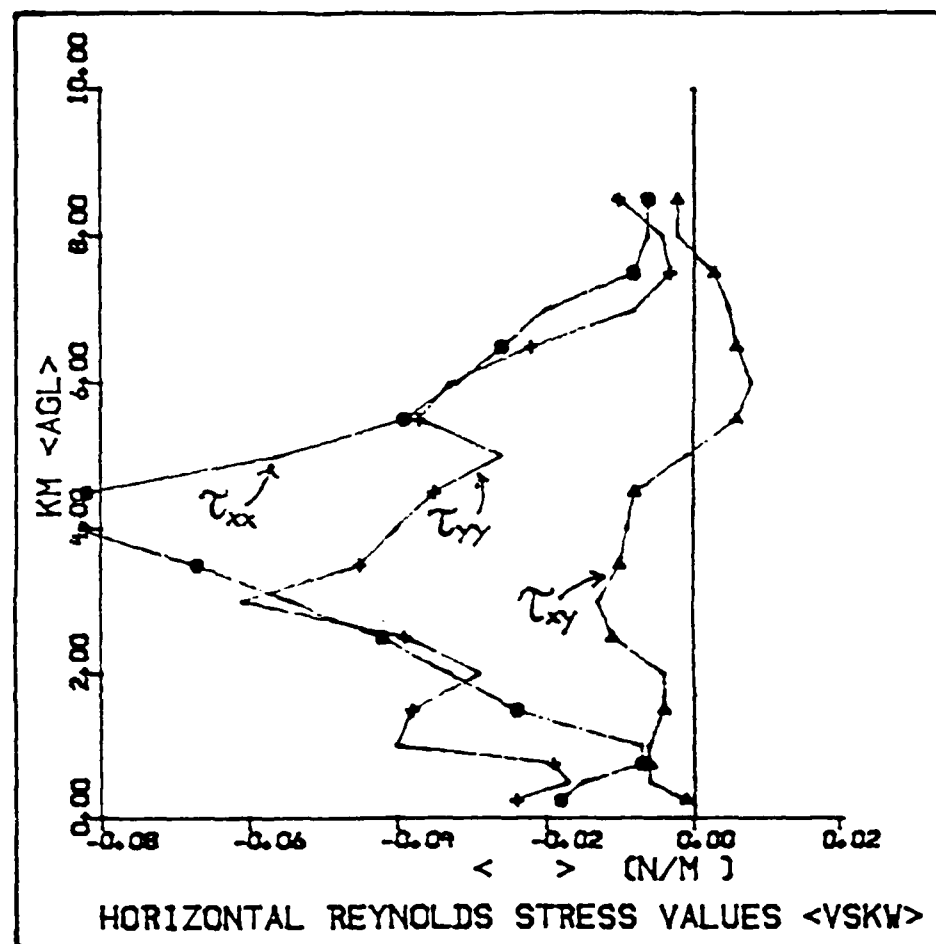


Fig. 5.1 Horizontal Reynolds stresses  $\tau_{xx}$ ,  $\tau_{xy}$  and  $\tau_{yy}$  for case VSKW. Units are Newtons per square meter ( $\text{N/m}^2$ )

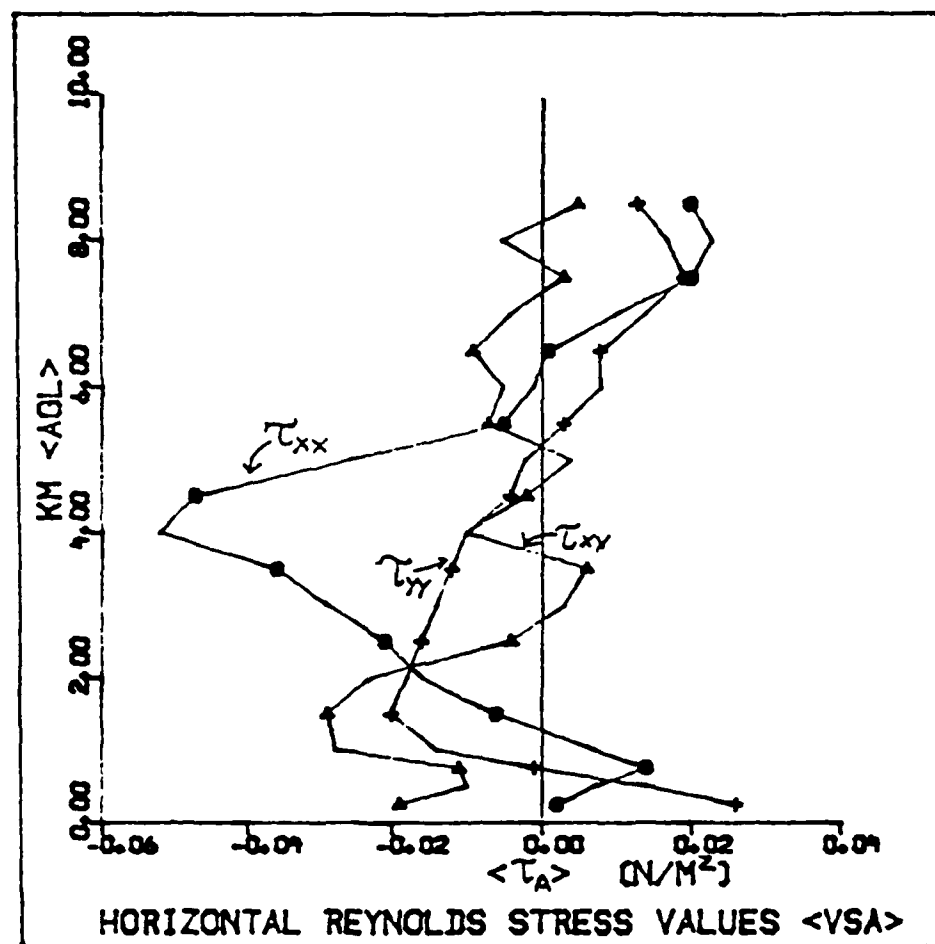


Fig. 5.2 As in Fig. 5.1 except for case VSA.



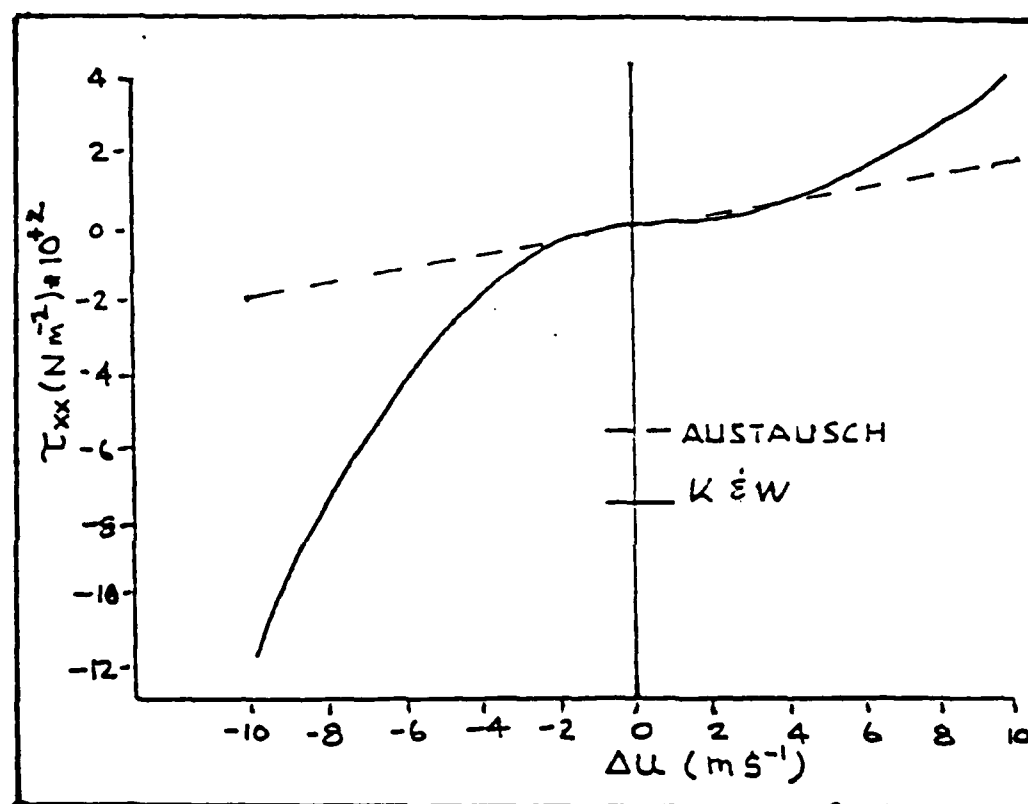


Fig. 5.3 Range of  $\tau_{xx}$  for given  $U$ -component differences for Klemp and Wilhelmson frictional parameterization and Austausch frictional parameterization.

absolute value of  $\tau$ . Since these means are so close to zero, the standard deviations are very close to the means of the absolute values of  $\tau$ . Actual values of  $\tau$  in the vicinity of the microburst center, not shown, ranged in value from .3 to -.3 for the VSKW case.

Figures 5.4 and 5.5 show the mean horizontal ( $K_{mxx}$ ,  $K_{mxy}$  and  $K_{myy}$ ) and vertical ( $K_{mxz}$ ,  $K_{myz}$  and  $K_{mzz}$ ) eddy viscosity coefficients, respectively, for case VSKW. The larger values of  $K_{myz}$  found in the mid-troposphere are related to the v component jet which was previously identified. These findings suggest that:

- 1) When compared to the frictional formulation based on the Austausch hypothesis, the Klemp and Wilhelmson formulation produces lower estimates of the frictional contribution in the pressure retrieval process by underestimating the eddy viscosity coefficient.
- 2) When compared to the Austausch formula, Klemp and Wilhelmson frictional scheme tends to smooth the recovered temperature and intensify pressure deviations.

## 5.2 Smoothing of Radial Winds

Smoothing in this study was accomplished by increasing the scan radius in the Barnes gridding procedure from 1.25 to 1.75 km. Prior to the gridding

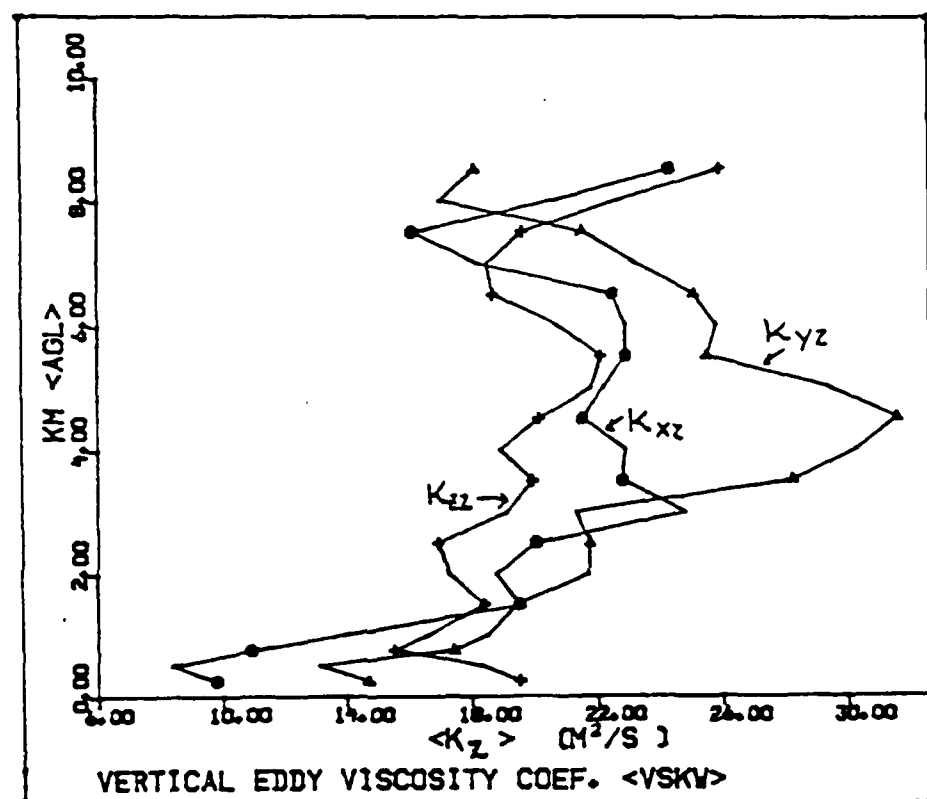


Fig. 5.4 Vertical eddy viscosity coefficients computed from basic case (VSKW) horizontal winds using formula of Smagorinsky (1963). Units are  $m^2 s^{-1}$ .

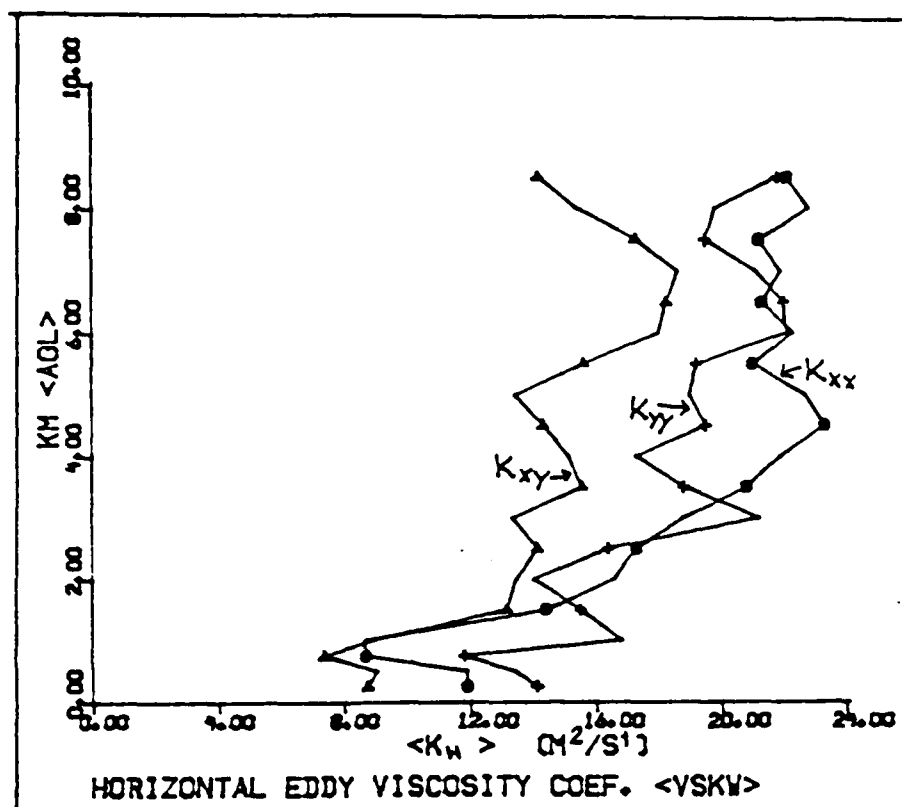


Fig. 5.5 As in Fig. 5.4 except for horizontal eddy viscosity coefficients.

process, the data were sliced into slabs which, except for the levels below 1.0 km, were mutually exclusive, that is data from one layer were not used in the gridding process of another layer. Thus increasing the scan radius essentially resulted in a horizontal smoothing rather than a full three dimensional smoothing process. Table 5.2 shows the results of the momentum check values for the unsmoothed no friction case (VUN) and the smoothed no friction case (VSN). Note that the percentage decreases in  $E_r$  are particularly significant in the layer from the surface to 4 km. This is approximately the height of the parent cloud base. Table 5.5 shows the means and standard deviations of the three-dimensional wind components. As expected the means and standard deviations for the smoothed case (VSN) are less than for the unsmoothed case (VUN). Notice that the apparent wind maximum in the  $v$  component occurs in the layers between 4 to 6 km. Due to the mutual exclusivity of data used in the level gridding procedure, existence of this feature in the vertical indicates that this is an actual feature rather than contamination of a number of grid points in the horizontal by an error at a single data point.

As noted earlier, Table 5.3 shows the standard deviations for the pressure and temperature variables

Table 5.5

Values of the mean and standard deviation (SD) for the three velocity components for 1647 MDT. Cases considered include VUN (variational-unsmoothed without friction) and VSN (variational-smoothed with friction). Scan radii are 1.25 and 1.75 km for unsmoothed and smoothed cases, respectively. The domain is 10 km by 10 km centered on the microburst.

Z(km)	Unsmoothed						Smoothed					
	u m/s	v m/s	w m/s	SDu m/s	SDv m/s	SDw m/s	u m/s	v m/s	w m/s	SDu m/s	SDv m/s	SDw m/s
0.25	1.7	-1.2	-.1	1.8	2.5	0.9	1.7	-1.2	-.1	1.7	2.4	0.8
0.50	1.6	-1.2	-.2	1.9	2.5	1.6	1.6	-1.2	-.2	1.8	2.4	1.4
0.75	1.6	-1.8	-.3	1.4	2.4	2.2	1.6	-1.8	-.3	1.3	2.3	2.0
1.0	1.5	-2.6	-.3	1.1	2.4	2.6	1.5	-2.6	-.3	1.0	2.3	2.3
1.5	1.3	-3.2	-.3	1.7	1.8	3.1	1.4	-3.3	-.3	1.5	1.7	2.8
2.0	1.3	-2.9	-.2	2.3	1.7	3.5	1.3	-2.9	-.2	2.1	1.6	3.1
2.5	1.4	-2.5	-.1	2.4	1.9	3.6	1.4	-2.5	-.1	2.2	1.8	3.2
3.0	1.7	-2.1	.1	2.5	2.2	3.6	1.8	-2.2	.1	2.4	2.2	3.1
3.5	2.5	-2.4	.4	3.0	2.1	3.5	2.6	-2.5	.4	3.0	1.9	2.9
4.0	2.9	-3.6	.8	3.1	2.3	3.5	2.9	-3.6	.8	2.9	2.2	2.8
4.5	3.0	-5.3	1.2	3.1	2.2	3.5	3.0	-5.3	1.2	3.0	2.0	2.8
5.0	3.3	-6.9	1.5	2.6	2.0	3.5	3.3	-6.9	1.5	2.5	1.8	2.8
5.5	3.4	-7.8	1.6	2.2	2.0	3.6	3.4	-7.8	1.6	2.0	1.9	2.8
6.0	3.7	-7.9	1.6	2.3	2.2	3.5	3.7	-8.0	1.6	2.0	2.0	2.7
6.5	3.6	-7.3	1.6	2.3	2.2	3.3	3.6	-7.3	1.6	2.1	2.0	2.6
7.0	3.7	-6.7	1.4	2.8	2.2	2.8	3.7	-6.7	1.4	2.6	2.1	2.3
7.5	3.8	-5.5	1.1	3.0	2.3	2.3	3.8	-5.5	1.1	2.8	2.1	2.0
8.0	2.9	-4.5	.6	2.8	2.5	1.5	3.0	-4.5	.6	2.7	2.4	1.3
8.5	1.5	-3.7	.2	2.4	2.4	0.4	1.6	-3.7	.2	2.3	2.4	0.4

retrieved. Results show that smoothing (VSN) reduces the standard deviations when compared to the unsmoothed case (VUN). This is to be expected since to a great extent these retrieved variables depend on the wind. Further, in both smoothed and unsmoothed results there appears to be a maximum located within the jet level. Examination of the individual terms in the momentum equations reveals that most of the variability comes from the  $\partial v / \partial z$  term.

### 5.3 Inclusion of Random Error

The actual amount of errors in the measured wind field comes from several sources, see Chapter 4 for details. However, it has been estimated that these errors are on the order of 10% of the measured wind, e.g., Waldteufel (1976), Doviak and Zrnic (1984), etc. Since no independent measurements were made of this storm, it is impossible to determine actual errors present in the derived winds or retrieved variables. It is, however, possible to determine sensitivity of the random error inherent in the wind field to the retrieval of pressure and temperature perturbations. We have chosen the case VSKW to conduct the sensitivity experiment. Two tests were performed. In each test random error amounting to a maximum of 10% (VSKWE1) or 20% (VSKWE2) of the gridded radial wind for each radar was inserted into the wind field.

The data were then processed in a manner similar to case VSKW discussed previously.

Figures 5.6 and 5.7 show the retrieved perturbation pressure and temperature fields, respectively, at 0.25 km for case VSKWE1. The pressure and temperature patterns for case VSKWE1 (Figs. 5.6 and 5.7) are quite similar to those for the base case VSKW (Figs. 6.14 and 6.19). This indicates that the contaminated wind field did not greatly distort the retrieved pressure and temperature fields. Some useful information still can be extracted from the retrieved fields. This finding is encouraging since it demonstrates that thermodynamic retrieval is not quite sensitive to a typical error of up to 10% in the derived wind field. For this reason, we believe that the retrieved fields of deviation perturbation pressure and temperature are quite reliable. Table 5.6 shows the root mean square errors (RMSEs) and the standard deviations of the differences between the derived pressure and derived temperature fields which are free of induced error (VSKW) and those with induced error (VSKWE1) and (VSKWE2). Notice that magnitudes of RMSE for the test with 10% error (case VSKWE1) are relatively small in comparison with those of 20% error (case VSKWE2). This result indicates that the thermodynamic retrieval technique is viable if the derived wind field is



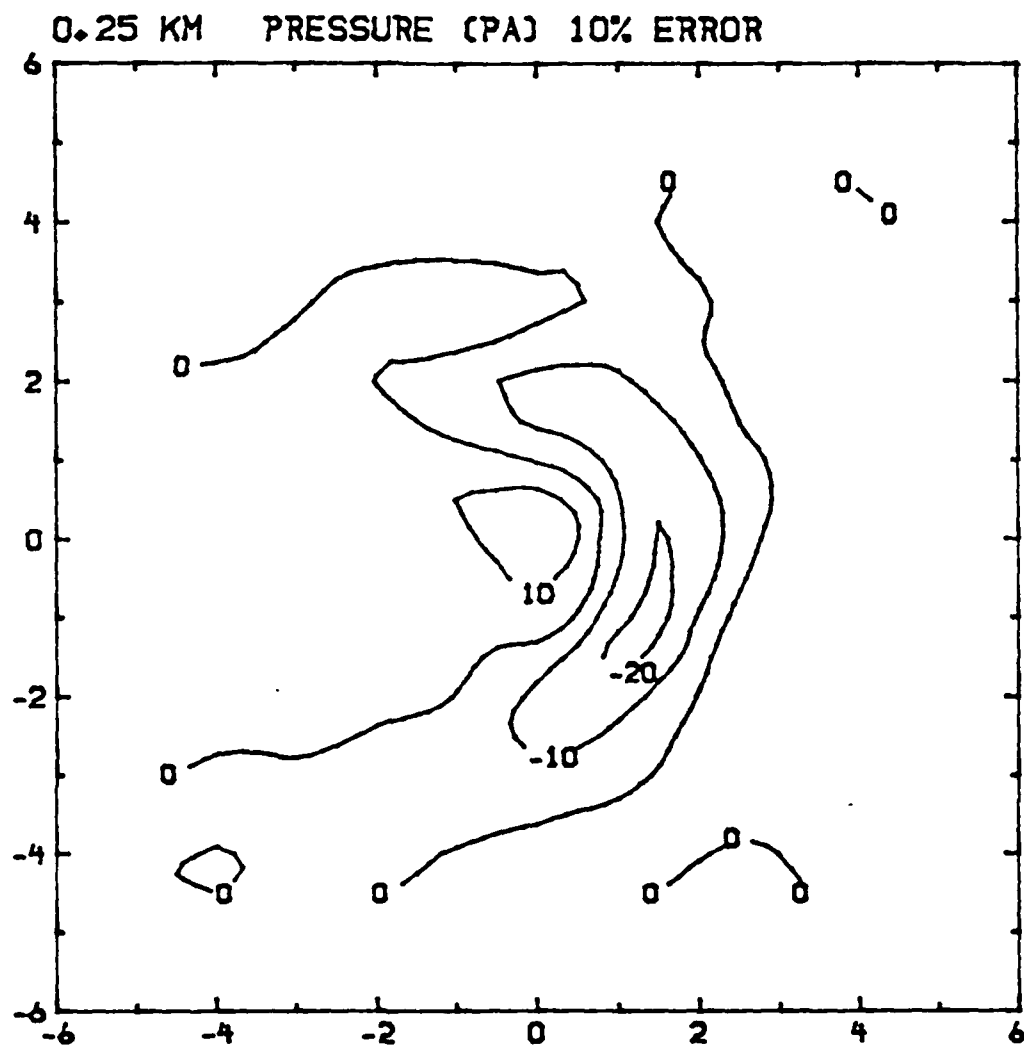


Fig. 5.6 Distribution of deviation perturbation pressure ( $P_a'$ ) at 0.25 km computed using winds with a randomly introduced 10% error in magnitude.

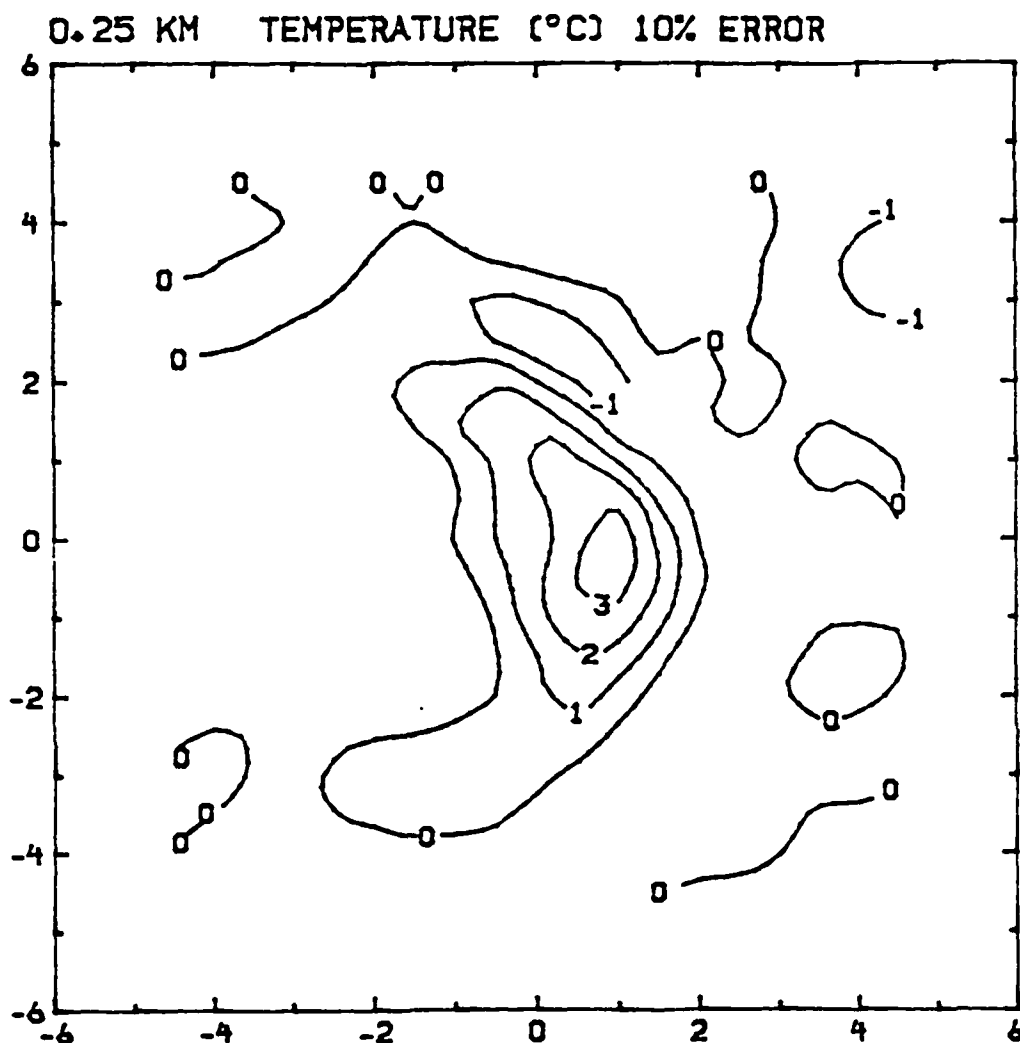


Fig. 5.7 As in Fig. 5.6 except for deviation perturbation virtual temperature ( $T_{vd}'$ ).

Table 5.6

Values of root mean square error (RMSE) between basic case, VSKW, and various sensitivity test cases, VSKWE1, VSKWE2, and VSKWEL.

Z(km)	VSKW vs. VSKWE1		VSKW vs. VSKWE2		VSKW vs. VSKWEL
	RMSE Pa	RMSE C	RMSE Pa	RMSE C	RMSE C
0.25	.101	.01	.533	.07	.07
0.50	.111	.02	.521	.05	.10
0.75	.173	.01	.411	.16	.09
1.0	.092	.02	1.857	.05	.10
1.5	.122	.02	.838	.08	.12
2.0	.115	.02	.462	.06	.09
2.5	.245	.02	.527	.06	.05
3.0	.153	.03	.933	.10	.04
3.5	.306	.03	2.044	.12	.05
4.0	.163	.05	1.673	.28	.05
4.5	.165	.07	4.737	.13	.05
5.0	.217	.09	1.205	.28	.05
5.5	.223	.11	1.220	.20	.05
6.0	.192	.12	1.755	.25	.05
6.5	.284	.12	2.702	.23	.04
7.0	.242	.12	.614	.25	.02
7.5	.197	.11	.431	.18	.02
8.0	.209	.11	.495	.19	.01
8.5	.444	.07	.987	.14	.01

within 10 to 15% accuracy of the "true" wind field.

The sensitivity of the retrieval process can be measured by comparing the standard deviations of the perturbation pressure and temperature from case VSKW, presented in Table 5.3b, to the root mean square errors shown in Table 5.6. Results show that errors created in the retrieved pressure and temperature fields are of the same order of magnitude as the induced errors, i.e., for the 10% induced error case, there appears to be about 10% differences in the retrieved field. This case represents the magnitude of the error expected in the wind field synthesized from Doppler data. For case VSKWE2, a 20% induced error seems to produce errors of about 20% to 40%. Note that inherent in this comparison is the fact that the "base" pressure and temperature fields are not absolutely free of error themselves. Errors exist in the "base" wind field used to produce the results of case VSKW. Thus any suggestion that there is a linear relationship between the magnitude of errors in the derived wind field and the retrieved thermodynamic fields should be thought of as relative only and not absolute. These results are similar to those reported by Pasken (1981) where similar comparisons were made using model data. Pasken (1981) concluded that there seems to be a direct relationship between the amount

of inserted error and the resultant error on the retrieved fields.

#### 5.4 Sensitivity to Liquid Water Loading

Sensitivity to liquid water content changes were investigated by Hane et al. (1981). They concluded that doubling the liquid water content did not contribute significantly to degradation of the retrieved variables. A similar test was performed in this study. The procedure was to double the liquid water content (VSKWEL) in the precipitation drag computation in the temperature retrieval process. Since this process did not affect the pressure computation, comparison of the momentum checks cannot be made since both (VSKW) and (VSKWEL) used the same derived pressure fields.

Column 5 in Table 5.6 shows the RMSE values of temperature retrieval between cases VSKWEL and VSKW. When these values are compared with the standard deviations of temperature for case VSKW, the RMSE values are much smaller in magnitude. It is apparent that this scheme is somewhat insensitive to changes in the liquid water content. Figure 5.3 shows the temperature differences,  $T - T_e$ , for 0.5 km level. Results show that errors in liquid water content tend to be related to the reflectivity pattern. Although

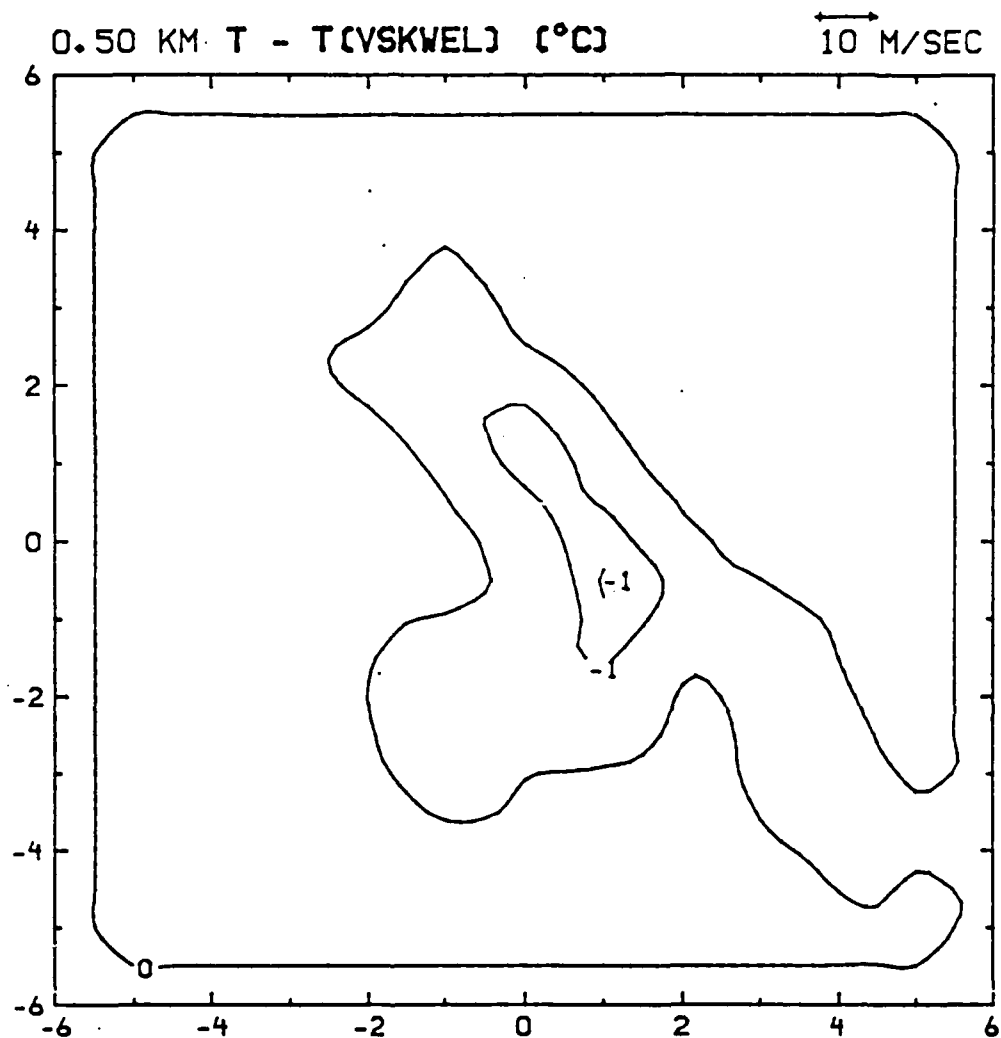


Fig. 5.8 Distribution of difference at 0.50 km between temperature computed with base case (VSKW) winds and temperature computed using winds with 10% induced error (VSKWEL).

the overall average changes indicate small changes, Fig. 5.3 shows that the errors can be very significant in areas with high reflectivity. In addition, the same test was performed with the precipitation drag term removed from the computation (not shown). The results were comparable to those when the liquid water content was doubled. The inclusion of the precipitation drag term in the computation of deviation perturbation (virtual) temperature seems to be warranted by these results. This would be especially true if the microburst being investigated were wet, where precipitation drag term plays an important role in the temperature computation.

### 5.5 "Best" Retrieval Method

From the results presented in Tables 5.2 through 5.6, Figs. 5.1 through 5.8, and using the momentum check as a measure of goodness, the smoothed case including friction (VSA or VSKW) produces the better results. Since the Klemp and Wilhelmson (1978) formulation appears to be physically more acceptable, the results of this case will be discussed in Chapter 6.

## CHAPTER 6

### Discussion of Results

In this study ten experiments were conducted to ascertain the sensitivity of the retrieval process to various modifications of a basic process, see Table 5.1. Findings show the following:

- 1) Correction of the horizontal wind to balance the anelastic continuity equation is needed.
- 2) Smoothing in the form of increased scan radius used during the Barnes' gridding process produces better results.
- 3) Inclusion of a frictional parameterization decreases momentum check values.
- 4) Inclusion of a precipitation drag term improves results.

All of these processes were incorporated into case VSKW and the results are discussed below.

#### 6.1 Three-dimensional Flow Pattern

##### 6.1.1 Horizontal velocity

Figures 6.1 and 6.2 show the pattern of  $u$  and  $v$  velocity components, respectively, at 0.25 km for 1647 MDT. For comparison, storm relative wind vectors are also plotted. All heights are above ground level



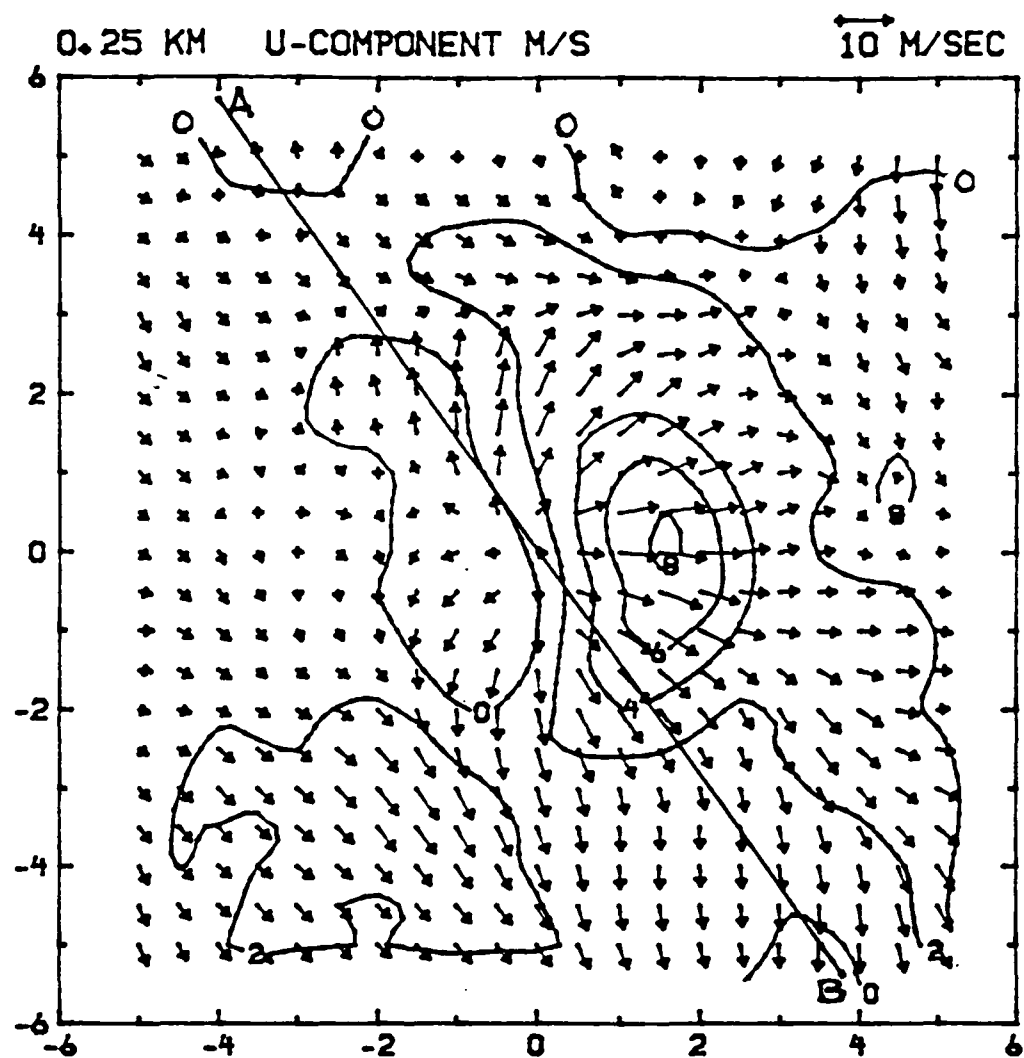


Fig. 6.1 Distribution of U-component of wind superimposed on storm-relative horizontal winds at 0.25 km. Line AB signifies the line of vertical cross sections presented elsewhere. Isotachs are at intervals of  $2 \text{ m s}^{-1}$ .

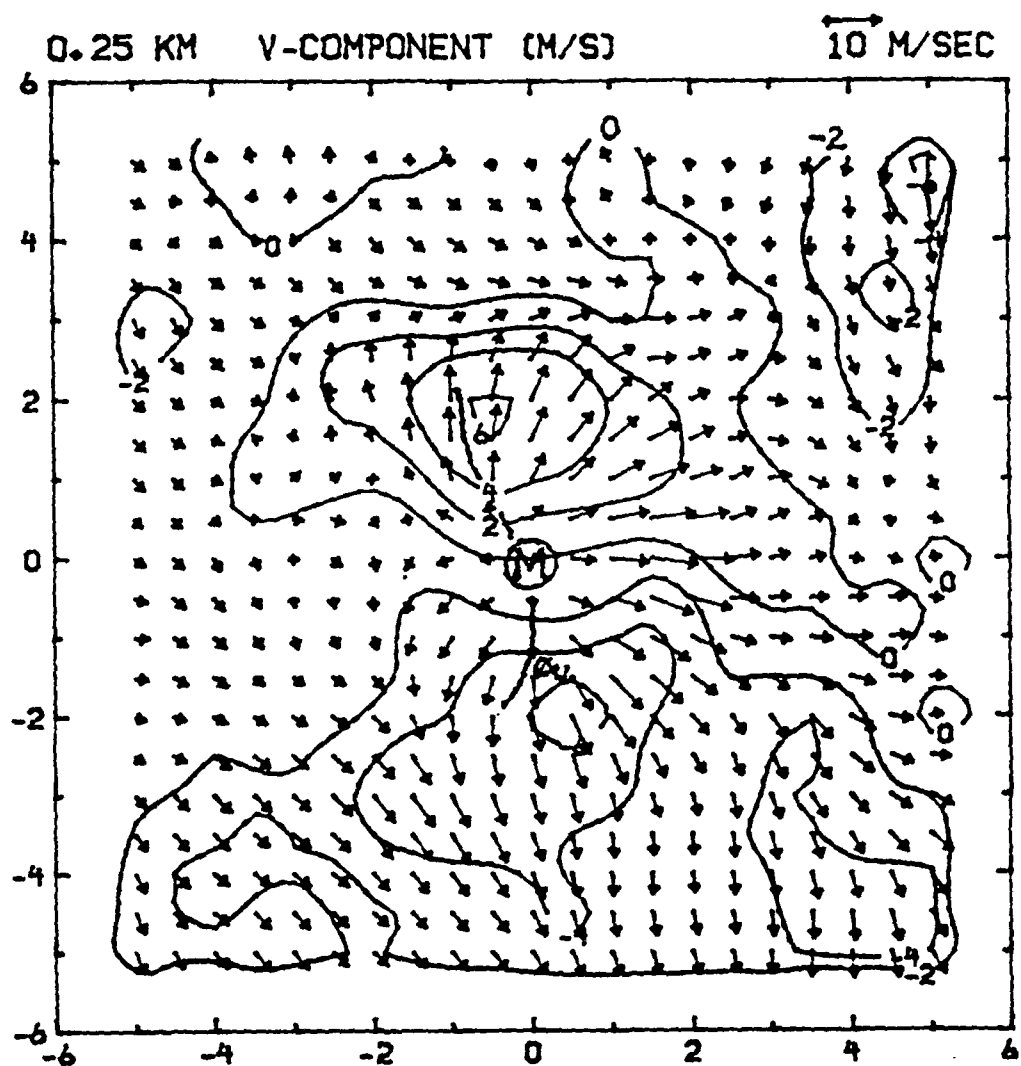


Fig. 6.2 As in Fig. 6.1 except for V-component. Dashed line denotes 0 isotachs for U-component of wind. M denotes the center of the microburst.

(AGL). Grid distances are in km with the origin located on the microburst. The center of the microburst not shown in the figures is located at 12.5 km west and 18.5 km south of the CP-2 radar (see Fig. 3.4). Line AB in Fig. 6.1 denotes the location of vertical cross section presented later. This vertical cross section is in line with the environmental flow vector. Contours for Figs. 6.1 and 6.2 are every  $2 \text{ m s}^{-1}$ . The center of the microburst can be located by superimposing the zero contour from Fig. 6.1 onto Fig. 6.2 (dashed line). The intersection of the two zero lines represents the center of the microburst at 0.25 km. Note that the absolute wind difference in the u component across the microburst is about  $10 \text{ m s}^{-1}$  and slightly larger than that for the v component. The criterion for a downburst to be a microburst is met by both components of the horizontal wind, see Fujita (1978) and McCarthy *et al.* (1983).

The shallow extent of the horizontal wind shear can be seen by comparing Fig. 6.1 at 0.25 km to Fig. 6.3 representing the same diagram but for 1.0 km AGL. At 1.0 km the u component of wind is negative (southerly) across the entire grid. Absence of the outflow feature especially in the u component of horizontal wind suggests that the horizontal outflow from this microburst is confined in a shallow layer from

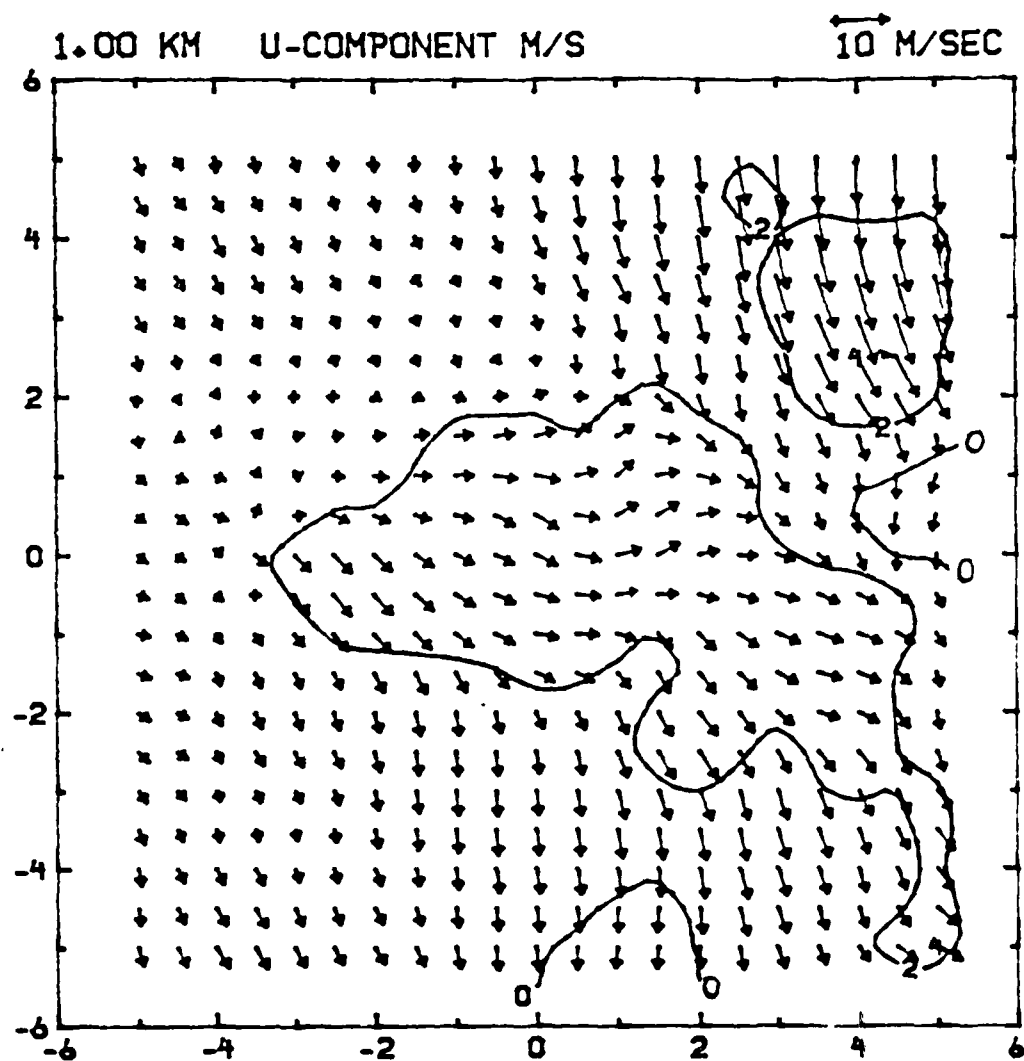


Fig. 6.3 As in Fig. 6.1 except for 1.0 km.

the surface to 1 km AGL. This is consistent with many of the examples cited by Fujita (1985).

Figure 6.4 shows the reflectivity pattern at 0.25 km superimposed on the horizontal wind field. The center of the microburst is marked by "M". Contours are 10 dBz beginning with 20 dBz. The high reflectivity within 0.25 km of the surface suggests that this is a wet microburst. Wilson et al. (1984) displayed the 0.05 km pattern of reflectivity and wind for 1641, 1643, 1646 and 1648 MDT. They showed a similar high reflectivity pattern 50 m from the surface for the entire period. This lends credence to the suggestion that at 1647 MDT this storm was in its mature stage rather than developing and was a wet rather than dry microburst. It is unfortunate that this storm occurred outside the PAM sampling region. Thus no real observational confirmation of this fact exists. Their results also confirm the strength of the storm although a microburst impinging on the surface would tend to have more intense horizontal outflow.

Reflectivity and horizontal wind flow at 4.0 km AGL is shown in Fig. 6.5. This corresponds to the level nearest the base of the parent cloud. Most notable are the jet axis aligned from west to east and the zone of convergence just to the west northwest of

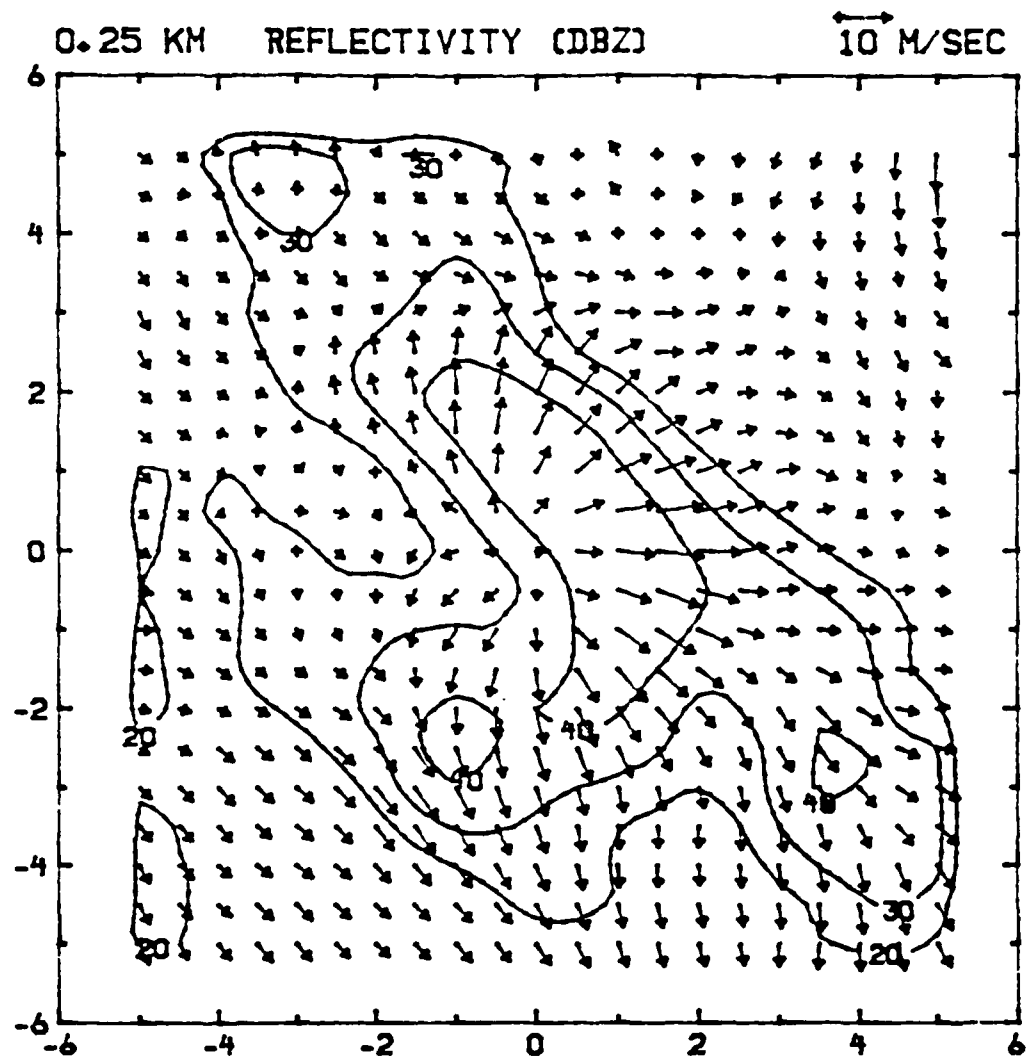


Fig. 6.4 As in Fig. 6.1 except for Reflectivity. Isopleths are at intervals of 10 dBz.

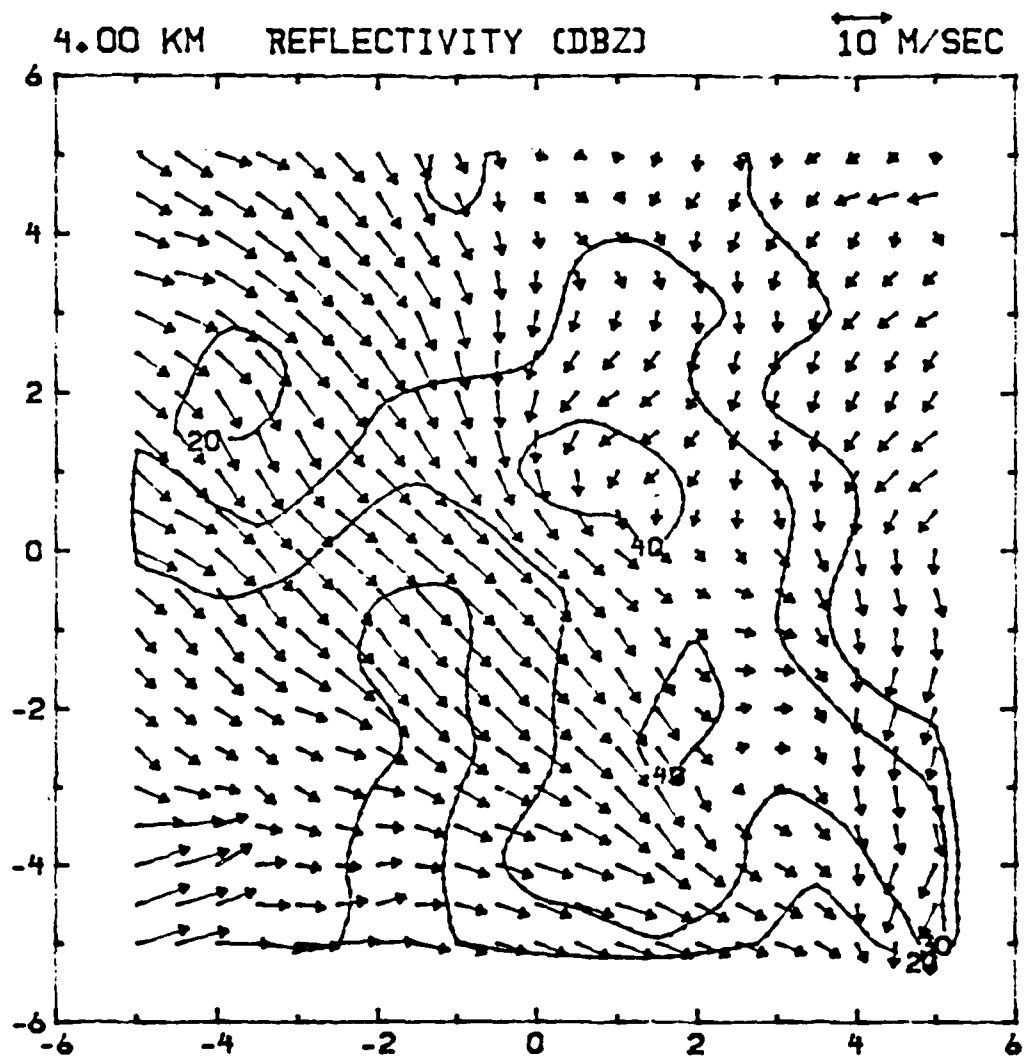


Fig. 6.5 As in Fig. 6.4 except for 4.0 km.

the northernmost reflectivity maximum. This convergence zone results from the flow of environmental air around a barrier formed by the precipitation core. The two areas of high reflectivity with  $Z > 40$  dBz reflectivity are associated with the two main precipitation cores within the storm. The large area of 20-30 dBz in the west northwest corner of the area represents the lower edge of the main storm cloud.

Overall examination of reflectivity and the horizontal wind structure of this storm suggests that it is in many ways "typical" of microbursts, exhibiting features and magnitudes detected by other investigators using both Doppler radar as well as other remote sensing devices.

#### 6.1.2 Vertical velocity

Figure 6.6 shows the vertical velocity pattern and horizontal storm-relative wind field at 0.50 km. Contour interval is  $2 \text{ m s}^{-1}$ . This level reveals the low level structure better since at 0.25 km the lower boundary condition that  $w=0$  at the surface reduces the magnitude of the vertical velocity. Grid distances are in km with the center of the grid coincident with the microburst at the surface. Note that the center of the microburst coincides with the downward velocity maximum at this level. Outside this core area of downward motion, there appears to be an annular ring



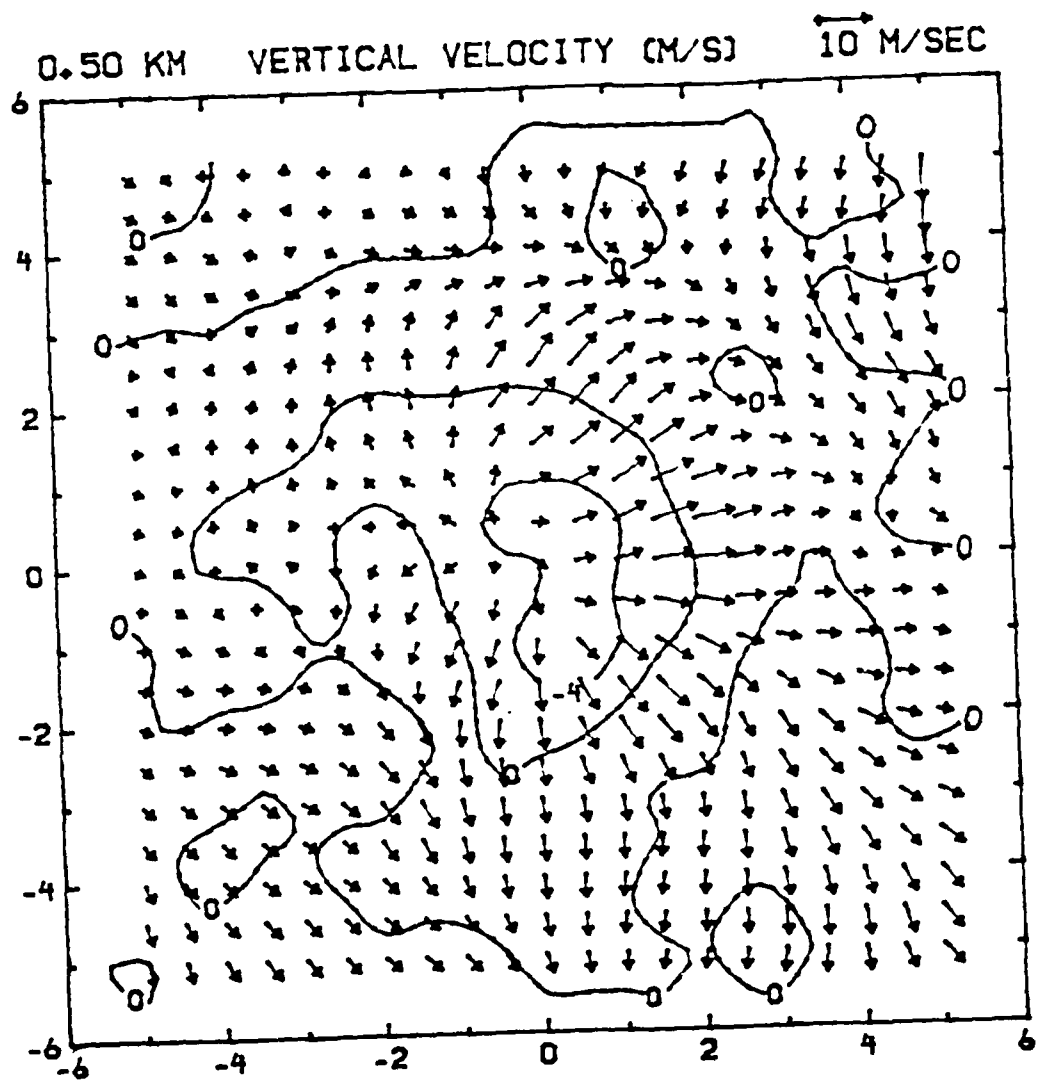


Fig. 6.6 Distribution of vertical velocity ( $w$ ) superimposed on storm-relative horizontal winds at 0.50 km. Isotachs are at intervals of  $4 \text{ m s}^{-1}$ .

of upward motion. This pattern is consistent with descriptions given in Fujita (1985). The largest upward velocities appear on the upwind side of the microburst. This area of strong upward motion results when the microburst outflow boundary near the surface forcing the incoming environmental air upward. Parsons et al. (1985) also found upward motion on the upwind side of another storm. They suggested that the outflow from the microburst is negatively buoyant compared to the surrounding air. This dense outward moving air would act in much the same manner as a gust front, lifting the more buoyant environmental air upward.

From Table 5.6, it is found that the maximum average vertical velocity occurs near the 1 km height. Figure 6.7 shows the vertical velocity superimposed on the horizontal wind field at this level. The annular ring of upward motion is still present and fairly well organized. The horizontal outflow is very weak at this level, again attesting to the shallow extent of the outflow region from this microburst. Figure 6.8 shows the vertical velocity pattern at 4.0 km. This represents the vertical velocity near the cloud base. With the exception of three small downdraft cores which are associated with reflectivity maximum most of the air is moving upward. The distribution of verti-

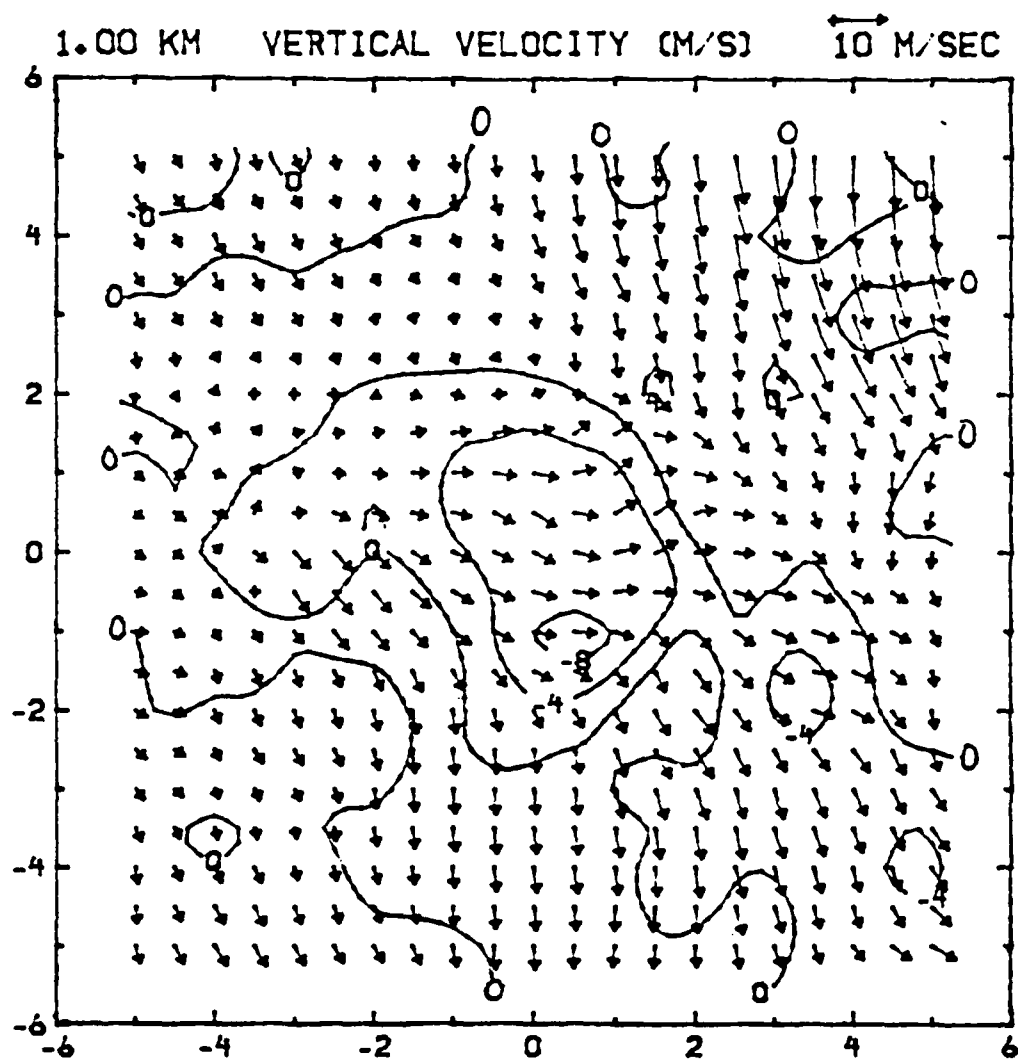


Fig. 6.7 As in Fig. 6.6 except for 1.0 km.

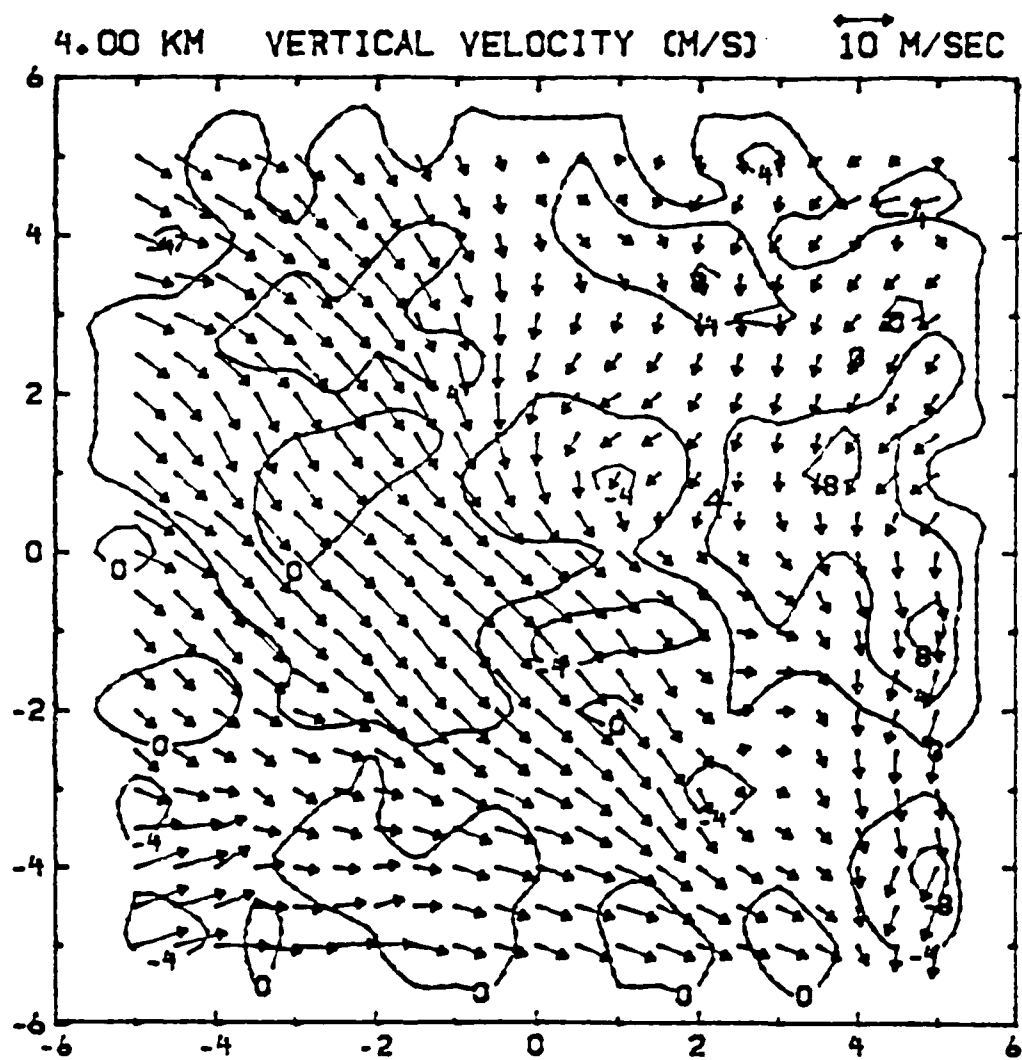


Fig. 6.8 As in Fig. 6.6 except for 4.0 km.

cal velocity at 6 km AGL is presented in Fig. 6.9. Inspection of Figs. 6.7, 6.3 and 6.9 reveals the existence of an updraft-downdraft couplet similar to that suggested by Lin et al. (1985). This couplet, also found by Pasken (1981), seems to be associated with more severe storms and storms in their developing stages. Lin et al. (1985) suggested that the updraft is linked to the weak echo region (WER) of inflow into the storm, and the downdraft is associated with the precipitation shaft near the right rear flank of the storm. Certainly, examination of Figs. 6.5 and 6.8 and Figs. 6.4 and 6.6 show that, in this storm, the downdraft is directly associated with the precipitation core of the storm. Examination of these reflectivity and vertical velocity patterns as well as other levels (not shown) suggest that in the lower levels the strong updraft on the downwind side of the storm is associated with lower reflectivities defining the edge of the storm rather than the WER imbedded within the storm. However, the updraft core to the upwind side of the downdraft is associated with the interaction of environmental flow and the storm itself.

The age and non-severity of the storm suggest that if any such couplet, i.e., rear flank downdraft - WER, had existed it has dissipated. A number of mechanisms could have contributed to this dissipation.

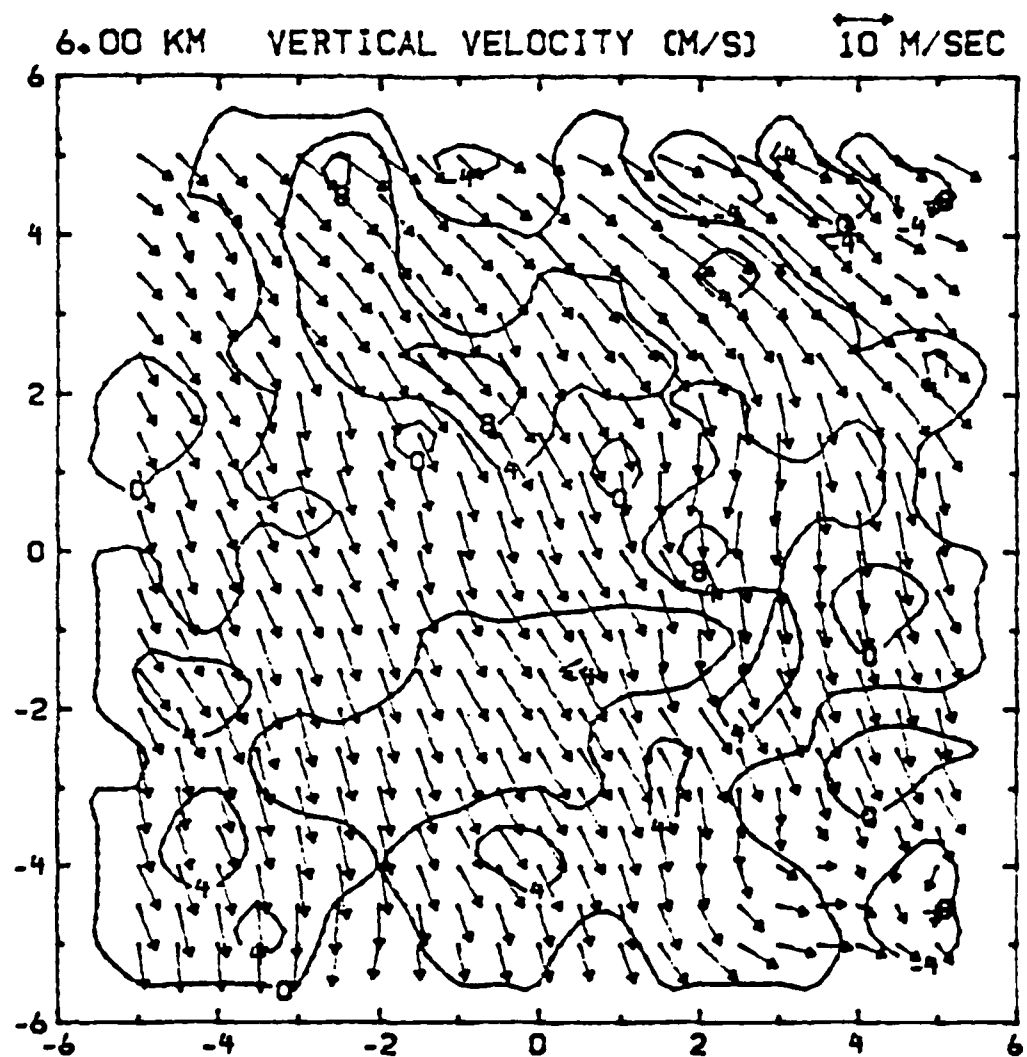


Fig. 6.9 As in Fig. 6.6 except for 6.0 km.

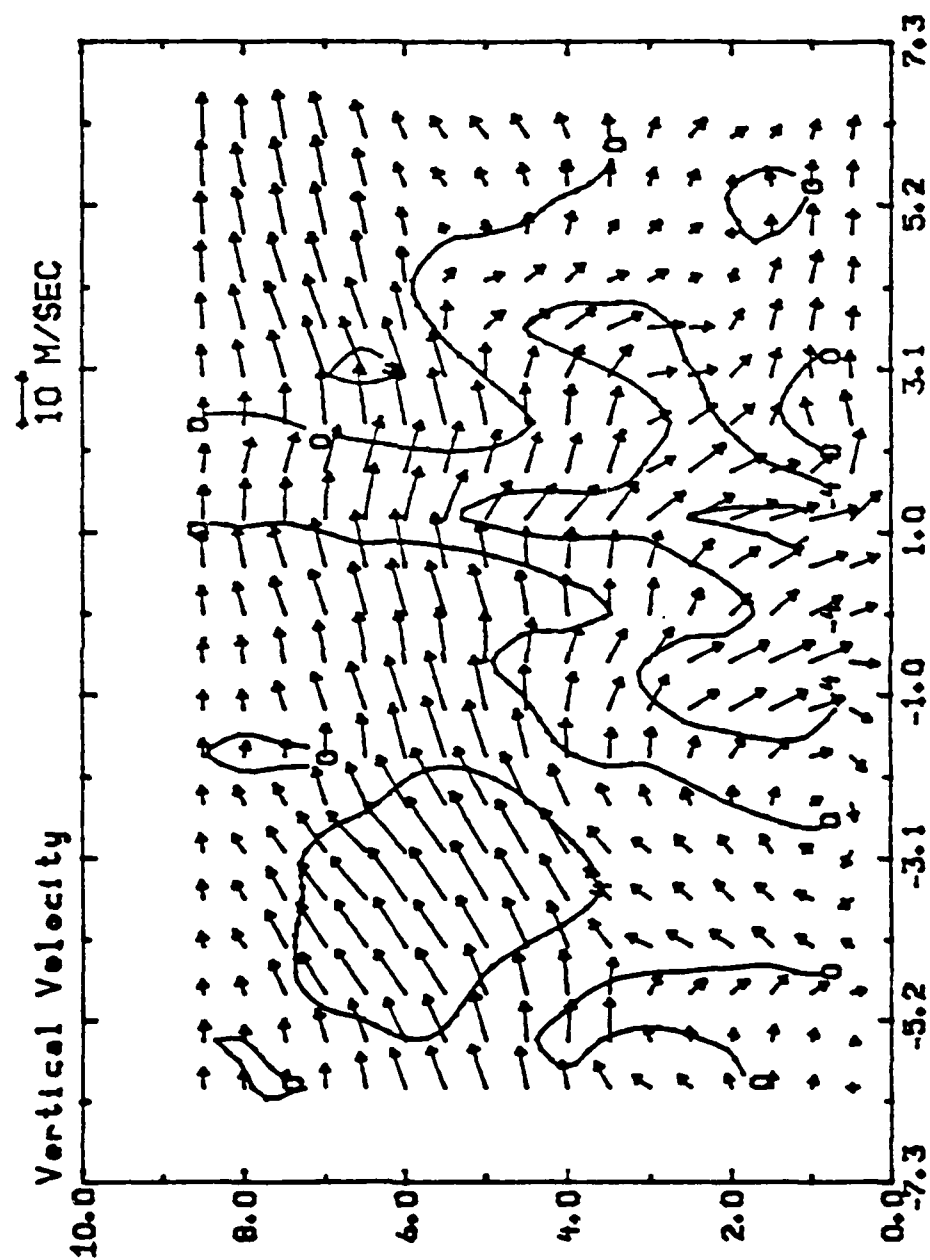
Precipitation loading, as evidenced by the high reflectivities at low levels, could have destroyed the updraft region. This is suggested in the Byers and Braham (1949) thunderstorm model where the updraft is replaced in the mature stage of the storm by a downdraft created by downward moving cooler air and precipitation.

Figure 6.10 shows the vertical cross section of the wind field along line AB from Fig. 6.1. The horizontal component of the wind has been converted to in-plane wind, i.e. it is a vector combination of the  $u$  and  $v$  component wind lying parallel to the plane. The full vertical extent of the microburst is evident. The connection between incoming environmental air at 4.0 km and the microburst at the surface is clear.

The vertical cross section of reflectivity superimposed on the in-plane wind field is shown in Fig. 6.11. Three areas of interest are labeled A, B and M on Fig 6.11. Area A appears to be a gust front associated with the outflow region from the main reflectivity core (B). The microburst (M) is located in a region of high reflectivity gradient and upwind of the reflectivity maximum. The horizontal flow is diverted downward by this core of maximum precipitation acting as a barrier to flow. This effect when coupled with downward motion created by the precipita-

Fig. 6.10 Vertical cross section along line AB showing vertical velocity superimposed on 3-dimensional wind field. Horizontal wind is the in-plane wind constructed from  $u$  and  $v$  components. Isotachs are at intervals of  $4 \text{ m s}^{-1}$ .

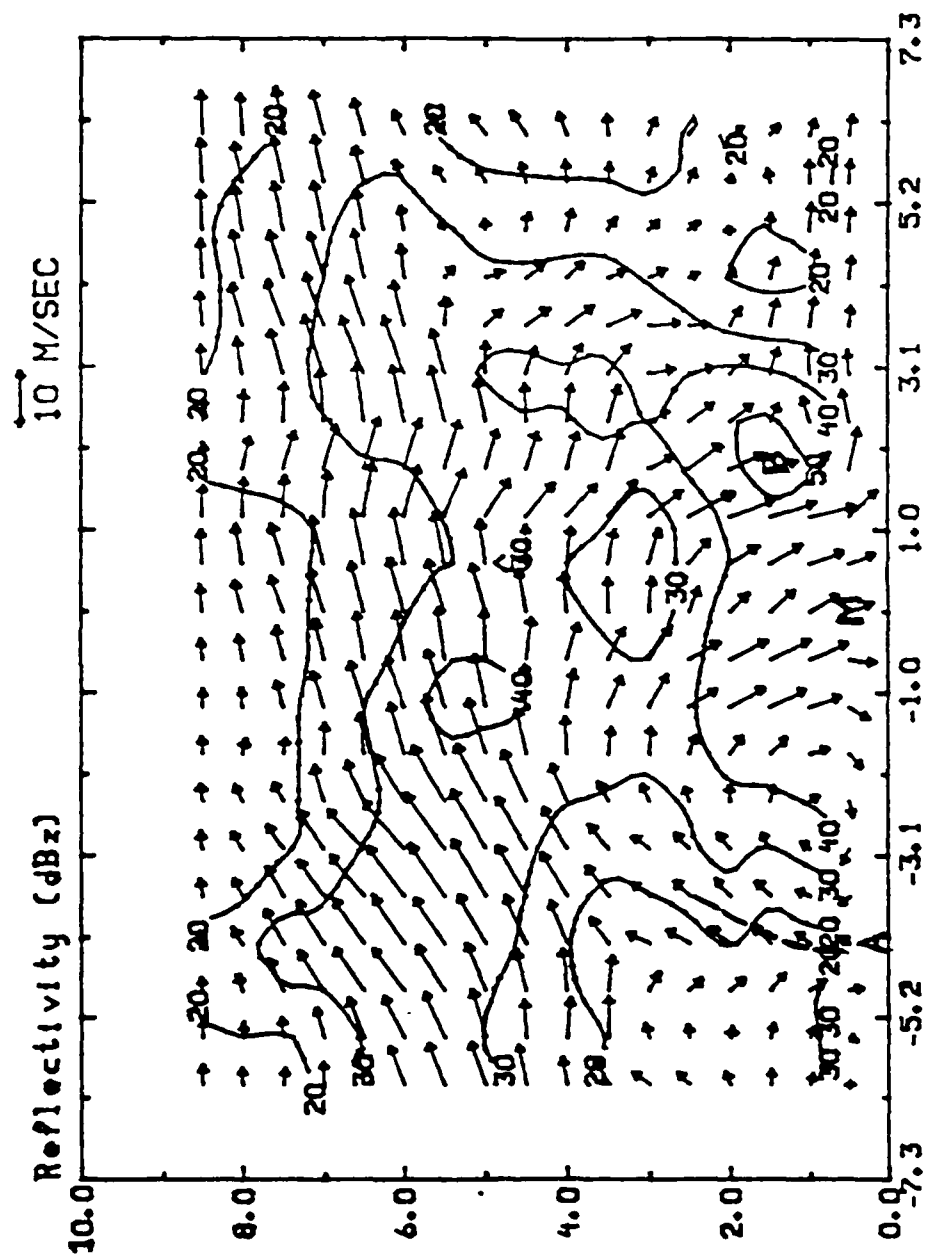




tion drag enhances the microburst. Lin et al. (1985) found a similar mechanism within their study. Fujita (1985) suggested that in wet microbursts effects from evaporative cooling are reduced and precipitation drag and downward deflection of horizontal wind become more important. The updraft on the upwind side of the microburst is associated with the edge of the cloud boundary distinguished by the 20 dBz isoline. It is the result of convergence of environmental air being deflected around the precipitation core and environmental air entering the storm from the west northwest.

The gust front (A) appears to be associated with the 20 dBz line nearly 4.5 km from the microburst. From the kinematic analysis of Wilson et al. (1984), see their Fig. 1, it appears that the microburst began to form around 1641 MDT. The first sign of divergent outflow occurred on the south side of the 40 dBz contour, located at 13.5 west and 17.5 south of CP-2. Two minutes later, the divergence increased to  $5 \times 10^{-3} \text{ s}^{-1}$  reaching the maximum ( $2 \times 10^{-2} \text{ s}^{-1}$ ) at 1646 MDT. The strong diverging outflow from the microburst center interacts with the environmental flow from the west to form a microburst gust front near area A (Fig. 6.11). A vortex ring suggested by Fujita (1985) is clearly seen between A and M.

Fig. 6.11 As in Fig. 6.10 except for reflectivity. Isopleths are at intervals of 10 dBz. (A) and dashed line denote microburst surface outflow boundary. (H) marks the center of the microburst and (B) is the reflectivity maximum along line AB.



A small rotor feature, associated with the vortex ring, exists approximately 2 km on the upwind side of the microburst. This rotor marks the boundary of the outflow region near the surface (dashed line). The vertical effect of the rotor associated with this gust front appears to extend to near the 2 km AGL level. Examination of other wind cross sections (not shown) as well as Fig 6.9 suggests that the rotor feature does not extend completely around the downburst nor does the gust front. The absence of the gust front a rotor in certain sections of the microburst region seems to be related to intensity of the microburst, motion of the parent storm, and the strength and direction of the environmental air flow. Fujita (1985) suggested that the presence of a distinguishable rotor in a mild microburst tends to be on the upwind side of the main outrush center, while the feature on the downwind side is "smeared" by the environmental wind.

When looking at the vertical velocity patterns in total, one gets the impression that the storm seems to be in two parts. The first part is the subcloud (below 4.0 km) section, while the upper portion is the cloud section. The prevalence of downward motion in the subcloud layer and only one portion of the cloud section associated with a reflectivity maximum which

extends from near the top of the cloud to the surface, suggests that the storm may be separating horizontally. This would seem reasonable if the storm were in its mature or dying stage.

### 6.3 Divergence

Figure 6.12 depicts the divergence pattern associated with the microburst at 0.25 km. Values near the center of the microburst are on the order of  $10^{-2} \text{ s}^{-1}$ . The area of convergence which rings this central divergence core is associated with mass convergence between the outflow of the microburst and the environment. This zone of convergence is approximately half the magnitude of the central divergence area. In Fig 6.12, a dashed line shows the microburst gust front. It coincides with the axis of maximum convergence approximately  $5 \times 10^{-3} \text{ s}^{-1}$ . Figure 6.13 shows the vertical cross section of divergence along line AB in Fig. 6.1. Contour interval is  $2.5 \times 10^{-3} \text{ s}^{-1}$ . The storm-relative wind is superimposed. Divergence exists throughout the entire region of the microburst with the maximum values near  $10^{-2} \text{ s}^{-1}$  near the surface. The two areas of convergence approximately 2-3 km from the center of the microburst represent the ring of convergence associated with the microburst outflow interaction with the environmental wind. Maximum values within this ring are much

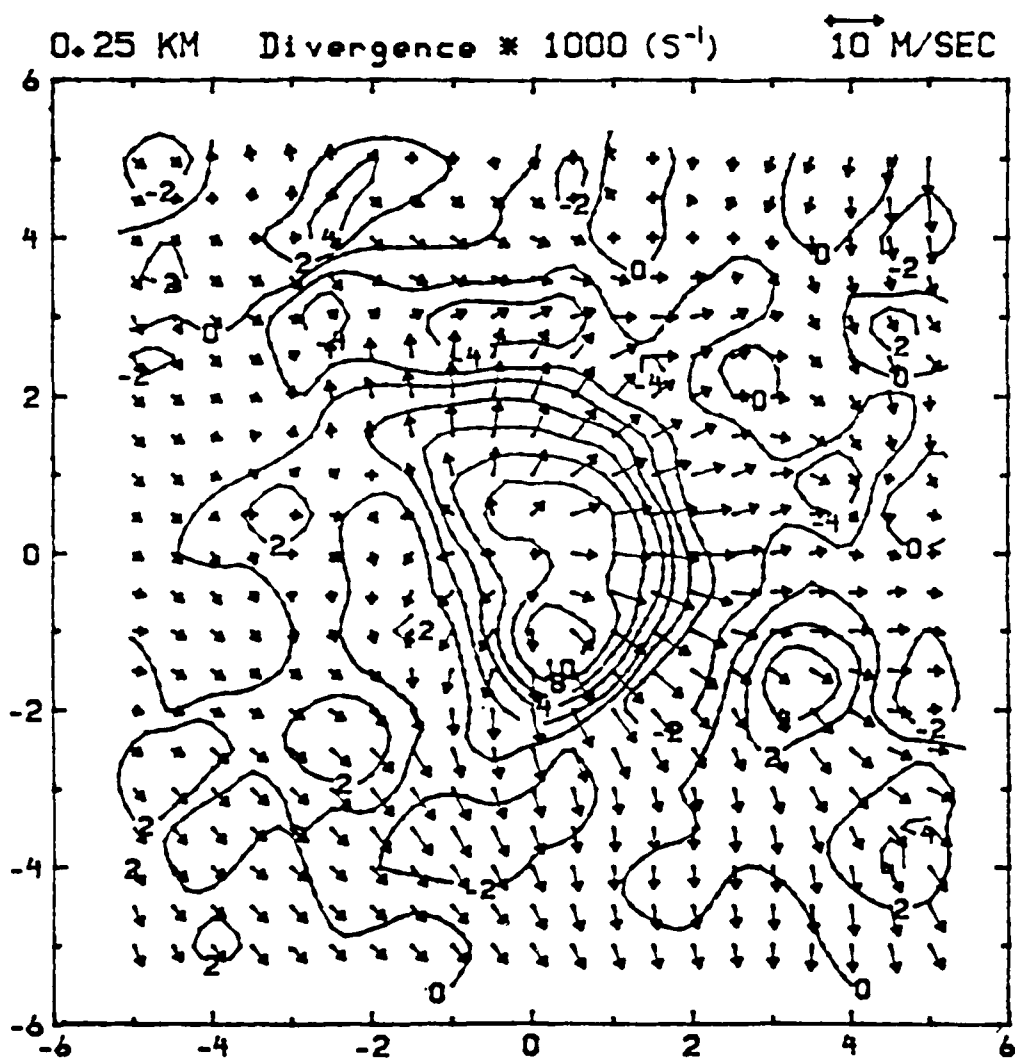


Fig. 6.12 As in Fig. 6.1 except for Divergence with units of  $10^{-3}s^{-1}$ . Isopleths are at intervals of  $4 \times 10^{-3}s^{-1}$ .

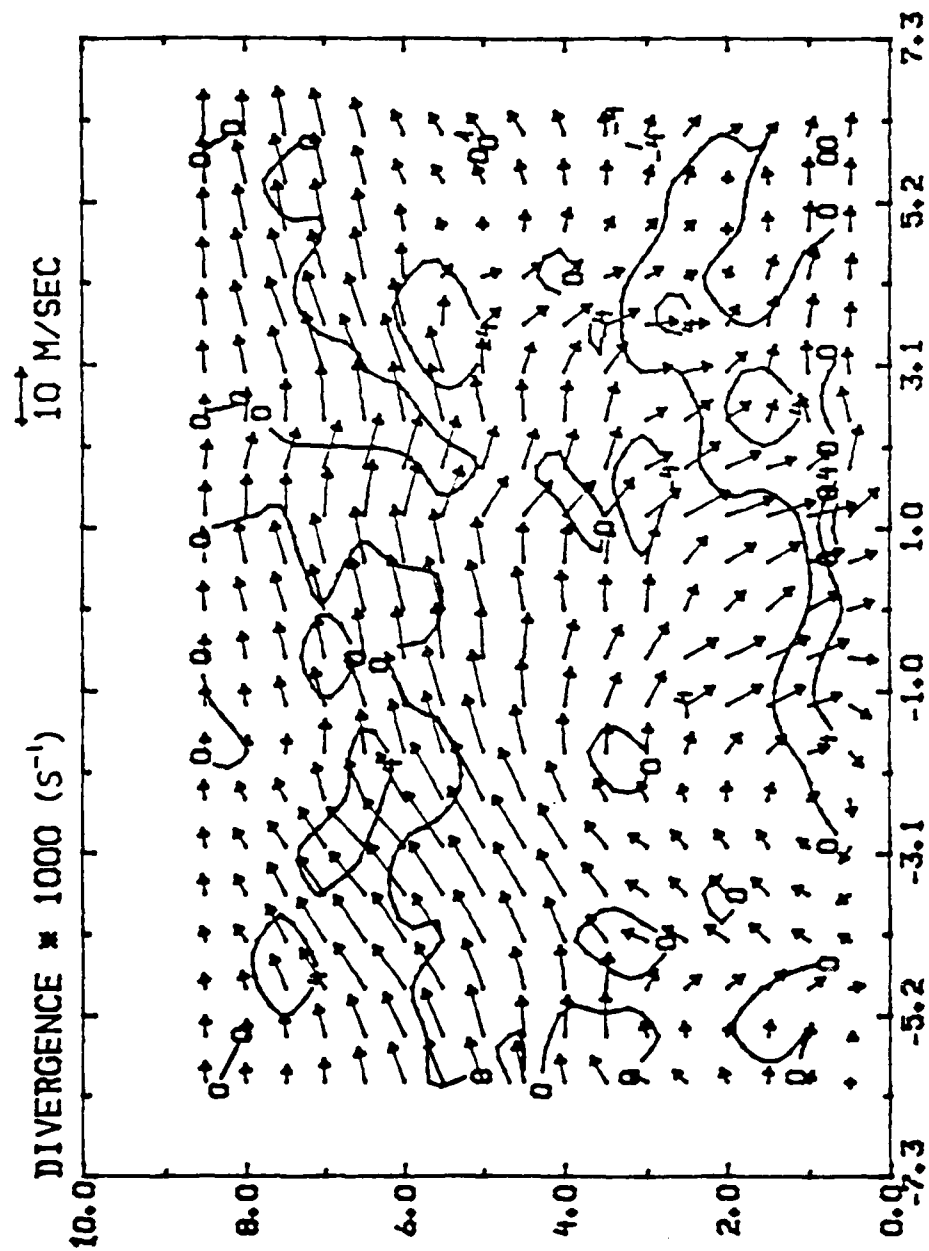


Fig. 6.13 As in Fig. 6.10 except for divergence in units of  $10^3 \text{ s}^{-1}$ .



smaller in magnitude than at the center of the microburst. Note that the diverging outflow is mainly confined to the layers from the surface to approximately 2 km. Above this level, convergence dominates due to the mass continuity requirement to maintain strong downflow within the downdraft and the convergence zone created by deflecting the environmental flow, see Fig. 6.8.

#### 6.4 Deviation Perturbation Pressure, $P_d'$

The retrieved  $P_d'$  field for 0.25 km is shown in Fig. 6.14. As expected there is a stagnation mesohigh up to 15 Pa inside the microburst. This stagnation high is surrounded by a broad region of low pressure in the strong outflow area. Such a pressure pattern is similar to those shown in Fujita (1935) for the Andrews AFB microburst. The center of higher pressure was located slightly on the downwind side of the microburst. This is a manifestation of the effect of the environmental air skewing the microburst downwind. Fujita (1935) suggested that a low pressure ring exists outside the stagnation high in a downburst. This can be seen readily in Fig 6.14. It completely surrounds the storm but has been modified by the environmental wind flow. The upwind side of the storm has stronger low pressure than the downwind side. The

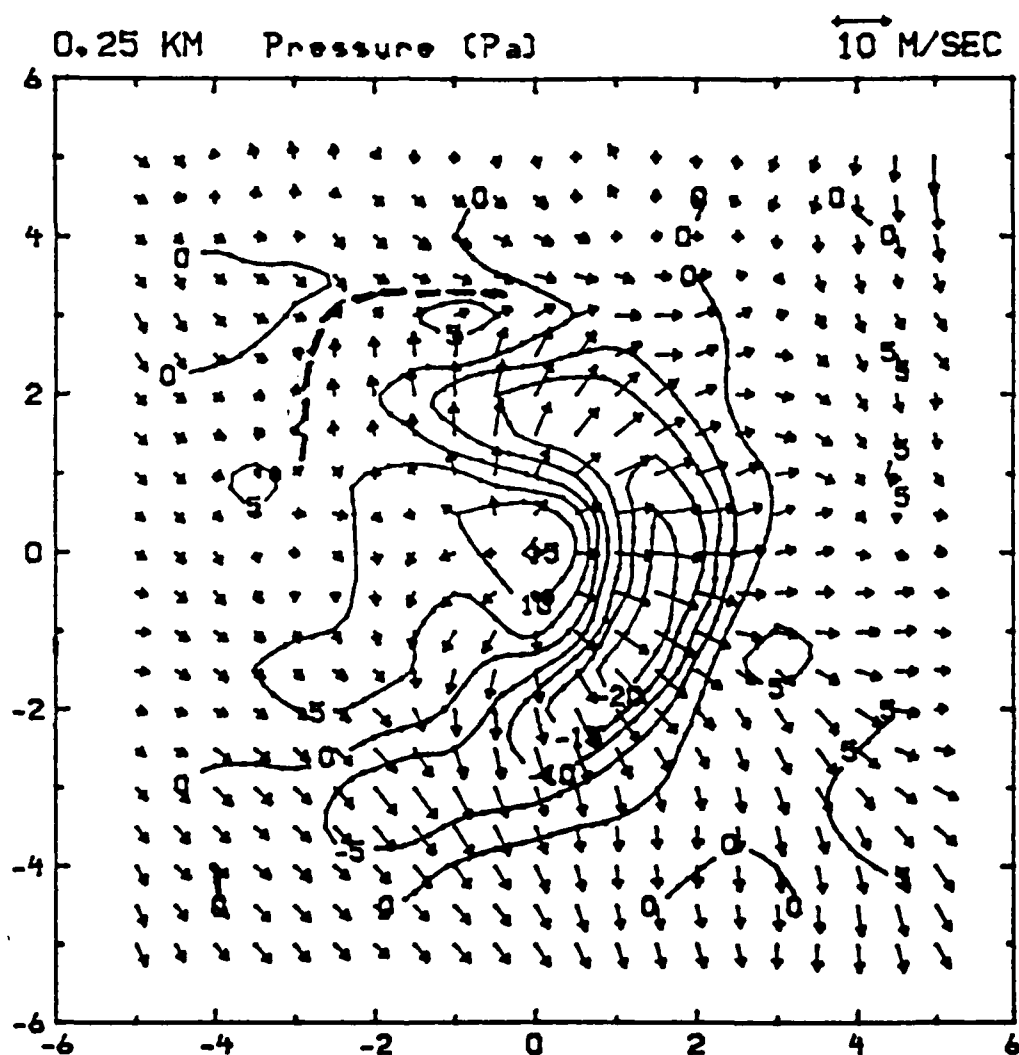


Fig. 6.14 As in Fig. 6.1 except for deviation perturbation pressure. Isobars are at intervals of 5 Pascals (Pa).

rotor and gust front (dashed line) show up in the pressure pattern as a relative maximum as one would expect from a convergent situation.

Figure 6.15 shows that maximum positive pressure exists at 0.75 km AGL in the microburst. Values of +0.3 mb are found in there. As expected, the values are smaller than those found in other studies, e.g., Lin et al. (1985), Pasken (1981) and Wirsing (1985). However, all these storms were much stronger in nature than a microburst producing storm similar to the one being investigated. Parsons et al. (1985) working with another JAWS storm found retrieved pressure values of 0.5 mb near the center of the microburst at 0.25 km.

The horizontal pressure distribution at 4 km AGL is displayed in Fig 6.16. This level is slightly above the cloud base where the prevailing environmental wind begins to interact with the main body of a microburst-producing storm. Inspection of Fig. 6.16 reveals that high pressure, labeled H, is observed to the northwest of the main updraft (U) with low pressure, labeled L, to the southeast. The orientation of maximum pressure gradient determined in the vicinity of U is approximately in the direction of the environmental wind shear vector,  $d\vec{V}_e/dz$ , from the northwest. This shear vector is determined from Denver's sounding

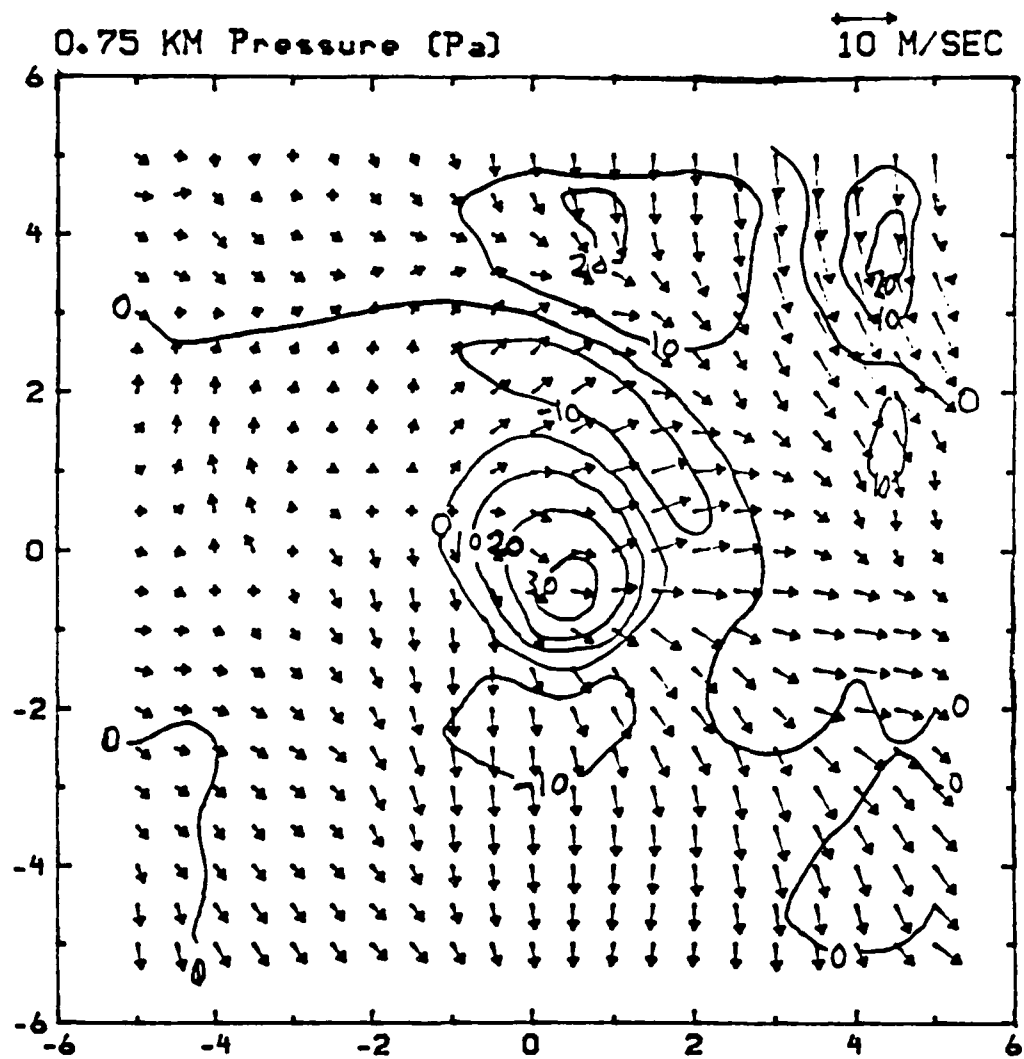


Fig. 6.15 As in Fig. 6.14 except for 0.75 km.

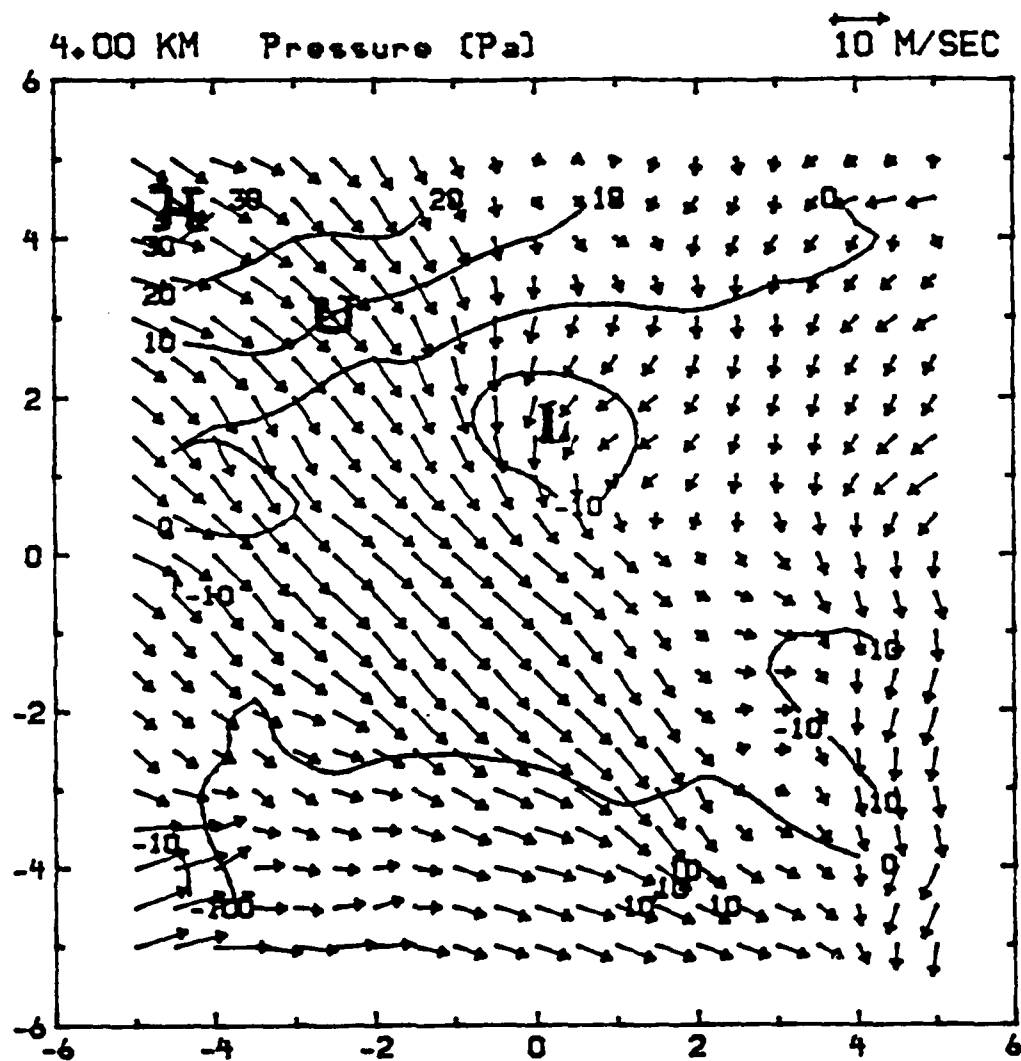


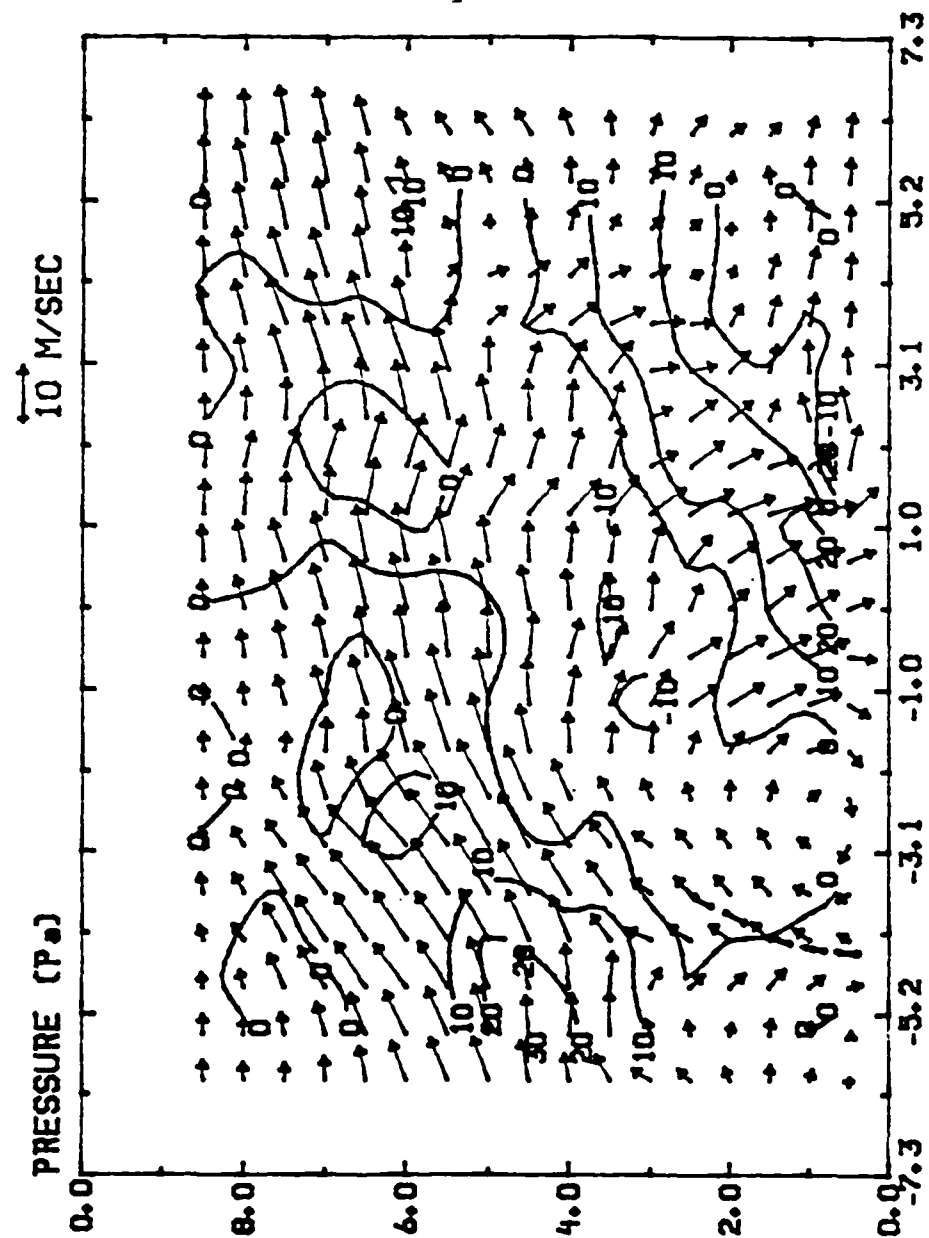
Fig. 6.16 As in Fig. 6.14 except for 4.00 km. Isobars are at intervals of 10 Pascals (Pa).

shown in Fig. 3.3. Our finding is in good qualitative agreement with the linear theory of Rotunno and Klemp (1982). The theory predicts that the dynamic interaction between the sheared environmental wind and the storm's updraft creates high pressure on the upshear flank with low pressure on the downshear flank. The magnitude of pressure perturbation near the updraft is proportional to the magnitude of the height dependent shear vector,  $d\vec{V}_e/dz$ , multiplied by the horizontal gradient of vertical velocity  $\nabla_h w$  along the shear vector. Thus, the pressure pattern with the main body of the parent storm displayed in Fig. 6.16 appears to be reliable. A horizontal perturbation pressure gradient,  $\nabla_h p_d'$ , from mesohigh H to mesolow L is quite pronounced. The magnitude is about 30 Pa (0.3 mb) over a distance of 5 km which is much smaller than those reported in studies by Brandes (1984), Hane and Ray (1985) and Lin *et al.* (1985) for severe convective storms. It is worth noting that the presence of high pressure (H) on the upshear side of U plays an important role in affecting the structure and internal dynamics of a microburst-producing storm. It will be shown later that this stagnation high results in favorable 3D perturbation pressure gradients over that region and is partially responsible for initiating and maintaining a downdraft which produced the microburst

in the lower layers.

Figure 6.17 shows the vertical cross section of the perturbation pressure field along line AB in Fig. 6.1. Contour interval is 10 Pa (.1 mb). The storm relative wind field is superimposed to show the relationship between the pressure and flow pattern. Of interest is the pressure maximum located at 4.5 km. This is caused by the interaction between the environmental flow and the storm acting as a barrier. It also coincides with the edge of the main storm delineated by the 20 dBz isoline. The air entering the storm is relatively dry. As it entrains air within the cloud, it becomes cooler. This would cause it to descend. This in combination with the interaction with the maximum precipitation shaft enhances and maintains the downdraft which eventually becomes the microburst. The ring of low pressure is present and the low pressure on the upwind side coincides with the gust front and rotor near the surface. The leading edge of the outflow is marked with a dashed line.

Fujita (1985) suggested that a close relation between the perturbation pressure and the horizontal wind. Figure 6.18 shows this relationship for the 0.25 km level along line AB in Fig. 6.1. As expected, and in agreement with Fujita (1985), when the pressure





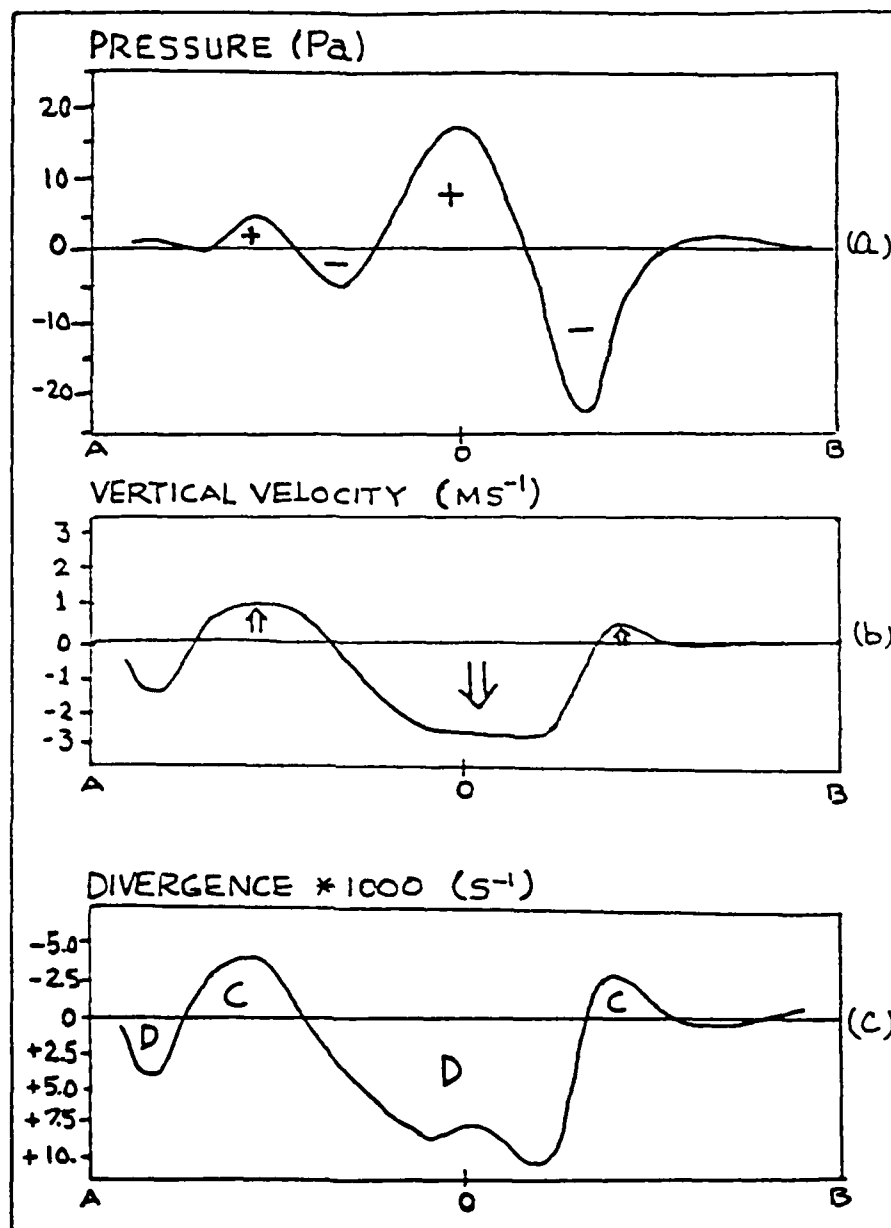


Fig. 6.18 The distribution at 0.25 km of (a) deviation perturbation pressure in Pascals, (b) vertical velocity ( $w$ ) in  $\text{m s}^{-1}$ , (c) divergence in  $10^{-3} \text{s}^{-1}$ , (d) deviation perturbation temperature in  $^{\circ}\text{C}$  and (e) in-plane horizontal velocity in  $\text{m s}^{-1}$  along line AB.

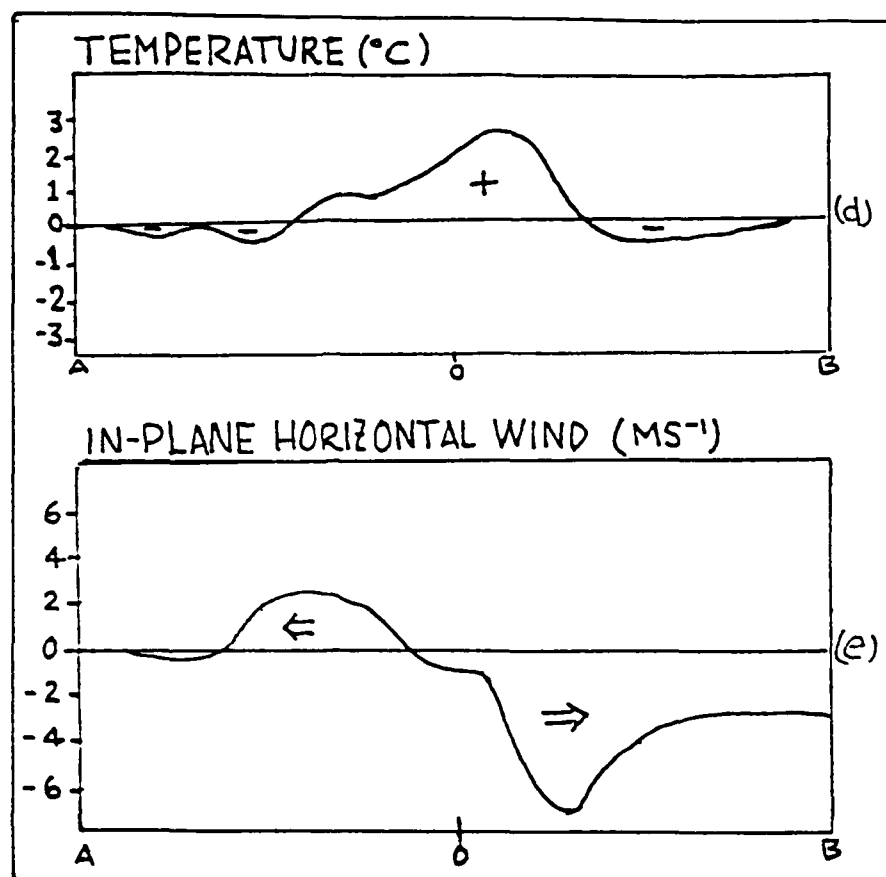


Fig. 6.18 continued

is increasing the horizontal velocity is decreasing and visa versa. The asymmetry of the pressure is due in part to interaction of the microburst outflow with the environmental wind. The horizontal outflow on the "upwind" side of the microburst is slowed down due to this interaction and consequently a higher pressure is created on the upwind side. This asymmetry is also reported by Fujita (1985). The vertical velocity profile is as expected. Upward motion is associated with the convergence and lower pressures, while the downward motion is associated with the higher pressures and divergence of the microburst center. The asymmetrical updrafts are due to environmental interaction smearing out the updraft on the downwind side of the microburst. The divergence associated with the central outflow region of the microburst is accompanied by a convergence zone on either side. These convergent zones amount to the microburst outflow gust front. Again the asymmetry in the central divergence zone is associated with the environmental flow effect. The maximum divergence is associated with the horizontal velocity maximum on the downwind side of the microburst. The larger convergent area is associated with the gust front and the rotor discussed earlier. The warm deviation perturbation temperature is skewed toward the downwind side of the microburst center.

The lower temperature surrounding the central warm core is seen as the two negative areas.

#### 6.5 Deviation perturbation virtual temperature, $T_{vd}'$

Figure 6.19 shows the deviation perturbation temperature for 0.25 km. Remember, this temperature is the deviation from its horizontal mean instead of the deviation from the environmental temperature. Hence, it does not represent the true perturbation virtual temperature,  $T_{vd}'$ . It contains the unknown area mean temperature  $\langle T_{vd}' \rangle$ . For this reason, caution must be exercised when interpreting the temperature field. A temperature maximum of 3.0 degrees is located just downwind from the microburst center. The non-symmetry is due to modification by the environmental flow. Fujita (1983) and Srivastava (1985) suggested that positive deviations of temperature in this region are quite plausible, and in the case of a wet microburst somewhat more expected.

Srivastava (1985) employed a simple evaporatively driven downdraft model to show that near the end of the life cycle of the downburst, a positive temperature perturbation developed near the surface coupled with a negative temperature perturbation directly above, see his Figs. 1 and 2. This pattern can be seen in Fig. 6.20 which represents the cross section of deviation perturbation virtual temperature along

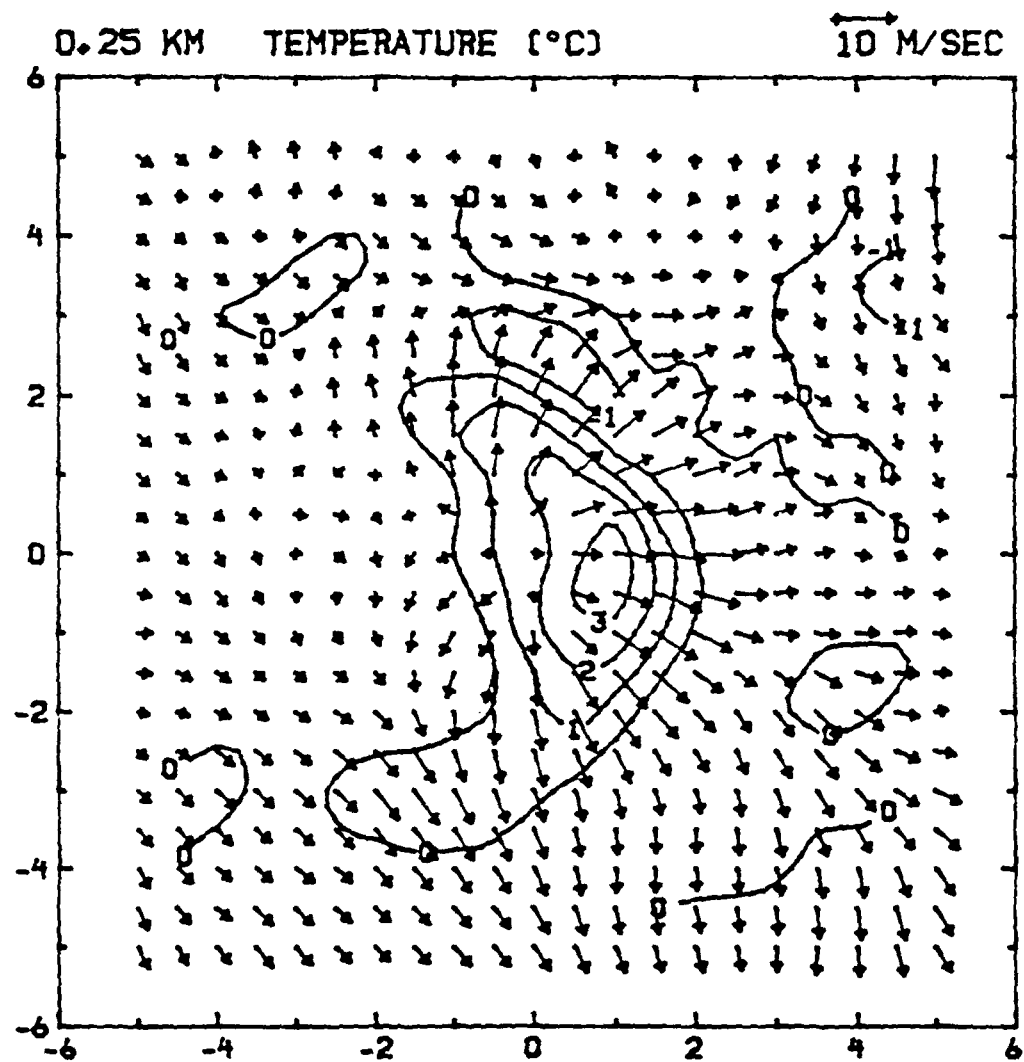


Fig. 6.19 As in Fig. 6.1 except for deviation perturbation virtual temperature. Isopleths are at intervals of  $1^{\circ}\text{C}$ .

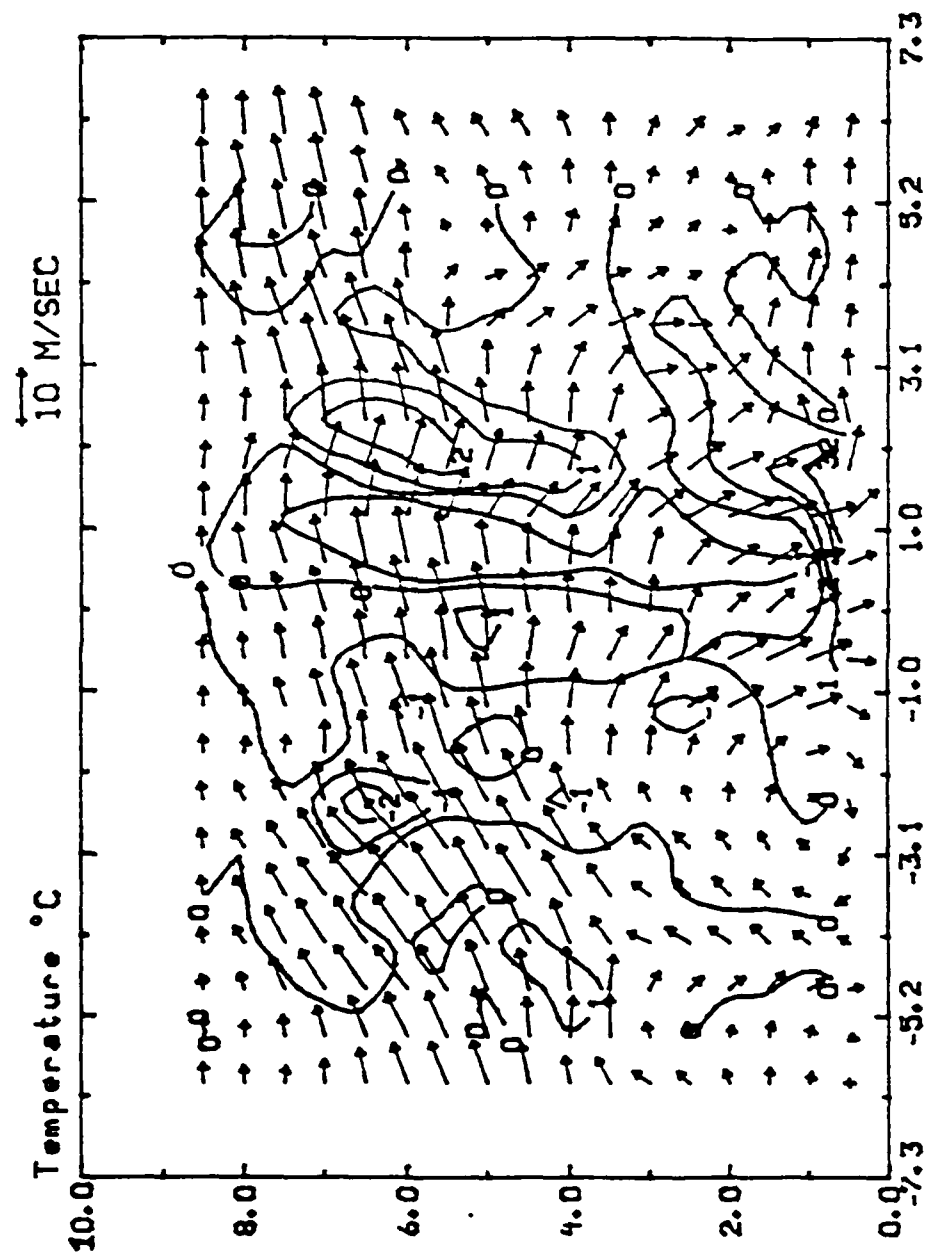


Fig. 6.20 As in Fig. 6.10 except for deviation perturbation virtual temperature.

line AB. Srivastava demonstrated that even though the downdraft air is warmer than the surrounding environmental air, its thermal buoyancy is negative since it is drier and hence virtually cooler than its surroundings. At upper levels, the total buoyancy of the air is a combination of the thermal buoyancy and the rainwater mixing ratio. In the case of the wet microburst, the rainwater loading overcomes the thermal buoyancy to produce a negative total buoyancy and hence enhances downward motion.

Reflectivity patterns suggest that the microburst is imbedded within a precipitation area. Thus air descending from the cloud base would not have the benefit of evaporative cooling to reduce the temperature. If such a parcel were to descend totally within a region of 100% relative humidity, it would in fact increase in temperature in a nearly dry adiabatic fashion (Srivastava, 1985). The second explanation involves the age of the storm. The value being computed is the deviation perturbation virtual temperature. If the storm were mature, cooler air descending earlier in the storm could have cooled the environment below the cloud. At the time of this study, the deviation perturbation temperature would then be positive. Fujita (1985) suggested that this scenario is quite possible especially within wet microbursts.

## CHAPTER 7

### Summary and Conclusions

The method developed by Armijo (1969) was used to derive the 3D wind field from dual-Doppler radar measurements of a convective storm producing a microburst. The storm occurred on 14 July 1982 during the Joint Airport Weather Studies (JAWS). Vertical velocities were obtained by integrating the anelastic continuity equation downward from the storm top near 8.5 km to the surface. After correcting the vertical velocity to conform to the lower surface boundary condition that  $w=0$ , the horizontal wind was corrected using the variational approach similar to that of Ziegler et al. (1983) and Lin et al. (1985). This correction was necessary to bring the 3D wind field again into anelastic balance. Once the wind field was derived, a thermodynamic retrieval technique was employed to recover fields of deviation perturbation pressure, density and (virtual) temperature. These fields were then subjected to internal consistency checks to determine the adequacy of the recovery procedure prior to physical interpretation.



In an effort to determine whether the retrieval method (which seemed to perform well in the strong storm environment) would be sensitive enough to produce usable results on a milder storm, a number of experiments were done, see Table 5.1. Our findings show that:

- 1) In order to extract thermodynamic variables from 3D wind fields, these wind fields must be brought into anelastic balance. Failure to do this produces thermodynamic fields which, at best, can be used to describe only grossest of features.
- 2) Inclusion of a frictional parameterization scheme in the computation of pressure and temperature is needed, especially near the surface, where the frictional effect is most pronounced.
- 3) Inclusion of a precipitation drag term is necessary for the temperature recovery scheme. This is especially true in cases of wet microbursts where this term plays a very important role in the retrieval. Failure to include such a term will result in errors which are on the same order of magnitude with the retrieved temperature and are biased by the reflectivity field.
- 4) The thermodynamic retrieval scheme is insensitive to inclusion of a relatively small random error ( $<10\%$ ) in the radial wind field. However, large random

errors in the wind field would distort the retrieved field greatly, thereby producing very little useful information.

5) Patterns and strengths of features associated with the microburst are weaker for this storm when compared to those of more spectacular and stronger storms studied by others. The existence of a warm center below the microburst was verified. This conforms well with scenerios suggested by Srivastava (1985) and Fujita (1985).

6) Precipitation drag as well as a mid level stagnation pressure high upwind of the microburst seem to be the driving force behind sustaining the microburst during the mature and decaying part of its life. This does not preclude the possibility that during the early stages of this event, subcloud evaporative cooling acts to enhance downward motion below the cloud.

This study does answer some of the questions raised about the sensitivity of the procedure to retrieve dynamic and thermodynamic variables from dual-Doppler scans. It also provides a qualitative if not quantitative look at the structure of a microburst producing storm which was relatively weak by comparison to most of the other storms studied. There are still a number of questions which remain to be

considered. First, to what extent does inclusion of the temporal term in the computations alter the retrieved fields and their magnitudes? Secondly, and from the aviation point of view, how often do weaker storms produce microbursts which could be hazardous to aircraft performance? Finally, and most important, is it possible to predict the microburst event prior to its affecting aircraft performance using a single Doppler radar?

## APPENDIX A: Object Analysis Schemes

### 1. Introduction

The objective map analysis scheme developed by Barnes (1964) has been widely used by the meteorological community. It only requires four passes (3 iterations) to arrive at an interpolated field which fits the observations. The earlier version of the scheme was modified by the author (Barnes, 1973) to include the following features:

1. It reduces the number of passes to two (one iteration) to obtain the desired interpolated field.
2. It enhances detail in the interpolated field by including time-series observations.

The first feature is specifically designed to speed up the rate of convergence, thereby reducing the computational time. By properly changing a weight function parameter, details which require four or more passes through the data heretofore now become discernible with only two passes.

### 2. Response Function

Consider an atmospheric variable  $f(x,y)$  which is uniform in the Y-direction and is expressed as

$$f(x,y) = A \sin(ax) \quad (A1)$$

where  $a(= \frac{2\pi}{\lambda})$  is the wave number, and  $\lambda$  is the wave

length. We wish to obtain the interpolated variable  $g(x,y)$  at some grid point  $(x,y)$  from the observed data at point  $(x+r\cos\phi, y+r\sin\phi)$  (see Fig. A1), and filter (weigh) the data according to their distance  $(r)$  from the point  $(x,y)$ , i.e.,

$$g(x,y) = \int_0^{2\pi} \int_0^{\infty} f(x+r\cos\phi, y+r\sin\phi) w(r,k) r dr d\phi \quad (A2)$$

where the weight function is

$$w(r,k) = \frac{1}{4\pi} \exp\left(-\frac{r^2}{4k}\right) \quad (A3)$$

and  $k$  is a parameter (weighting factor) to be determined.

Equation (3) is a well known Gaussian function. Its shape is uniquely determined by the standard deviation  $\sigma = \sqrt{2K}$ . Hence, larger values of  $K$  will give flat curves, while smaller values will provide sharp bell-shaped curves.

We wish to determine the relationship between the observed value,  $f$ , and the weighted average value,  $g$ , at the same point  $(x,y)$ , i.e.,

$$g(x,y) = D(a,k)f(x,y) \quad (A4)$$

where  $D(a,k)$  is the response function and is a function of the wave number  $a (= 2\pi/\lambda)$ . It can be shown that the filtered response to  $f(x,y)$  is

$$D(a,k) = e^{-a^2 k} = e^{-\left(\frac{2\pi}{\lambda}\right)^2 k} = e^{-4k(\pi/\lambda)^2} \quad (A5)$$

which does not alter the phase of the original function, but acts only to damp the amplitude. Rela-

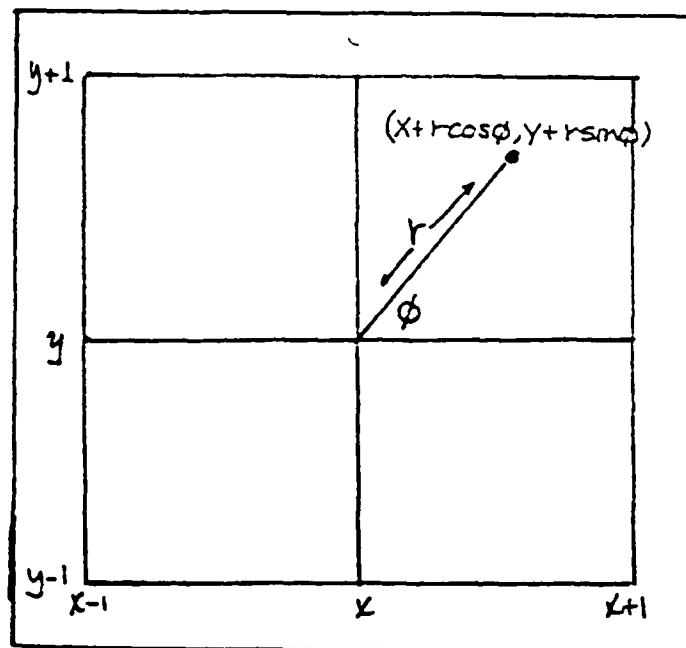


Fig. A1 Relationship between the data point and the grid points for Barnes scheme.

tionship of the response function,  $D(a,k)$ , the wave length,  $\lambda$ , for various choices of the parameter  $k$  is shown in Fig. A2. It indicates response corresponding to initial (first pass) through the data with a Gaussian type filter [Eq.(A3)]. In general, response is nearly zero for very short waves and approaches one for very long waves.

Ideally, one can select a small  $k$  which allows us to define the effective cut-off wavelengths (see Fig. A2) and yet be confident that very short waves (noise) are suppressed. However, the practical lower limit on  $k$  is determined by the data density and distribution. For example, if the average data spacing is 20 km, then it is impractical to consider response to waves  $< 40$  km in length. On the other hand, if data are not uniformly distributed, then phase changes and a higher "noise" level are inherent to the interpolated field. Hence, additional restrictions are required (Barnes, 1973).

In his earlier paper (Barnes, 1964), the weight function  $\eta = \exp(-r^2/4k)$  was chosen with

$$4k = R^2/E \quad (A6)$$

where  $E = 4$  and  $R$  is the "radius of influence" or simply "scan radius" beyond which an observation exerted zero influence in determining  $g(x,y)$ , see the dashed line in Fig. A3. With  $E = 4$ , we have repre-

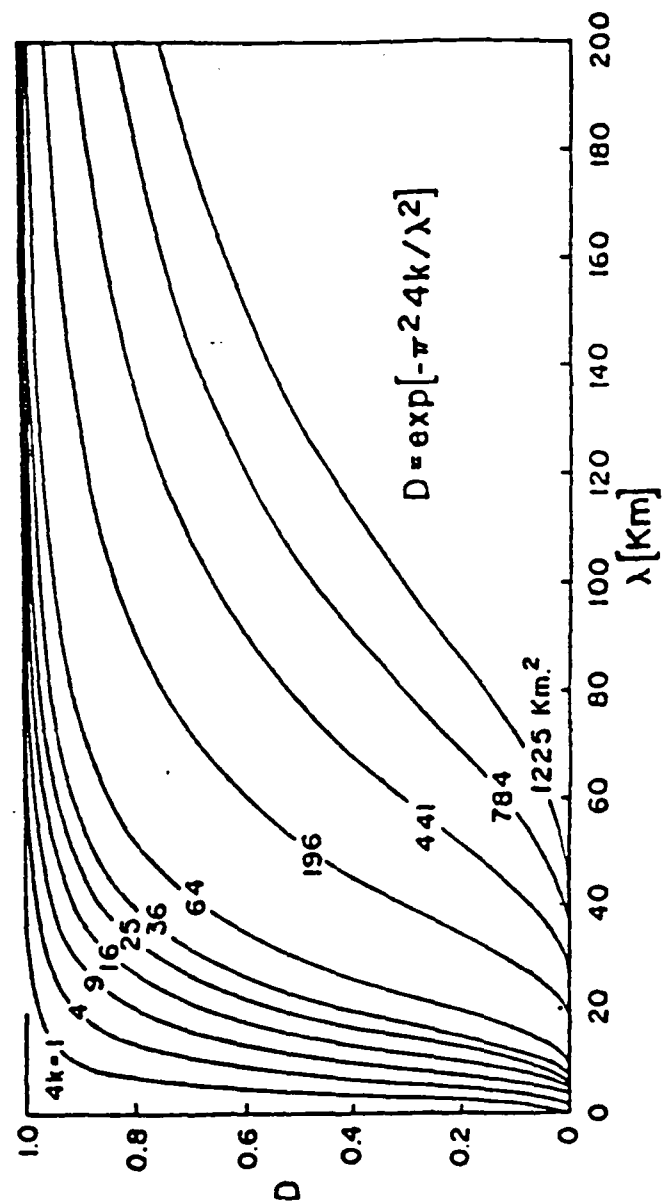


Fig. A2 Relationship of response function to wavelength  $\lambda$  for various choices of parameter  $K$  (after Barnes, 1973).



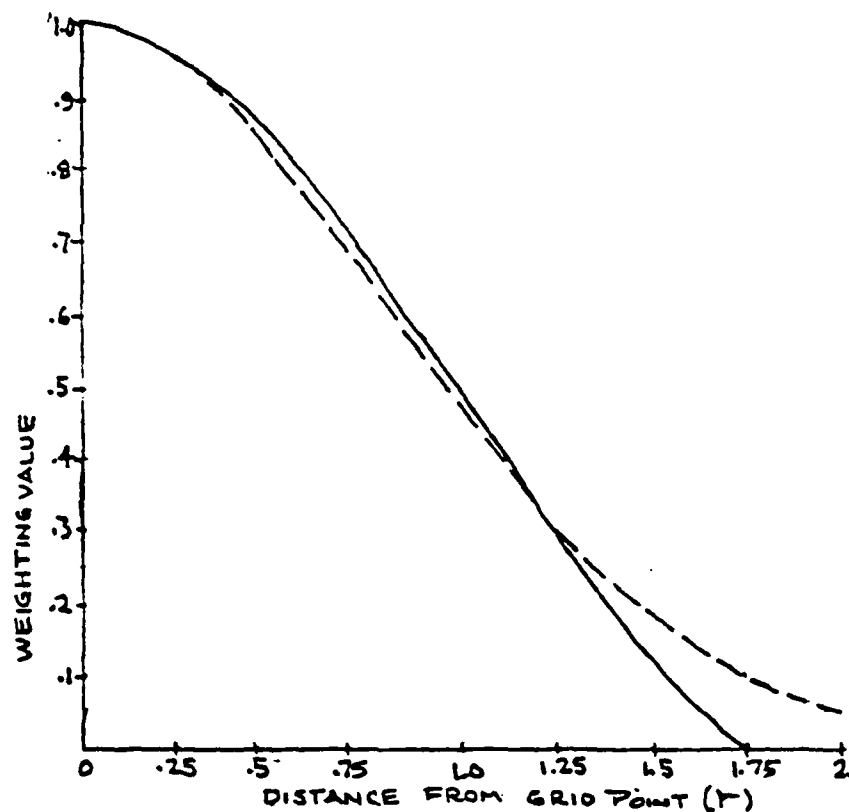


Fig. A3 Cressman weighting function (solid line) compared to first pass of Barnes weighting function (dashed line). For Cressman,  $R = 1.7$ , for Barnes  $R = 2.3$ . Crossover point is  $r=1.15$  with weight  $w = \exp(-1) = 0.363$ .

sented 98% of the influence of any datum within the circular region whose radius is  $R$ . With the aid of (A6), (A5) can also be written as

$$D(a,k) = e^{-\frac{R^2}{E}(\frac{\pi}{\lambda})^2} = e^{-\frac{\pi^2}{E}(R/\lambda)^2} \quad (A7)$$

The choice of  $R$  is critical and is closely related to the mean data spacing ( $d_m$ ). It is also a function of the observational errors and the nature of the data distribution (Stephens and Stitt, 1970). For the case of uniform data distribution, an optimum choice of  $R$  in relation to  $d_m$  is

$$1 < R/d_m < 2 \quad (A8)$$

Figure A4 illustrates some relationships between the initial response function  $D_0$  and wavelengths  $\lambda$  for various values of scan radius  $R$ .

### 3. Forcing Analysis to Fit Observed Data

In his earlier paper, Barnes (1964) developed a technique, a method of successive corrections, to fit the interpolated function,  $g(x,y)$ , to the observations within an arbitrarily small difference. Briefly, the technique employed successive applications of the same filter (weight function  $\eta$ ) to the residual differences between  $g(x,y)$  and  $f(x,y)$  on each of an arbitrary number of passes through the data. This technique was shown to be mathematically convergent which required only four passes (three iterations) to

# BARNES 1973 RESPONSE FUNCTION

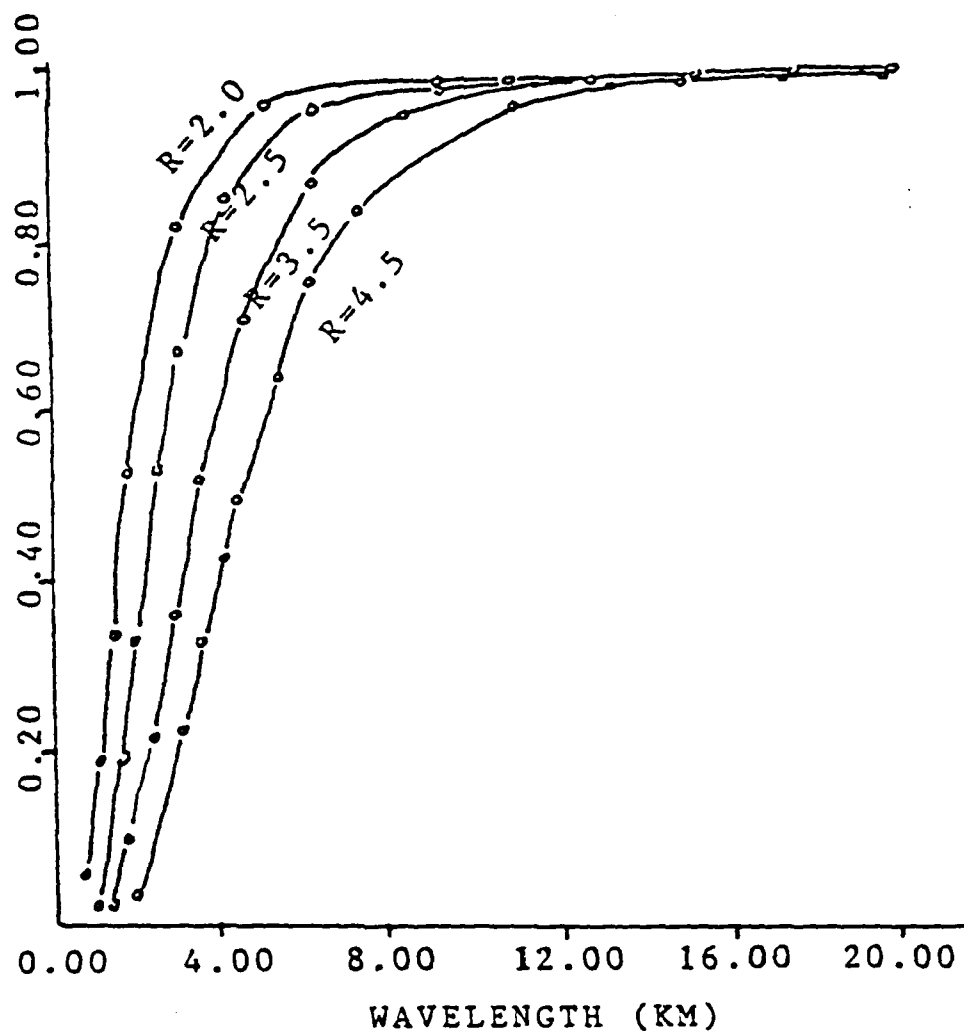


Fig. A4 Response curve for Barnes scheme (Eq. A5) for various values of R. Ordinate represents the percentage of original amplitude returned after gridding procedure.

force the interpolated field to agree with observations. The main drawback of the scheme was the large number of iterations required to achieve adequate response to short wavelengths which are not computationally economical. Later Barnes (1973) modified the scheme to require only one pass (iteration) through the data to achieve the desired response at the same wavelength. When only one pass through the data is made, the initial response  $D_\Delta$ , is

$$D_0 = e^{-4k_0 \left(\frac{\pi}{\lambda}\right)^2} \quad (A9)$$

The relationship between  $D_0$  and  $\lambda$  for various values of  $4k_0$  is shown in Fig. A2.

The interpolated field after the first pass at the grid point  $(i,j)$  is given by

$$g_0(i,j) = f(x,y)D_0 \quad (A10)$$

The subscript 0 denotes the first pass result through the data with weight function  $\eta = \exp(-r^2/4k_0)$ . The second pass (first iteration) then yields smoothed values of the residual differences between  $f(x,y)$  and  $g_0(x,y)$  which are added to the first pass field,  $g_0(i,j)$  to give:

$$g_1(i,j) = g_0(i,j) + [f(x,y) - g_0(x,y)]D_1 \quad (A11)$$

where

$$D_1 = \exp\left[-4k_1 \left(\frac{\pi}{\lambda}\right)^2\right] \quad (A12)$$

is the response resulting from application of the

AD-A170 673

DYNAMIC AND THERMODYNAMIC CHARACTERISTICS OF A  
MICROBURST-PRODUCING STORM. (U) AIR FORCE INST OF TECH  
WRIGHT-PATTERSON AFB OH R G HUGHES 1986

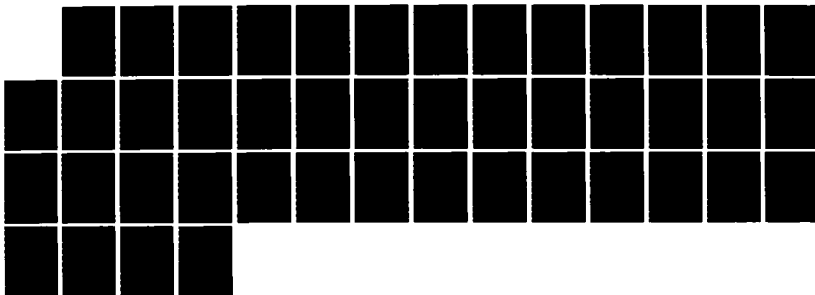
3/3

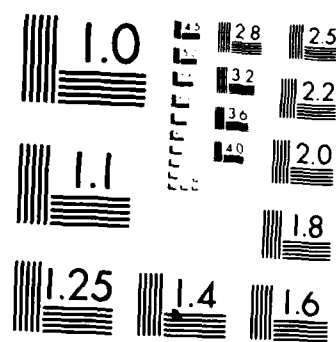
UNCLASSIFIED

AFIT/CI/NR-86-690

F/G 17/9

NL





MICROCOPY RESOLUTION TEST CHART  
NATIONAL BUREAU OF STANDARDS-1963-A

weight function

$$\eta_1 = \exp(-4k_1(\pi/\lambda)^2) \quad (\text{A13})$$

where  $k_1 = k_0 Y$  and  $0 < Y < 1$ .

Thus

$$D_1 = \exp([-4Yk_0(\pi/\lambda)^2]) = D_0^Y \quad (\text{A14})$$

Substituting (A10) and (A14) into (A11) yields

$$\begin{aligned} g_1(i,j) &= D_0 f(x,y) + [f(x,y) - D_0 f(x,y)] D_0^Y \\ &= f(x,y) [D_0 + D_0^Y - D_0 D^Y] \\ &= f(x,y) D_0 [1 + D_0^{Y-1} - D_0^Y] \\ &= f(x,y) D' \end{aligned} \quad (\text{A15})$$

where  $D' = D_0 (1 + D_0^{Y-1} - D_0^Y)$

$$D' = D_0 + (1 - D_0) D_1 \quad (\text{A16})$$

is the new response function indicating the proper measure of the degree of analysis convergence. In other words,  $D'$  represents how closely the interpolated values agree with the observed ones after a second pass (first iteration) through the data. The relationship between the initial response function,  $D_0$ , and the final response function,  $D'$ , for various  $\lambda$ , is shown in Fig. A5 and Table A1. Note that the curve  $Y = 1.0$  corresponds to the response after one iteration using the old technique, i.e.,

$$D_{OLD}^* = D_0 \sum_{n=0}^N (1 - D_0)^n \quad (\text{A17})$$

The new technique ( $k_1 = Y k_0$ ) with  $Y < 1$  recovers short wavelength amplitudes very quickly. According to Barnes (1973),  $Y$  cannot be smaller than 0.2 with-

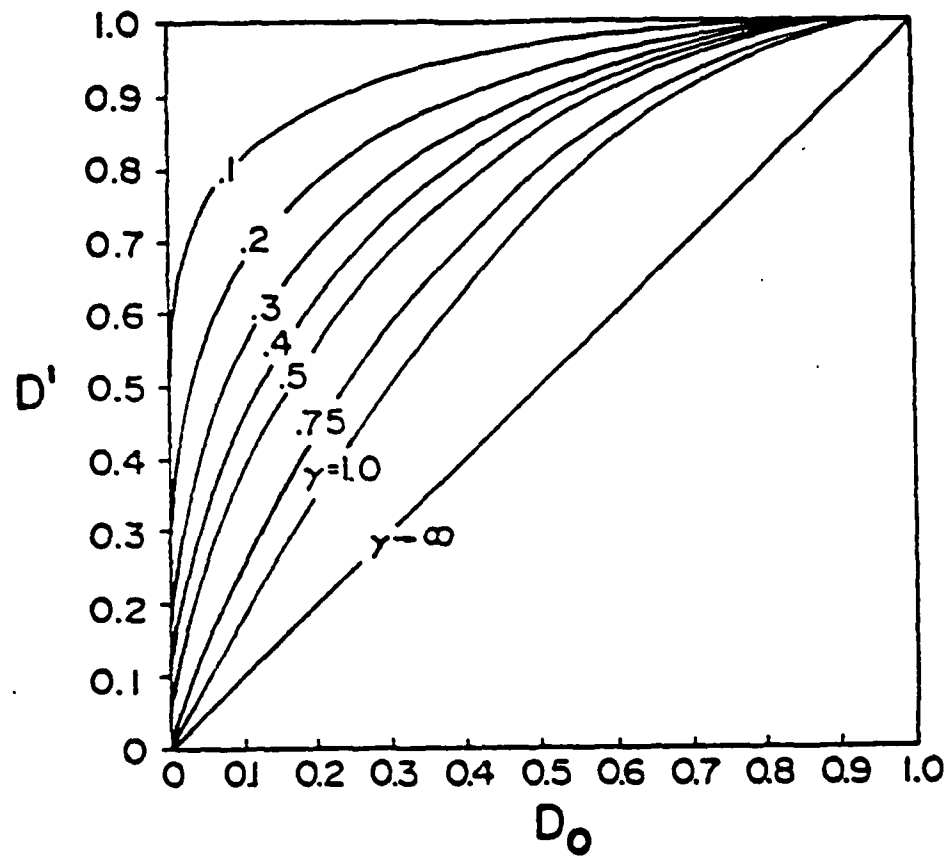


Fig. A5 Response  $D'$  after one correction pass as a function of initial response  $D_0$  and arbitrary parameter  $\gamma$  (after Barnes, 1973)



Table A1.

Relationship between $D_0$ and $D'$ for various values of $Y$ and $\lambda$ (km).													
$\lambda$	1.0	1.5	2.0	2.5	3.0	3.5	4.0	4.5	5.0	6.0	8.0	10.	20.
$D_0$	.00	.00	.02	.09	.18	.28	.38	.47	.54	.65	.79	.86	.93 .96
$Y=.2$													
$D'$	.05	.26	.47	.64	.76	.84	.89	.93	.95	.97	.99	.99	1.0
$Y=.3$													
$D'$	.01	.13	.33	.52	.67	.78	.85	.89	.92	.96	.99	.99	1.0
$Y=.4$													
$D'$	.00	.07	.23	.43	.59	.72	.80	.86	.90	.95	.98	.99	.99
$Y=.5$													
$D'$	.00	.03	.16	.35	.53	.67	.76	.83	.88	.93	.98	.99	.99
$Y=1.$													
$D'$	.00	.00	.04	.16	.33	.49	.62	.72	.78	.88	.95	.98	.99

out creating underflow checks on most computer systems. Further, if  $\gamma > .5$ , it does not produce rapid analysis convergence. An optimum value seems to be

$$0.2 < \gamma < 0.4 \quad (\text{A18})$$

as discussed in the study by Koch et al. (1983). From (A11), the actual correction pass value at each grid point is computed as the sum of the weighted averages from the two passes with  $M$  observations, i.e.,

$$g_1(i,j) = \frac{\sum_{m=1}^M \eta_{0m} f(x_m, y_m)}{\sum_{m=1}^M \eta_{0m}} + \frac{\sum_{m=1}^M \eta_{1m} [f(x_m, y_m) - g_0(x_m, y_m)]}{\sum_{m=1}^M \eta_{1m}} \quad (\text{A19})$$

If we let

$$\eta_{0m} = w_m^0; \quad \eta_{1m} = w_m^1$$

then (A19) can also be written as

$$g_1(i,j) = \frac{\sum_{m=1}^M w_m^0 f(x_m, y_m)}{\sum_{m=1}^M w_m^0} + \frac{\sum_{m=1}^M w_m^1 (f(x_m, y_m) - g_0(x_m, y_m))}{\sum_{m=1}^M w_m^1} \quad (\text{A19}')$$

where values of  $g_0(x_m, y_m)$  can be obtained by a simple bilinear interpolation between values of  $g_0(i, j)$  at the four surrounding grid points.

#### 4. Barnes' Scheme versus Cressman's Scheme

It is of interest to compare the scheme developed by Barnes (1973) with the Cressman (1959)

method for restoring short waves by successive scans with decreased influence radii. Cressman's weighting function,  $W_i$ , is given by

$$W_i = \begin{cases} \frac{R_o^2 - d_i^2}{R_o^2 + d_i^2} & \text{for } d_i \leq R_o \\ 0 & \text{for } d_i > R_o \end{cases} \quad (\text{A20})$$

where  $d$  is the distance from the grid point  $(i,j)$  to the observation at  $(x,y)$  and  $R_o$  is the scan radius. The scan radius  $R_o$  (or the length of the radius vector of influence) is generally equal to the horizontal and/or vertical grid spacing ( $\Delta$ ), i.e.,  $R_o/\Delta = 1$  (Wilson et al., 1984). Fig. A3 illustrates Cressman's weighting function  $W_i$  for  $R_o = 1.7$  km. For comparison, Barnes' weighting function,  $\eta$  (or  $W_m$ ), is also plotted using the scan radius  $R = 2.3$  km (dashed). Note that  $R_o \neq R$ . In this example, both curves have the same weighting  $e^{-1} (= .368)$  at the distance approximately 1.15 km. According to Barnes (1973), his scheme when compared to Cressman's scheme has the following four advantages:

- 1) Weight factor  $4k$  can be chosen prior to analysis so that pattern scales supportable by the data distribution will be revealed to known response amplitudes.
- 2) Because  $\eta$  approaches zero asymptotically, the influence of data can be extended any distance with-

out changing the weight function and, therefore, the response characteristics. In the Cressman technique, the weighting function shape is tied to the influence radius ( $R_o$ ) beyond which zero weight applies. To insure that sufficient data influence the interpolation in data sparse regions, the current scan radius is locally increased in some applications (Inman, 1970) until a minimum number of observations are included. Such a locally varying weight factor produces unknown response in the final results, and introduces small scale irregularities (noise) which must be smoothed by later application of arbitrary filters.

3) Small scale irregularities are adequately suppressed by this technique with the proper selection of scan radius ( $R$ ). Once the value of  $R$  is chosen, there is no need to change it during the iteration process.

4) The desired pattern resolution can be achieved in only one iteration, instead of four or more required with Cressman's technique, thus effecting a modest savings in computer time.

An objective analysis scheme based on the Barnes (1973) technique and designed for use on an interactive computer was developed by Koch et al. (1983). In the paper, a comparison between the Barnes and

Cressman objective analysis schemes was discussed. Since the Cressman weight does not asymptotically approach zero with increasing distance as it does in the Barnes technique (see Fig. A3), it can cause serious difficulties when the data distribution is non-uniform. Classical sampling theory suggests that waves with  $\lambda < 2d_m$  (or  $2\Delta n$ ) cannot be resolved properly since five data points are required to describe the wave and its derivatives. Both Cressman and Barnes techniques employ the method of successive corrections. Thus, an adjustment is made to the first pass analysis by decreasing the scan radius in the second pass through the data to recover the amplitude of short waves with wavelength  $\lambda > 2d_m$  which was suppressed during the first pass due to filtering. In the Cressman case, neither the number of additional passes (4-6) nor the value of the scan radius at the second pass are governed explicitly by the data distance; thus, neither is the filter response. Stephens and Stitt (1970) developed a method of selecting optimum influence radii for the objective analysis of a scalar field using the method of successive corrections. They used Cressman's weighting function to perform various experiments. Results showed that for an ensemble of randomly distributed station arrays, the optimum influence radius

occurs at  $R_o/d_m \approx 1.6$ . However, the optimum influence radius increases with data separation, observational error, and wavelength of the true field for the average taken as the guess field. For a uniform data distribution, an optimum choice for the Cressman influence radius on the first pass can be made in terms of  $d_m$ . However, the optimum influence radius is not well known theoretically on additional passes, so the final filter response is rather arbitrary.

Unlike Cressman weighting, the Barnes filter response characteristics can be determined prior to the analysis so that pattern scales resolvable by the data distribution may be revealed to a great extent. According to Koch et al. (1983), non-uniform data distributions must be carefully dealt with. The average distance between each of the observations to its nearest neighbor,  $\Delta r_c$ , determines the maximum detail permitted in the objective analysis. Once the data spacing ( $\Delta n$ ) is determined, i.e.  $\Delta n > \Delta r_c$ , the value should be properly selected. This quantity determines the degree of convergence of the interpolated field towards the observed field. As previously mentioned (see Fig. A5), the maximum detail is obtainable with  $Y = 0.2$ , while the least detail results with  $Y = 1.0$ . The small value of  $Y$  (say  $Y \approx 0.2$ ) can only be used when observations have

large values of signal to noise ratio (SNR) and are not substantially contaminated by subgrid-scale atmospheric processes. In addition, the spatial data distribution must be rather uniform. For the purposes of Doppler studies, we found that most data have a high enough signal to noise ratio so that can be chosen between 0.2 and 0.4. Figure A6 presents the relationship between the response function and wavelength for  $\gamma = 0.3$  and  $R = 2.5$  km. The solid curve represents the initial response ( $D_0$ ), while the dashed curve denotes the final response ( $D'$ ). For comparison, the response curve  $D_0^\gamma$  is also plotted (dotted curve). It is seen that amplitudes of shorter waves which were suppressed during the first pass are recovered substantially after one iteration (second pass). For example at  $\lambda = 3$  km,  $D_0 = 0.18$  and  $D' = 0.67$  which implies that for the wave with wavelength  $\lambda = 3$  km, about 67% of its original amplitude will be retained after only one correction. On the other hand, if no correction is made then only  $\sim 18\%$  of its original amplitude will be kept and the remaining 82% will be lost due to filtering.

From Table A1, it is seen that as the size (scale) of waves increases, say  $\lambda \geq 5$  km, then more than 90% of their original amplitudes will be represented in the final analysis field. It will be shown

later that our final response curve ( $D'$ ) is in good agreement with the response curve of Testud and Chong (1983) for Analysis B (see their Fig. 2). Inspection of Fig. A6 further reveals that the wavelengths of the minimum resolvable wave for the scan radius of  $R = 2.5$  km is about 2 to 2.5 km depending on the definition of a cut-off wavelength. Testud and Chong (1983) determined the cut-off wavelength based on the amplitude gain factor:  $G = 0.5$ , corresponding to the response  $D' = 0.5$  in our example. On the other hand, Koch et al. (1983) used  $D' = e^{-1}$  ( $= 0.378$ ) to determine the minimum resolvable wavelengths ( $2\Delta n$ ) in terms of known data spacing  $\Delta n$ . Consider  $\gamma = 0.2$ , they arrived at the formula relating the weighting factor  $4k_0$  to the minimum resolvable wavelength  $2\Delta n$ , i.e.,

$$4k_0 = 5.052 \left( \frac{2\Delta n}{\pi} \right)^2 \quad (\text{A21})$$

It implies that the weight parameter  $4k_0$  is fixed by the data spacing ( $\Delta n$ ) to give maximum response of no more than  $e^{-1}$  at the  $2\Delta n$  wavelengths. The above relationship will be slightly changed if a different value of  $\gamma$  is used. If we rewrite A(21) as

$$4k_0 = \frac{R^2}{E} = C_\gamma \left( \frac{2\Delta n}{\pi} \right)^2 \quad (\text{A22})$$

where  $C_\gamma = 3.052$  for  $\gamma = 0.2$ . Note that values of  $C$  become smaller if larger values of  $\gamma$  are used.

It follows that



# BARNES 1973 RESPONSE FUNCTION

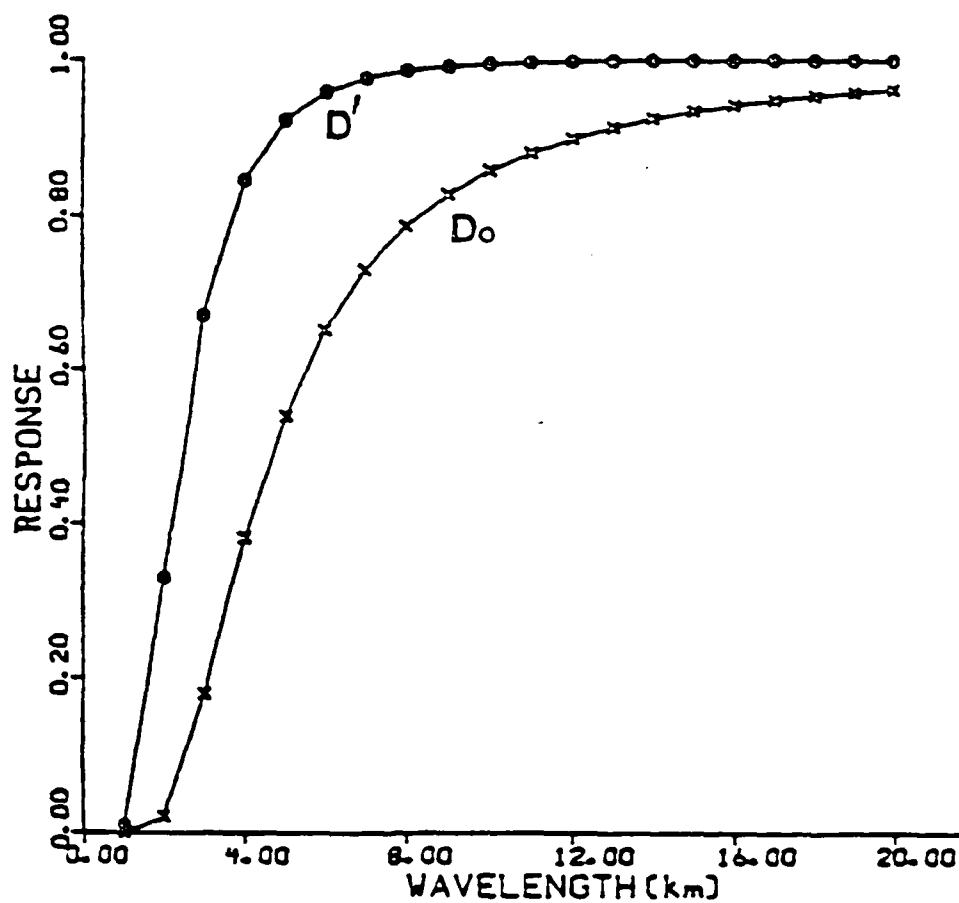


Fig. A6 Response functions  $D_0$  and  $D'$  versus the wavelength  $\lambda$  in km.

$$R = \left(\frac{4}{\pi} \sqrt{C_Y}\right) \Delta n \quad \text{or} \quad R/\Delta n = \frac{4}{\pi} \sqrt{C_Y} = 2.87 \quad (\text{A22a})$$

When  $Y = 0.3$ , our calculation indicates that  $C_Y = 3.503$  and

$$R/\Delta n \approx 2.4 \quad (\text{A22b})$$

which suggests that the selection of an optimum scan radius is closely related to the mean data spacing  $\Delta n$  (or  $d_m$ ). If  $\Delta n = 1$  km, then  $R$  should be chosen to be  $\approx 2.4$  km. On the other hand, if the cut-off wavelength is chosen at  $G(D') = 0.5$ , then the relation (A22b) becomes  $R/\Delta n \approx 2.0$ .

Once the mean data spacing is known, the choice of grid size ( $\Delta$ ) can be properly made. Since five grid points are required to represent a typical wave on a grid, and the minimum resolvable wave is of  $\lambda = 2\Delta n$ , then  $\Delta$  must be no longer than one-half of  $\Delta n$  to guarantee proper representation of resolvable wavelengths. As for the lower limit, the ratio  $\Delta/\Delta n$  should be less than  $1/3$  to avoid noisy derivative fields in velocity, e.g., vorticity and divergence fields. Koch et al. (1983) suggested that

$$1/3 < \Delta/\Delta n < 1/2 \quad (\text{A23})$$

for their interactive Barnes scheme.

##### 5. Objective Analysis Scheme Based on Principles of Calculus of Variation

Testud and Chong (1983) proposed a method based on the principles of numerical variational analysis

(Sasaki, 1970) to filter and interpolate the "raw" data in radial velocity. This step is necessary in order to reduce the noise due to radar statistical errors and to cut off turbulent motions with scales smaller than the data resolution.

We wish to find the filtered function  $M^0(s, l)$  which is the best fit, in the least-squares sense, to the data set  $\{M_k\}$ . Here  $s = x$  and  $l = \sqrt{y^2 + z^2}$  in the Coplane coordinates. Since  $M^0$  is continuous and differentiable up to the second order, the integral

$$J(M^0) = \frac{1}{S} \iint_{\text{AREA}} \left( \left( \frac{\partial M^0}{\partial s} \right)^2 + \left( \frac{\partial M^0}{\partial l} \right)^2 \right) ds dl \quad (\text{A24})$$

is bounded. Here  $S$  denotes the surface of the domain being considered. We want to minimize the error between functions  $M^0(s, l)$  and  $M_k$  such that

$$E = \frac{1}{N} \sum_{k=1}^N (M^0(s_k, l_k) - M_k)^2 \quad (\text{A25})$$

which satisfies the condition

$$J_1(M^0) = C_1 \quad (\text{A26})$$

with  $C_1$  positive real.

The classical problem in calculus of variation can be solved by considering the minimization of the function  $F$  in the form

$$F = \frac{1}{S} \iint_{\text{AREA}} (M^0 - M) ds dl + \mu_1 J_1(M^0) \quad (\text{A27})$$

where  $\mu_1$  is a predetermined value. The Euler's equation associated with (A27) is

$$M^0 - M - \mu_1 \Delta M = 0 \quad (\text{A28})$$

In Fourier space (A28) becomes

$$M_K^0 = \frac{M_K}{1 + \mu |\vec{K}|^2} \quad (A29)$$

where  $K^2$  is the wave vector, and  $M_K^0$ ,  $M_K$  denote the Fourier component of  $M^0$  and  $M$ , respectively. Thus  $J_1(M^0)$  acts as a low-pass filter which has the property of isotropy (since the amplitude gain only depends on wave number  $|\vec{K}|$ ). Further, the parameter controls the "cut-off wave number"  $|\vec{K}| = 1/\sqrt{\mu}$  or wavelength  $\lambda_0 = \frac{2\pi}{|\vec{K}_0|}$  for which the amplitude gain ( $G = A_{out}/A_{in}$ ) is 0.5 corresponding to 50% response in the Barnes scheme discussed previously.

For the same reasons, the above relationship can also be applied to functionals  $J_n$  using higher order derivatives, i.e.,

$$J_n(M^0) = \frac{1}{S} \iint_{\text{AREA}} \sum_{p=0}^n \frac{n!}{p!(n-p)!} \left( \frac{\partial^p \left( \frac{\partial(M^0)}{\partial \ell^{n-p}} \right)}{\partial s^p} \right)^2 ds d\ell \quad (A30)$$

From Eq.(A29) it follows that the amplitude gain  $G$  corresponding to such functionals can be written as

$$G = \frac{M_K^0}{M_K} = \frac{1}{1 + \mu K^2} \quad (A31)$$

The higher the order  $n$ , the steeper is the slope of the gain curve around the cut-off wavenumber  $|\vec{K}_0| = \mu^{-1/2n}$ . Only the first ( $n = 1$ ) and second ( $n = 2$ ) order functionals,  $J_1(M^0)$  and  $J_2(M^0)$ , are considered.  $J_1(M^0)$  is given in (24) and  $J_2(M^0)$  has the form

$$J_2(M^0) = \frac{1}{S} \iint_{\text{AREA}} \left[ \left( \frac{\partial^2 M^0}{\partial s^2} \right)^2 + 2 \left( \frac{\partial^2 M^0}{\partial s \partial \ell} \right) + \left( \frac{\partial^2 M^0}{\partial \ell^2} \right) \right] ds d\ell \quad (\text{A32})$$

Four numerical experiments were performed by Testud and Chong (1983). The first three experiments (Analysis A, B, and C) are presented below:

Analysis A - Variational Analysis with  $J_1$ .

Consider the first order functional  $J_1(M^0)$  with  $\mu_1 = 0.405(\text{km})$ , corresponding to a cut-off wavelength  $\lambda_0 = 4 \text{ km}$ . The filtered values  $M_{ij}^0$  are calculated from the matrix equation, see their Eq.(17).

Analysis B - Variational Analysis with  $J_2$

As in Analysis A except that  $J_1(M^0)$  is replaced by  $J_2(M^0)$ , the second order functional. To assure the cut-off wavelength  $\lambda_0 = 4.0 \text{ km}$ ,  $\mu$  is chosen to be  $0.164 \text{ km}$ .

Analysis C - Cressman's Filtering

Gridded values of  $M_{ij}^0$  are calculated based on Cressman's Weight inside a circle with a scan radius  $R_0 = 1.7 \text{ km}$ . The value of  $R_0$  chosen gives the same "cut-off wavelength"  $\lambda_0 = 4.0 \text{ km}$  as in A and B.

The filtering characteristics under experiments A, B, and C are presented in Fig. A7. It represents the amplitude gain factor  $G$ , defined as the ratio of wave amplitude at output to wave amplitude at input, as a function of the wavelength. Curves A and B are found to be very close to the theoretical gain curves

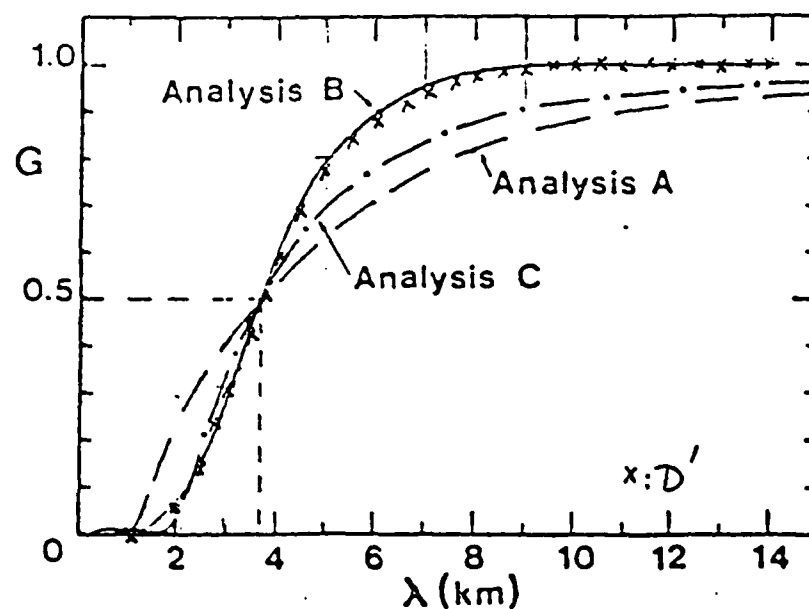


Fig. A7 Amplitude gain  $G$  of the filtering as a function of the wavelength  $\lambda$ . Curve A variational analysis with functional  $J_1$ ; curve B variational analysis with functional  $J_2$ ; Curve C filtering using the Cressman weighting function. The response curve  $D'$  obtained from Barnes (1973) scheme with  $\gamma=0.3$  and  $R=3.6$  km is denoted by the symbol  $x$ .

derived from the Euler equation, i.e.,

$$G_A(\lambda) = \frac{1}{1 + 4\pi^2 \mu_1 / \lambda^2} ; \quad G_B = \frac{1}{1 + 16\pi^4 \mu_2 / \lambda^4} \quad (A33)$$

Table A2 presents values of  $G$  obtained from (A33). These values are in good agreement with curves A and B shown in Fig. A7. It is apparent that, Analysis B appears to be better than Analyses A and C. It provides a sharper cut-off around  $\lambda_0 = 3.6$  km. Further, it completely suppresses subgrid scale motions, and yet retains the amplitudes ( $G > 0.95$ ) for motions with wavelengths  $> 7$  km. Analysis C appears to perform better than Analysis A, but worse than Analysis B. For comparison, the response function  $D'$  which produces a cut-off wavelength at  $\lambda_0 = 4$  km ( $\gamma = 0.3$  and  $R_0 = 4$  km) is also produced in Fig. A8 using the symbol  $x$ . It is evident that the agreement between the  $D'$  curve and the B curve is remarkable.

It is of interest to compare the response curve presented in Fig. A6, based on the Barnes (1973) scheme with  $\gamma = 0.3$  and  $R_0 = 2.5$  km, to the results obtained by Testud and Chong (1983), see Fig. A7. In order to make the comparison meaningful, the cut-off wavelength  $\lambda_0$  as revealed in Fig. A6 is now chosen to be about 2.5 km. Since (33) can produce the curves very comparable to those presented in Fig. A7 (Testud

Table A2.

The amplitude gain function,  $G$ , based on the theoretical formulas derived by Testud and Chong (1983).  $G_1$  is the amplitude gain for  $n = 1$  (first order) and  $G_2$  is for  $n = 2$  (second order). The cut-off wavelength (where  $G = 0.5$ ),  $\lambda_c$ , is 4 km.

$\lambda$ (km) =	0	2	4	6	8	10	15	20
Analysis A : $G_1$	0	0.200	0.500	0.690	0.800	0.860	0.935	0.962
Analysis B : $G_2$	0	0.060	0.500	0.836	0.942	0.975	0.995	0.999

$$G_1(\lambda) = \frac{1}{1 + 4\pi^2 \mu_1 / \lambda^2} ; \mu_1 = 0.405 \text{ km}$$

$$G_2(\lambda) = \frac{1}{1 + 16\pi^4 \mu_2 / \lambda^4} ; \mu_2 = 0.164$$



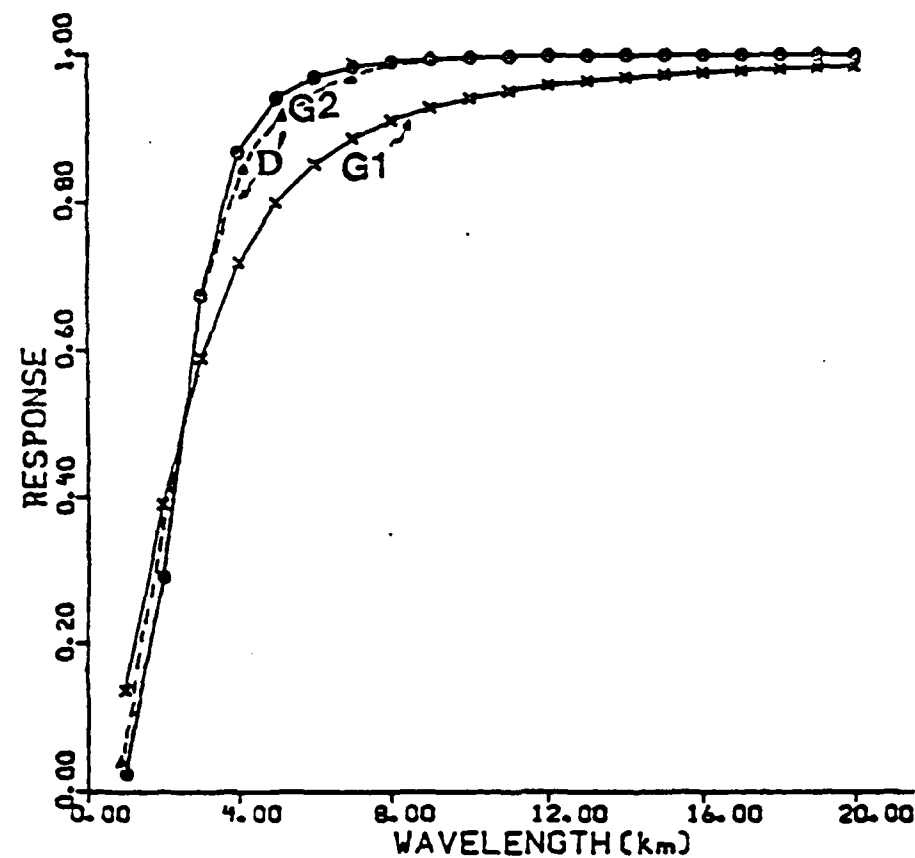


Fig. A8 Comparison of response curves obtained from Barnes (1973) scheme (D') with  $\gamma=0.3$  and  $R=2.5$  km and theoretical formulas derived by Testud and Chong (1983) for  $n=1$  (G1) and  $n=2$  (G2).

and Chong, 1983), we decided to use (A33) to calculate values of amplitude gain. In order to produce the "cut-off wavelength" at  $\lambda_0 = 2.5$  kr, values of  $\mu_1 = 0.1583$  km and  $\mu_2 = 0.0251$  km are chosen. Results for  $G_1$  and  $G_2$  are given in Table A3. For comparison, values for  $D'$  at corresponding wavelengths are also shown. It is clear that  $G_2$  is in very good agreement with  $D'$  although the results were obtained from two totally different, independent methods. These results are depicted in Fig. A8 for illustration.

#### 6. Concluding Remarks

The Barnes (1973) objective analysis scheme is shown to be a very effective method in reducing meteorological data. Although, the method has been primarily applied to the data collected under the conventional observational network, i.e., upper air and surface data, it can also be applied to non-conventional data sets, e.g., satellite and Doppler radar data. The advantages of the Barnes scheme over the Cressman scheme in obtaining the interpolated field with successive corrections are apparent. It allows the user to select a proper scan radius based on the consideration of the data distribution, the observational errors, etc., prior to the analysis.

Table A3

Computed values for G1 and G2 from the theoretical formulas derived by Testud and Chong (1983). Values of  $\lambda$ , and  $\lambda_{22}$  are 0.1584 km and 0.0251 km, respectively. For comparison, values of D' obtained from the Barnes (1973) scheme with  $\gamma = 0.3$  and  $R = 2.5$  are also listed. G1 is from Analysis A and G2 is from Analysis B.

	$\lambda =$	0.0	1.0	2.0	3.0	4.0	5.0	6.0	7.0	8.0	10.	15.	20.
D'		.00	.01	.33	.67	.84	.92	.96	.98	.99	.99	.99	.99
G1		.00	.14	.39	.59	.72	.80	.85	.89	.91	.94	.97	.99
G2		.00	.03	.29	.67	.87	.94	.97	.98	.99	.99	.99	.99

Accordingly, the information of resolvable waves can be preserved, while the unresolvable waves (noise) will be properly filtered. Thus, it appears to be a useful tool for Doppler studies.

## APPENDIX B: Correction of 3D Wind Field

### 1) Anelastic Constraint

The term "anelastic continuity" used throughout this study states essentially that density is a function of height only, or

$$\nabla_3 \cdot \rho \vec{V}_3 = \rho \frac{\partial u}{\partial x} + \rho \frac{\partial v}{\partial y} + \frac{\partial(\rho w)}{\partial z} \quad (B1)$$

The wind field derived using the Armijo (1969) equations contain both real and erroneous information. The vertical velocity which has been derived by downward integration of the anelastic continuity equation using these winds contains error as well. This 3D wind field is, however, in anelastic balance. The object of the correction scheme is threefold.

- 1) To adjust the wind field so that the constraint that the "true" vertical velocity at the surface is zero.
- 2) To adjust the wind field so the resultant wind field is still in anelastic balance.
- 3) The adjustment of the wind field be kept to a minimum in order to preserve as much of the "true" features as possible.

### 2. Euler-Lagrange Equations

Assuming that some weighting functions  $\alpha^2$  and  $\beta^2$  are available which reflect some measure of confidence

in the observed values of horizontal wind components. It is desirable to minimize the weighted square velocity error over the horizontal domain with the anelastic continuity equation acting to constrain the correction, i.e.,

$$J = \int_{z_1}^0 \int_{-Y}^Y \int_{-X}^X [\alpha^2(u - \hat{u})^2 + \beta^2(v - \hat{v})^2 + \lambda \nabla_3 \rho_0 \vec{W}_3] dx dy dz \quad (B2)$$

where

$\alpha^2, \beta^2$  are confidence weights for  $u$  and  $v$ , respectively,

$u, v$  are corrected (adjusted) horizontal wind components,

$\hat{u}, \hat{v}$  are observed horizontal wind components,

and

$\lambda$  is Lagrange multiplier.

The minimum (stationary) value of  $B2$  can be determined by applying the variational operator  $\delta$ . The result is referred to as the Euler-Lagrange differential equation.

$$\frac{\partial}{\partial x_j} \left( \frac{\partial I}{\partial \left( \frac{\partial u_i}{\partial x_j} \right)} \right) + \frac{\partial I}{\partial u_i} = 0 \quad (B3)$$

where

$I$  = integrand in Eq (B2)

$u_i$  =  $u$  for  $i=1$ ,  $v$  for  $i=2$ , and

$x_j$  =  $x$  for  $j=1$ ,  $y$  for  $j=2$ .

### 3. Proof of Existence of Euler-Lagrange Differential Equation

The motion of a particle in a conservative field of forces satisfies both Newton's laws of motion and the Lagrangian equations. There is still another relationship which is satisfied by the motion.

Consider a given function  $F(x, y, y')$  which we assume can be expanded in a Taylor series in an interval  $x_1 < x < x_2$ ; where  $x_1 < x_2$ . The problem we shall consider is:

What function  $y(x)$  will cause the integral (or functional)

$$J = \int_{x_1}^{x_2} F(x, y, y') dx \quad (B4)$$

to have a stationary value?

We shall use the method of calculus of variations, in which we consider neighboring functions

$$y(x) + \xi \eta(x) = F$$

with boundary conditon

$$\eta(x_1) = \eta(x_2) = 0 \quad (B5)$$

where  $\eta(x)$  is an arbitrary function of  $x$  and  $\xi$  is an arbitrarily small quantity. By letting  $\xi$  approach zero, the neighboring function can be made to approach the true function. Figure B.1 illustrates this concept. The problem may now be restated:

What conditions are necessary to cause the integral

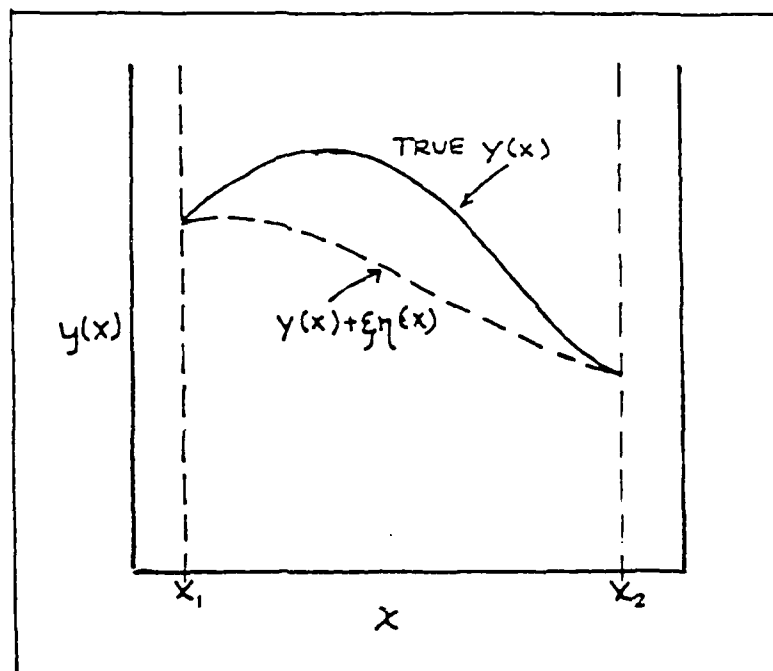


Fig. B1 Relationship between "true" functional solution and neighboring function for method of calculus of variation.



(or functional)

$$J = \int_{x_1}^{x_2} F(x, y + \xi \eta, y' + \xi \eta') dx \quad (B6)$$

to have a stationary value as  $\xi$  approaches zero, i.e.,

$$\left. \frac{dJ}{d\xi} \right|_{\xi=0} = 0 \quad (B7)$$

The Taylor series expansion for a function of three variables is

$$F(x+h, y+k, z+l) = F(x, y, z) + \left( h \frac{\partial F}{\partial x} + k \frac{\partial F}{\partial y} + l \frac{\partial F}{\partial z} \right) + \dots + \frac{1}{n!} \left( h^n \frac{\partial^n F}{\partial x^n} + k^n \frac{\partial^n F}{\partial y^n} + l^n \frac{\partial^n F}{\partial z^n} \right) \quad (B8)$$

where for  $n = 2$ , we have  $\frac{1}{2!} \left( h^2 \frac{\partial^2 F}{\partial x^2} + k^2 \frac{\partial^2 F}{\partial y^2} + l^2 \frac{\partial^2 F}{\partial z^2} \right)$

The Taylor series expansion of (B6) is therefore obtained by letting  $k = \xi \eta$  and  $l = \xi \eta'$ , yields

$$J = \int_{x_1}^{x_2} \left( F(x, y, y') + \xi \left( \eta \frac{\partial F}{\partial y} + \eta' \frac{\partial F}{\partial y'} \right) + \xi^2 \left( \dots \right) + \dots \right) dx \quad (B9)$$

when (B9) is differentiated with respect to  $\xi$  under the integral, this assumes that  $\xi$  is not a function of  $x$ , the results are

$$\frac{dJ}{d\xi} = \int_{x_1}^{x_2} \left( \eta \frac{\partial F}{\partial y} + \eta' \frac{\partial F}{\partial y'} + 2\xi \left( \dots \right) + \dots \right) dx \quad (B10)$$

Now allow  $\xi \rightarrow 0$ , so that we see

$$\left. \frac{dJ}{d\xi} \right|_{\xi=0} = \int_{x_1}^{x_2} \left( \eta \frac{\partial F}{\partial y} + \eta' \frac{\partial F}{\partial y'} \right) dx \quad (B11)$$

With the aid of the method of integration by parts, one obtains

$$\left. \frac{dJ}{d\xi} \right|_{\xi=0} = \int_{x_1}^{x_2} \eta \left( \frac{\partial F}{\partial y} - \frac{d}{dx} \left( \frac{\partial F}{\partial y'} \right) \right) dx + \eta \frac{\partial F}{\partial y} \Big|_{x_1}^{x_2} \quad (B12)$$

We note that the last portion of (B12) reduces to zero due to the boundary conditions we imposed in (B5).

The integral of (B12) is zero for the arbitrary function  $F(x)$  only if the integrand is zero, hence

$$\frac{d}{dx} \left( \frac{\partial F}{\partial y'} \right) - \frac{\partial F}{\partial y} = 0 \quad (B13)$$

which is called the Euler - Lagrange differential equation. The function  $y(x)$  which satisfies (B13) will cause the integral of (B4) to have a stationary value.

The resultant Euler-Lagrange equations for our particular problem are

$$u - \hat{u} = \frac{\bar{p}(z)}{2\alpha^2} \frac{\partial x}{\partial x} \quad (B14)$$

$$v - \hat{v} = \frac{\bar{p}(z)}{2\beta^2} \frac{\partial \lambda}{\partial u} \quad (B15)$$

and

$$\int_{z_T}^0 (\nabla_3 \cdot \bar{\rho}(z) \bar{\nabla}) dz = 0 \quad (B16)$$

The errors in the observed wind field cause errors in the divergence field. This error can be expressed as

$$\bar{\rho} D_E = \bar{\rho} (D - \hat{D}) \quad (B17)$$

where

$\bar{\rho} D$  is "true" mass divergence,

$\bar{\rho} \hat{D}$  is observed mass divergence, and

$\bar{\rho} (D - \hat{D})$  is mass divergence error.

Integrating (B17) from the storm top to the surface yields

$$\int_{z_T}^0 \bar{\rho} D_E dz = \int_{z_T}^0 \bar{\rho} D dz - \int_{z_T}^0 \bar{\rho} \hat{D} dz \quad (B18)$$

But from the Integral constraint equation (B16)

one obtains

$$W_{z_T} = \hat{W}_{z_T} = W_0 = 0 \quad (B19)$$

It follows:

$$\int_{z_T}^0 \bar{\rho} D dz = 0 \quad (B20)$$

Since the integral of the adjusted mass divergence must vanish we are left with

$$\int_{z_T}^0 \bar{\rho} D_E dz = - \int_{z_T}^0 \bar{\rho} \hat{D} dz \quad (B21)$$

With the aid of the anelastic continuity equation and the kinematic boundary conditions, it follows that

$$\int_{z_T}^0 \bar{\rho} D_E dz = (\bar{\rho} \hat{W}_0) \quad (B22)$$

Forcing the true vertical velocity to vanish at the storm top and at the surface is the basis for correcting the observed wind fields and hence the divergence fields. Differentiating (B14) with respect to  $x$  and (B15) with respect to  $y$  and add, yields

$$D_e(x, y, z) = \frac{\partial \left( \frac{\bar{p}}{2\alpha^2} \frac{\partial \lambda}{\partial x} \right)}{\partial x} + \frac{\partial \left( \frac{\bar{p}}{2\beta^2} \frac{\partial \lambda}{\partial y} \right)}{\partial y} \quad (\text{B23})$$

In the above,  $D_e$  represents the vertically integrated divergence errors accumulated during the downward integration process. Since we do not know the vertical distribution of  $D_e$  well, it is assumed to be independent of height. This assumption, however, insures that the corrected  $w$  does meet both the upper and lower kinematic boundary conditions. Further, the variationally adjusted three Cartesian wind components ( $u$ ,  $v$ ,  $w$ ) satisfy the anelastic continuity equation everywhere within the domain being considered. It further requires that the Lagrangian multiplier  $\lambda$  must be independent of height. It follows that the analysis equations have the form:

$$u = \hat{u} + \frac{\bar{p} \sigma_u^2}{2} \frac{\partial \lambda}{\partial x} \quad (\text{B24})$$

$$v = \hat{v} + \frac{\bar{p} \sigma_v^2}{2} \frac{\partial \lambda}{\partial y} \quad (\text{B25}).$$

Once the correction to the horizontal wind field is made, the vertical wind component can be recomputed using the previously described technique of downward

integration with the corrected horizontal wind field  
used to compute divergence elements.

# APPENDIX C: Computation of Correction Weighting Functions

The computation of the weighting functions  $\alpha^2$  and  $\beta^2$  used in the adjustment scheme follows that suggested by Ray et al. (1980) and Wilson et al. (1984). We begin by applying the Armijo (1969) equations for the solution of horizontal wind to the standard deviations

$$\sigma_u^2 = \frac{R_1^2 \Delta Y_2^2 \sigma_v^2 - R_2^2 \Delta Y_1^2 \sigma_v^2 + (\Delta Y_1 \Delta z_2 - \Delta z_1 \Delta Y_2)}{(\Delta x_1 \Delta Y_2 - \Delta Y_1 \Delta x_2)^2} + \text{cov}(u, w) \quad (C1)$$

$$\sigma_v^2 = \frac{R_1^2 \Delta x_2^2 \sigma_u^2 - R_2^2 \Delta x_1^2 \sigma_u^2 + (\Delta x_1 \Delta z_2 - \Delta z_1 \Delta x_2)}{(\Delta x_2 \Delta Y_1 - \Delta Y_2 \Delta x_1)^2} + \text{cov}(v, w) \quad (C2).$$

Wilson et al. (1984) noted that the covariance terms are small compared to contributions by the other terms and were therefore neglected in the computation. To solve the above equations, it was necessary to add a third equation to close the problem. A form of the anelastic continuity equation was added as the third equation.

$$\nabla_3 \cdot \sigma = 0 \quad (C3)$$

This equation was integrated downward in exactly the same manner used to solve for the wind components. The boundary condition,  $\sigma_w = 0$  at the storm top, was

assumed. The values of  $\sigma_{V_1}$  and  $\sigma_{V_2}$  were assumed to be unity throughout the 3-dimensional domain. At first glance, this may seem unfounded. The following test was performed to ascertain how reliable this assumption was. At selected grid locations, the edited radial observations, which were being used by the Barnes gridding procedure, were collected and an unweighted standard deviation was computed from the radial wind component from each radar. The radius of influence used was 1.25 km. While means were understandably different, these radial standard deviations were remarkably well behaved and clustered in value near unity. Recognizing that the selection of the scan radius will have great influence upon the outcome of this test, the use of unity was not considered totally unfounded. Wirsing (1985) suggested that the actual magnitude of the weighting function is of less importance than performing the correction with any weighting function and suggested that perhaps a value of unity could be used (private communication) and still produce credible results.

This technique has the appeal of having computed the weights in the same manner as computing the winds. There are two primary criticisms. First, it seems to some extent to suggest the reliability of the "derived" wind is more a function of position than

reliance on the what the radar "saw". The resultant field increases as you move away from the radars. This would seem reasonable as the volume used to compute the gate information increases as you move away from the radar. Secondly, a correction to account for "integrated divergence error" is not performed. This has the tendency to over correct the results near the surface the weights will not only contain "real" weight but also "computational" weight.



## BIBLIOGRAPHY

- Armijo, L., 1969: A theory for the determination of wind and precipitation velocities with Doppler radars. J. Atmos. Sci., 26, 566-569.
- Atlas, D., and R. Wexler, 1965: Wind measurements by conventional radar with a dual beam pattern. J. Appl. Meteor., 4, 598-606.
- Barnes, S.L., 1964: A technique for maximizing details in numerical weather map analysis. J. Appl. Meteor., 3, 396-409.
- \_\_\_\_\_, 1973: Mesoscale objective analysis using weighted time-series observations. NOAA Tech. Memo. ERL-NSSL-62, 60 pp.
- Battan, L.J., 1973: Radar observations of the atmosphere. University of Chicago Press, Chicago, IL. 324 pp.
- Bohne, A., and R. Srivastava, 1975: Radar errors in wind and precipitation fall speed measurements by a triple-Doppler radar system. Laboratory for Atmospheric Probing, University of Chicago Tech. Memo. 37. 44 pp.
- Brandes, E.A., 1977a: Flow in severe thunderstorms observed by dual-Doppler radar. Mon. Wea. Rev., 105, 113-120.
- \_\_\_\_\_, 1977b: Mesocyclone evolution and tornado generation within the Harrah, Oklahoma Storm. NOAA Tech. Memo. ERL-NSSL-81, 28 pp.
- \_\_\_\_\_, 1978: Mesocyclone evolution and tornado-genesis: Some observations. Mon. Wea. Rev., 106, 995-1011.
- \_\_\_\_\_, 1983: Relationship between thunderstorm mesoscale circulation and tornadogenesis. Mon. Wea. Rev., 112, 1033-1052.
- Brown, J.M., K.R. Knupp, and F. Caracena, 1982: Destructive winds from shallow, high based cumulonimbi. Preprints, 12th Conf. on Severe Local Storms, San Antonio, Tx. Amer. Meteor. Soc., 272-275.
- Browning, K.A., and F.H. Ludlam, 1962: Airflow and structure of a tornadic storm. Quart. J. Roy.

Meteor. Soc., 117-135.

Byers, H.R., and R.R. Braham, 1948: Thunderstorm structure and circulation. J. Meteor., 5, 71-86.

Chong, M., F. Rous, and J. Testud, 1980: A new filtering and interpolating method for processing dual-Doppler radar data: Performance in three dimensional wind restriction, ability to derive pressure and temperature fields. Preprints 19th Conf. on Radar Meteor., Amer. Meteor. Soc., 286-293.

Cressman, G.P., 1959: An operational objective analysis system. Mon. Wea. Rev., 87, 367-374.

Davis-Jones, R.P. and J.H. Henderson, 1973: Characteristics of thunderstorm updraft soundings. Preprints, 8th Conf. on Severe Local Storms, Denver, CO. Amer. Meteor. Soc., 1-5.

Deardorff, J.W., 1975: The development of boundary layer turbulence models for use in studying the severe storm environment. Proc. SESAME open meeting, D.K. Lilly, ED., Boulder, NOAA Env. Res. Lab., 251-264.

Douglas, R.H., 1964: Hail size distributions. Proc., 1964 World Conference on Radio Meteorology and 11th Weather Radar Conf., Amer. Meteor. Soc., 146-149.

Doviak, R.J., P.S. Ray, R.G. Strauch, and L.J. Miller, 1976: Error estimates in wind fields derived from dual-Doppler radar measurements. J. Applied Meteor., 15, 868-878.

Elmore, K.L., 1982: Cell structure and evolution within a squall line as revealed by dual-Doppler radar. M.S. Thesis, Univ. of Oklahoma, 212 pp.

Foote, G.B., and P.S. duToit, 1969: Terminal velocity of raindrops aloft. J. Appl. Meteor., 8, 249-253.

Fujita, T.T., and H.R. Byers, 1977: Spearhead echo and downburst in the crash of an airliner. Mon. Wea. Rev., 105, 129-146.

\_\_\_\_\_, and F. Caracena, 1977: An analysis of three weather-related aircraft accidents. Bull. Amer. Meteor. Soc., 58, 1164-1181.

\_\_\_\_\_, 1978: Manual of downburst identifica-

tion for project NIMROD. SMRP Res. Paper 156,  
Univ. of Chicago. 104 pp.

\_\_\_\_\_, and R.M. Wakimoto, 1981: Five scales  
of airflow associated with a series of downbursts  
on 16 July 1980. Mon. Wea. Rev., 109, 1438-1456

\_\_\_\_\_, and \_\_\_\_\_, 1983: Microbursts  
in JAWS depicted by Doppler radars, PAM and aerial  
photography. Preprints, 21st Conf. on Radar  
Meteorology, Edmonton, Alta., Canada, Amer. Meteor.  
Soc., 638-645.

\_\_\_\_\_, 1985: The downburst microburst and  
macroburst. University of Chicago press, Chicago,  
IL., 122 pp.

Gal-Chen, T., 1978: A method for initialization for  
the anelastic equations: Implications for matching  
models. Mon. Wea. Rev., 537-606.

\_\_\_\_\_, 1979: A method for calculating tem-  
perature, pressure and vertical velocities from  
Doppler radar observations. Preprints, 11th Conf.  
on Severe Local Storms, Amer. Meteor. Soc., 492-  
496.

\_\_\_\_\_, and C.E. Hane, 1981: Retrieving  
buoyancy and pressure fluctuations from Doppler  
radar observations: A status report. Atmospheric  
Technology, NCAR, No. 13, 98-104.

\_\_\_\_\_, 1982: Errors in fixed and moving frame  
of references: Applications for conventional and  
Doppler radar analysis. J. Atmos. Sci., 39, 2279-  
2300.

\_\_\_\_\_, 1983: Matching three-dimensional con-  
vection models with Doppler radar observations.  
Mesoscale meteorology-theories, observations and  
models (Lilly and Gal-Chen, Eds.), D. Reidel  
Publication Co., 591-601.

\_\_\_\_\_, and R.A. Kropfli, 1984: Buoyancy and  
pressure perturbations derived from dual-Doppler  
radar observations of the planetary boundary layer:  
Applications for matching models with observations.  
J. Atmos. Sci., 41, 3007-3020.

Hane, C.E. and B.C. Scott, 1978: Temperature and  
pressure perturbations within convective clouds  
derived from detailed air motion information:

- Preliminary testing. Mon. Wea. Rev., 106, 654-661.
- \_\_\_\_\_, R.E. Wilhelmson, and T. Gal-Chen, 1981: Retrieval of thermodynamic variables within deep convective clouds: Experiments in three dimensions. Mon. Wea. Rev., 109, 564-576.
- \_\_\_\_\_, and P.S. Ray, 1983: Calculation of the pressure field in a tornadic thunderstorm. Preprints, 13th Conf. on Severe Local Storms, Tulsa, OK. Amer Meteor. Soc., 113-116.
- Kessinger, C., M. Hjelmfield, and J. Wilson, 1983: Low-level microburst wind structure using Doppler radar and PAM data. Preprints, 21st Conf. on Radar Meteor., Edmonton, Alta, Canada, Amer. Meteor. Soc., 602-608.
- Klemp, J.B., and R.B. Wilhelmson, 1978: The simulation of three-dimensional convective storm dynamics. J. Atmos. Sci., 35, 1070-1096.
- Koch, S.E., M. DesJardins, and P.J. Kocin, 1983: An interactive Barnes objective map analysis scheme for use with satellite and conventional data. J. Climate and Appl. Meteor. 22, 1487-1503.
- Kropfli, R.A. and L.J. Miller, 1976: Kinematic structure and flux quantities in a convective storm from dual-Doppler radar observations. J. Atmos. Sci., 33, 520-529.
- Lhermitte, R.M., 1968: New developments in Doppler radar method. Preprints, 13th Radar Meteor. Conf., Boston, MA. Amer. Meteor. Soc., 14-17.
- \_\_\_\_\_, 1970: Dual-Doppler radar observations of a convective storm circulation. Preprints, 14th Radar Meteor. Conf., Tucson, AZ., Amer. Meteor. Soc., 139-144.
- Lin, Y.J., and R.W. Pasken, 1982a: A diagnostic study of the tornadic storm based on dual-Doppler wind measurements. Cloud Dynamics (Agee and Asia, Eds.), D. Reidel Publication Co., 315-328.
- \_\_\_\_\_, and \_\_\_\_\_, 1982b: Kinematic and dynamic characteristics of a tornadic storm determined from dual-Doppler winds. Papers in Meteorological Research, A Journal of Meteor. Soc. of ROC, 5, 50-68.

- \_\_\_\_\_, and T. Wang, 1930: A numerical study of thunderstorm environment interactions determined from perturbation pressure gradient forces, part II: Trajectory calculations. Papers in Meteor. Res., A Journal of the Meteor. Soc. of the ROC., 3, 17-30.
- \_\_\_\_\_, \_\_\_\_\_, and J.H. Lin, 1985: Dynamic and thermodynamic properties within a squall-line derived from dual-Doppler wind measurements. Preprints, 14th Conference on Severe Local Storms, Indianapolis, IN, Amer. Meteor. Soc., 89-91.
- \_\_\_\_\_, \_\_\_\_\_, and \_\_\_\_\_, 1986: Pressure and temperature perturbations within a squall-line thunderstorm derived from SESAME dual-Doppler data. J. Atmos. Sci., (in press).
- Ludlum, F.H., 1963: Severe local storms -- A review. Meteor. Monogr., 27, 1-30.
- Martner, B.E., 1975: Z-R and Z-W relations from drop size measurements in high-plains thunderstorms. Preprints, 9th Conf. on Severe Local Storms, Norman, OK. Amer. Meteor. Soc., 307-310.
- McCarthy, J., R. Roberts, and W. Schreiber, 1983: JAWS data collection, analysis highlights, and microburst statistics. Preprints, 21st Conf. on Radar Meteor., Edmonton, Alta., Canada, Amer. Meteor. Soc., 624-629.
- \_\_\_\_\_, J. Wilson, T.T. Fujita, 1982: The joint airport weather studies project. Bull. Amer. Meteor. Soc., 63, 15-22.
- Mueller, C.K. and P.H. Hildebrand, 1983: The structure of a microburst: as observed by ground-based and airborne Doppler radar. Preprints, 21st Conf. on Radar Meteor., Edmonton, Alta., Canada, Amer. Meteor. Soc., 602-608.
- NCAR, and U of Chicago, 1983: The Jaws Project Operations Summary 1982, 276 pp.
- Nelson, S.P., 1980: A study of hail production in supercell storm using a Doppler derived wind field and a numerical hail growth model. NOAA Tech. Memo., ERL-NSSL-89, 90 pp.
- Nelson, S.P., and R.A. Brown, 1982: Multiple Doppler

radar derived vertical velocities in thunderstorms.  
Part I - Error analysis and solution techniques.  
NOAA Tech. Memo., ERL-NSSL-94, 21 pp.

Newton, C.W., 1963: Dynamics of severe convective storms. Severe Local Storms. Meteor. Monogr., 27, 33-58, Amer. Meteor. Soc.

Ogura, Y. and N.A. Phillips, 1962: Scale analysis of deep and shallow convection in the atmosphere. J Atmos. Sci., 19, 173-179.

Parsons, D.B., C.J. Kessinger, K.L. Elmore, and R.D. Roberts, An investigation into the forcing of microbursts. Preprints, 14th Conf. on Severe Local Storms, Indianapolis, IN., Amer. Meteor. Soc., 48-51.

Pasken, R.W. and Y.J. Lin, 1982: Pressure perturbation within a tornadic storm derived from dual-Doppler wind data. Preprints, 12th Conf. in Severe Local Storms, Amer. Meteor. Soc., 257-260.

Pille', R.J., J.E. Justio and R.R. Rogers, 1963: Wind velocity measurements with Doppler radar.. Preprint 10th Weather Radar Conf., Boston, MA. Amer. Meteor. Soc., 329-331.

Ray, P.S., R.J. Doviak, G.B. Walker, D. Sirmans, J. Carter and B. Bumgarner, 1975: Dual-Doppler observations of a tornadic storm. J. Appl. Meteor., 14, 1521-1530.

Ray, P.S., K.K. Wagner, K.W. Johnson, J.J. Stephens, W.C. Bumgarner, and E.A. Mueller, 1978: Triple-Doppler observations of a convective storm. J. Appl. Meteor., 17, 1201-1212.

Rodi, A.R., K. L. Elmore, and W.P. Mahoney, 1983: Aircraft and Doppler air motion comparisons in a JAWS microburst. Preprints, 21st Conf. on Radar Meteor., Edmonton, Alta., Canada, Amer. Meteor. Soc., 624-629.

Rogers, R.R., 1964: An extension of the Z-R relationship for Doppler radar. Preprints, 11th radar Meteor. Conf., Boston, MA. Amer. Meteor. Soc., 158-160.

Rotunno, R., and J.B. Klemp, 1982: The influence of shear induced pressure gradient on thunderstorm motion. Mon. Wea. Rev., 110, 136-151.

- Sasaki, Y., 1970: Some basic formalisms in numerical variational analysis. Mon. Wea. Rev., 98, 875-883.
- Sekhon, R.S., and R.C. Srivastava, 1971: Doppler radar observations of drop-size distributions in a thunderstorm. J. Atmos. Sci., 28, 983-994.
- Sinclair, P.C., 1978: Severe storm air velocity and temperature structure deduced from penetrating aircraft. Preprints, 8th Conf. on Severe Local Storms. Denver, CO. Amer.
- Smagorinsky, J., 1963: General circulation experiment with the primitive equations. 1. The basic experiment. Mon. Wea. Rev., 91, 99-164.
- Srivastava, R.C., 1985: A simple model of evaporatively driven downdraft: application to microburst downdraft. J. Atmos. Sci., 28, 1004-1023.
- Waldleufel, P., 1976: An analysis of weather spectra variance in a tornadic storm. NOAA Tech. Memo. ERL-NSSL-76, 80 pp.
- Wilson, J.R., R.D. Roberts, C. Kessinger, and J. McCarthy, 1983: Microburst wind structure and evaluation of Doppler radar for aircraft wind shear detection. Report for the FAA under contract #DTFA01-82-Y-10513, 44 pp.
- Wilson, J.R., R.D. Roberts, C. Kessinger, and J. McCarthy, 1984: Microburst wind structure and evaluation of Doppler radar for airport wind shear detection. J. Climate Appl. Meteor., 22, 1227-1241.
- Wirsing, F.C., 1985: An intercomparison of variational techniques in deriving three-dimensional wind and pressure fields from dual-Doppler radar data of a severe right-moving thunderstorm. M.S. Thesis, St. Louis Univ., 96 pp.
- Ziegler, C.L., 1978: A dual-Doppler variational objective analysis as applied to studies of convective storms. NOAA Tech. Memo. ERL-NSSL-85, Norman, National Severe Storms Lab., 116 pp.
- \_\_\_\_\_, P.S. Ray, and N.C. Knight, 1983: Hail growth in an Oklahoma multicell storm. J. Appl. Sci., 40, 1768-1791.

## Biography of the Author

Robert Gordon Hughes was born on June 4, 1946 in Richmond, Virginia. He attended public schools on the island of Okinawa, Japan from 1952-1964. In September 1964 he entered the Engineering Department, University of Hawaii, in Honolulu, Hawaii. In 1968, prior to his graduation, he entered the United States Army. He served three years, from 1968-1971, as a Nuclear Weapons Maintenance Technician in the Republic of Korea and on Guam, Mariannas Islands, Trust Territories of the United States. In 1971 he returned to the University of Hawaii and received his Bachelors degree in Mathematics in 1972. After graduation he joined the United States Air Force as a Second Lieutenant and received his initial training in meteorology at North Carolina State University. In 1974, he was assigned as a weather forecaster at Myrtle Beach Air Force Base, South Carolina. In 1975 he became the Chief Forecaster at that station. In 1978 he was selected to enter the Air Force Institute of Technology and in 1980 received a Master of Science degree in meteorology from Purdue University. In 1980 he was assigned to the Environmental Technical Applications Center at Scott AFB, IL. From 1980 to 1983 he held the posts of Chief, Electromagnetic Propagation



Section, Chief, Basic Assessment Section and Chief, Data Base Management Section. In 1983, he was again selected to enter the Air Force Institute of Technology at St. Louis University. He joined the Department of Meteorology in August 1983 and has pursued his PH.D. in the field of meteorology since then. During the past three years he has been working on the Severe Storms Research Project, supported by the United States Air Force Institute of Technology and the National Science Foundation, under the direction of Dr. Yeong-jer Lin

END

DTIC

9-86